

MAGNETIC FIELDS, COSMIC RAYS AND
SYNCHROTRON EMISSION IN SPIRAL GALAXIES

ANDREW SNODIN

A thesis submitted for the degree of
Doctor of Philosophy



*School of Mathematics and Statistics
Newcastle University
Newcastle upon Tyne
United Kingdom*

February 2008

Abstract

Magnetic fields have been detected in many spiral galaxies. Observations of polarized radio synchrotron emission are the most useful tool in exploring the nature of these fields. We have developed methods to generate synthetic polarization maps of spiral galaxies (with allowance for their position and inclination with respect to the line of sight) from magnetic field models and other data. Polarization maps based on dynamo and gas dynamical models for barred galaxies are compared with maps observed at $\lambda\lambda 3.5$ and 6.2 cm. We have developed methods and procedures to make the comparisons of theory and observations both direct and meaningful, resulting in the most detailed comparisons to date. It is shown that gas dynamical and dynamo models for the galaxy NGC 1365 are broadly compatible with radio observations, but we have identified deficiencies which are most likely attributable to earlier published gas dynamical models. We also find that the variation of cosmic ray energy density across the galaxy is much weaker than that of the magnetic field, so that energy equipartition between the two can not be maintained locally. To justify and understand this, we have developed a numerical two-fluid MHD model for the evolution of cosmic ray energy density in magnetic field produced by interstellar turbulence. This is the first such model for cosmic ray dynamics where the magnetic field is produced by dynamo action. We have demonstrated that the large diffusivity of cosmic rays can be successfully modelled with a non-Fickian approach. Cosmic ray energy density in our model is seen to exhibit some correlation with gas density, but not with the magnetic field.

Contents

1	Introduction	1
1.1	Galaxies	2
1.2	Magnetic fields in spiral galaxies	6
1.3	Cosmic rays	7
1.4	Synchrotron emission	8
2	An overview of galactic magnetic fields and cosmic rays	10
2.1	Basic ideas and equations	11
2.1.1	Maxwell's equations	11
2.1.2	The induction equation	11
2.1.3	Electromagnetic waves	12
2.2	The Stokes Parameters	12
2.3	Synchrotron emission	14
2.3.1	Polarization	15
2.3.2	Emissivity	16
2.3.3	Propagation	17
2.4	Observed magnetic field strengths	18
2.5	Galactic dynamos	19
2.5.1	Small scale dynamos	19
2.5.2	Mean-field models	20
2.6	Cosmic rays	22
3	Propagation of cosmic rays in turbulent magnetic fields	26
3.1	Introduction	27
3.2	Method	27
3.2.1	Cosmic ray hydromagnetic equations	27
3.2.2	Non-Fickian diffusion	29
3.2.3	Numerics	32

3.2.4	A remedy for cosmic ray diffusion near a magnetic X-point . . .	33
3.3	Macroscopic evolution of the cosmic ray gas	33
3.3.1	Energy balance	33
3.3.2	Compressional enhancement of cosmic ray energy	36
3.3.3	Effect of cosmic ray pressure	38
3.3.4	Cosmic rays in a partially ordered magnetic field	38
3.4	Propagation in dynamo generated magnetic fields	41
3.5	Discussion	49
4	Synthetic radio maps	51
4.1	Overview	52
4.2	Stokes parameters for model galaxies	53
4.3	Models for cosmic ray distribution	55
4.4	Generating synthetic radio maps	56
4.4.1	Outline	56
4.4.2	Dealing with different types of model	57
4.4.3	Rotation to the sky frame	58
4.4.4	Lines of sight	62
4.4.5	Integration along the lines of sight	63
4.4.6	Implementation of beam smoothing	64
4.5	Example	64
5	Detailed modelling of the magnetic fields in the barred galaxies NGC 1097 and NGC 1365	71
5.1	Radio observations	72
5.2	NGC 1097 and 1365	74
5.3	Global models of NGC 1365	77
5.3.1	The gas dynamical models	78
5.3.2	The dynamo models	80
5.3.3	Results	85
5.3.4	Synthetic polarization maps	88
5.3.5	Cuts through polarization maps	95
5.3.6	The difference maps	97
5.3.7	Faraday rotation	99
5.3.8	Magnetic field structure	99
5.3.9	Sensitivity to parameters, and implications of the dynamo models	101
5.3.10	Dependence on the gas ionization fraction	107

5.4 Discussion and conclusions	107
6 Basic conclusions	110
A Boundedness of cosmic ray energy density	113
B The forcing function	114
Bibliography	115

Chapter 1

Introduction

This thesis explores two main nonthermal ingredients of the interstellar medium, magnetic fields and cosmic rays, and their manifestations via the synchrotron emission. In the following, I shall briefly introduce the subjects of this thesis and attempt to motivate the key ideas to be discussed in the subsequent chapter.

1.1 Galaxies

A *galaxy* is a collection of stars, gas, dust, and non-visible matter (or dark matter) held together by gravity. Our knowledge of galaxies derives from a combination of observations of our own galaxy (known as *the Galaxy*), external galaxies and theoretical ideas. Together they provide information about the composition, distance to and sizes of galaxies, and estimates of associated masses and velocities. The shapes, sizes and masses of galaxies are seen to vary widely. The smallest known galaxies contain about $10^5 - 10^6$ stars and the largest may have more than $10^{12} - 10^{13}$ stars. The range of sizes is about 1 – 100 kpc in diameter.

The majority of galaxies have some quite distinctive shape falling into one of several classes. 95% of the observable galaxies can be classed as either *spiral* or *elliptical* galaxies. Elliptical galaxies have a blob-like ellipsoidal shape, whereas spiral galaxies are usually extremely *flat* and exhibit striking spiral structure (see Fig. 1.1) In the 1930's Edwin Hubble introduced a classification system of these galactic types. Spirals were given two subclasses; ordinary and *barred* spirals. Together they are graphically represented in the tuning fork diagram or Hubble sequence as show in Fig. 1.2. The *lenticular* galaxies (S0 in the diagram) are at the branch point of the fork with ellipticals to the left and spirals to the right (lenticulars are rather flat like spiral galaxies, but show no spiral structure). The spirals are classified in terms of the nature of the spiral structure and the ellipticals in terms of how flattened they appear. Hubble had thought that the variations in morphology of the observed galaxies might be due to some kind of evolutionary process and this is reflected in the diagram layout. Today, along with *irregular galaxies* (which have no particular morphological features), this general classification is in common use; other rarer classes of galaxies are sometimes introduced.

The differences between types of galaxies are now usually attributed to the way in which they were formed and their early evolution. Most galaxies were probably formed when the cosmological matter in the denser regions began to collapse and cluster together. It appears that all the observable galaxies have similar ages, of the order 10^{10} years.



Figure 1.1: Optical images of two spiral galaxies obtained with the NASA/ESA Hubble Space Telescope. Top: The Whirlpool spiral galaxy M51. Below: The barred spiral galaxy NGC 1300.

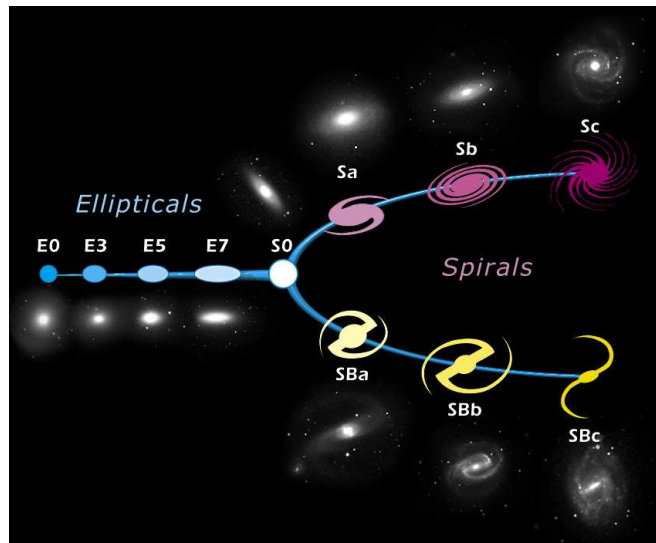


Figure 1.2: A Hubble sequence diagram. The ellipticals are to the left; upper right are the ordinary spirals and lower right are barred spirals (SB). From hubblesite.org.

Spirals account for about 70% of the observable galaxies. A spiral galaxy typically consists of a blob-like central nucleus or bulge surrounded by a flat, rapidly-rotating disc. They usually have a spherical halo of sparsely distributed stars and other matter which has low luminosity. Spirals are characterized by spiral structures in their light distribution, which are regions of star formation containing the most massive hot young (of age $< 10^7$ years) stars that give off blue light. Fig. 1.1 shows two optical images of spiral galaxies in which this structure can be seen. The oldest stars (around 10^{10} years) in a spiral galaxy reside in the bulge and halo. These stars take strongly elliptical orbits around the galactic centre. There is little gas in the bulge and halo; most of the gas in a galaxy is in the disc. Most of the stars of the disc are of intermediate and younger age and their orbits are much more circular than those in the bulge and halo. Usually a significant fraction of the mass is contained in the central blob. A barred spiral galaxy has an elongated (and often flattened) central nucleus, rather than a spherical one of a normal spiral. The lower image of Fig 1.1 is the barred spiral galaxy NGC 1300 which has a distinctive bar. The distinction between ordinary and barred spiral galaxies may not always be clear because the bar might be like an elongated blob, rather than a flattened ellipse. Our own Galaxy is a spiral galaxy and like the majority of spirals it seems to have a bar (see e.g. Gerhard 2002; Benjamin et al. 2005).

The interstellar medium (or ISM) is the medium between the stars in a galaxy, where typically 10% of the galaxy's visible mass is found. It consists of mainly gas,

dust, magnetic fields and high energy particles. Exploding supernova stars and stellar winds disturb the surrounding gas and drive turbulent motions in the medium, up to scales of 100 pc in the Galaxy. The supernova remnants can also heat the gas to high temperatures. These processes are just part of the complex ISM dynamics, leading to a rather inhomogeneous structure. The magnetic fields and high energy particles are also thought to play a significant rôle in determining this structure, if for no other reason that their energy densities in the ISM are observed to be comparable to both the thermal energy and the kinetic energy of the turbulent motions. In the Galaxy there are several distinct observable gas components. Roughly half the matter of the ISM is clumped into discrete cold ($T \sim 10 - 100$ K) clouds of molecular and atomic gas. The rest of the matter is warmer and more uniformly spread out. Most of this is warm atomic matter ($T \sim 8000$ K), which has a similar total mass in the Galaxy to the cold gas, but a density about 100 times smaller near the position of the sun. Warm ionized matter, of a similar temperature to the warm atomic matter but constituting slightly less total mass, is found quite uniformly throughout the ISM apart from in regions surrounding massive hot stars (known as “H II regions”), where it has a much higher density. The hot ionized component ($T \sim 10^6 - 10^7$ K) originates in supernova remnants and constitutes a not well known fraction of the total mass, but probably quite a bit smaller than the other components mentioned above. The average mass density in the ISM is equivalent to about 1 hydrogen atom per cm^3 . (See e.g. Lequeux 2005, for more details of these components and the ISM.)

Measurements of Doppler shifts of various spectral lines in the electromagnetic emission from stars and gas allows the velocities along an observer’s line of sight to be deduced. For external galaxies, if the angle of inclination between the plane of a galactic disc and the observer’s line of sight is known, corresponding velocities in the disc can be calculated. If we assume the velocities are in the azimuthal direction in the plane of the galaxy, we can obtain the radial profile of galactic rotation (in some cases both the azimuthal and radial velocities can be deduced; e.g. for the galaxy M31 (Braun 1991)). The plot of rotation speed against radial distance from the galactic centre is known as a *rotation curve*. These are known for many galaxies. In Fig. 1.3, rotation curves obtained by Sofue et al. (1999) are shown for the two barred spiral galaxies discussed in Chapter 5. These have been obtained from a combination of H I (neutral hydrogen) and CO observations. We see that outside the central regions the two curves are relatively flat. This flat part of the curve is typical of spiral galaxies i.e. they are seen to rotate *differentially* with the highest angular velocities near the centre. This implies that the mass in galaxies is not concentrated in the most luminous

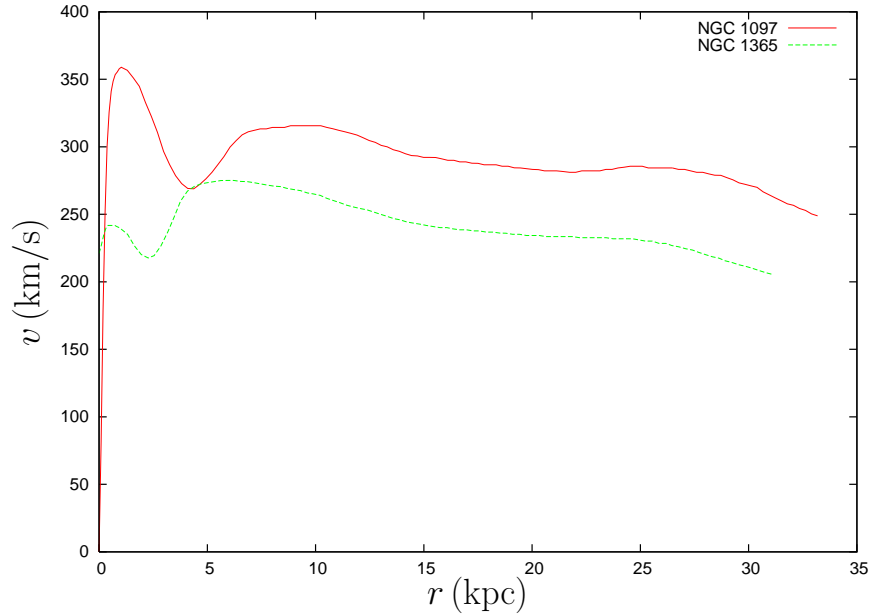


Figure 1.3: Rotation curves of Sofue et al. (1999) for two spiral galaxies: NGC 1097 and NGC 1365

regions, but is distributed across the galactic disc. The review of van der Kruit & Allen (1978) provides a useful discussion on the measurements of the velocities and rotation curves for spiral galaxies.

Where galaxies are mentioned in the remainder of this text, we shall be referring primarily to spiral galaxies, regardless of the applicability in a particular context to other types of galaxies.

1.2 Magnetic fields in spiral galaxies

A connection between the observed polarization of starlight in our Galaxy (Hiltner 1949; Hall 1949) and preferred orientations of dust grains in a magnetic field was made by Davis & Greenstein (1951); this was the first discovery of magnetic fields in our Galaxy. A large collection of nearby observations of polarized starlight in our Galaxy by Mathewson & Ford (1970) suggests that the magnetic field in the Galaxy is almost azimuthal at the position of the Sun. For a few nearby external galaxies, observations of polarized starlight can be made and these have revealed large scale magnetic spiral structure (e.g. in M51 by Scarrott et al. 1987), similar to those seen in the optical images.

Today radio frequency observations of *synchrotron* emission provide insight into the

basic properties of the interstellar medium of spiral galaxies, in particular the magnetic fields. Measurements of magnetic fields are obtained primarily from the intensity and Faraday rotation of the emission, which we shall address shortly. With synchrotron emission measurements, many spiral galaxies have been observed to have large-scale regular magnetic fields. As with the nearby polarized starlight observations, these fields often have spiral structure which has a similar pitch and structure to the pattern seen in the light distribution. The magnetic field structure does not necessarily occur in the same location as the optical structure. Smaller scale tangled fields are also observed in spiral galaxies. The regular large scale fields are, in several cases, strongest in between the optical spiral arms. However, the total field strength (i.e. the sum of the regular and the random small scale fields) is found to be strongest near the optical arms. The spiral patterns in the regular magnetic field are generally thought to be produced from the differential rotation of the disc via dynamo action. Also, because of turbulent motions in the ISM and the apparently large random field strengths, it is likely that some sort of dynamo action occurs on smaller scales. The disc of a spiral galaxy has a magnetic field with a strength much less than that of the Earth measured at its surface.

In our own Galaxy, observations near our location indicate that the magnetic field has a tendency to be aligned with the disc plane. This is consistent with observations of magnetic field alignment in external edge-on galaxies. Estimates of the regular field strength near the sun are typically around $4 \mu\text{G}$, and for the random field around $5 \mu\text{G}$. The total field strength is similar to that found in external spiral galaxies (see Sect. 2.4).

The origin of magnetic fields in galaxies is unknown, but several plausible mechanisms have been proposed; we shall not address these issues in this thesis.

1.3 Cosmic rays

Cosmic rays are high energy charged particles having velocities close to the speed of light. They were discovered by Hess in 1912 via balloon experiments in the earth's atmosphere. Hess had thought he had discovered 'rays' and for some time after it was thought that cosmic rays were gamma rays, hence the name which is used today. The cosmic rays detected near the earth and in the upper atmosphere consist of most ionized nuclei, but are mainly protons. Electrons account for about 1% of the observed cosmic ray energy.

Observations of composition suggest that their sources could be rapidly evolving young stars which release the particles into the ISM via supernova explosions. The resulting shock waves potentially provide acceleration mechanisms to obtain cosmic

rays with energies up to 10^{15} eV; estimates suggest that more than 10% of the kinetic energy in the blast waves can be converted into cosmic ray energy (see e.g. Hillas 2005, and references therein). The highest observed energies of cosmic rays are about 10^{21} eV, but these are quite rare. They are not well understood and may originate from outside the Galaxy.

From whatever their sources are, cosmic rays pass through the interstellar space, then eventually leave the galaxy. In this passage, the probability of a cosmic ray particle interacting with matter in the ISM is very low, so cosmic rays can be considered essentially collisionless. However, the interactions that do occur, both with other cosmic rays and interstellar material, are important in understanding the ISM. Fragmentation of cosmic ray particles through interaction with this matter (spallation) produces lighter nuclei, providing means of estimating where cosmic rays have come from and how long they have existed by comparing ratios of different nuclei. Apart from directly observing cosmic rays about the location of the earth, gamma rays and the synchrotron emission introduced in the next section provide (independently) indirect information about cosmic rays (and also magnetic fields). Observations suggest that the maximum time spent by a cosmic ray particle in the Galaxy is about $10^7 - 10^8$ years (see e.g. Simpson 1983, and references therein).

The bulk of the cosmic ray energy density is provided by protons. The pressure of cosmic rays is roughly the size of their energy density and exerts an isotropic force on the background plasma through its gradient. The dynamical importance of cosmic rays in the ISM has long been recognized (Ginzburg & Syrovatskii 1964; Parker 1966; Berezhinskii et al. 1990). Spatial gradients of the cosmic ray pressure contribute significantly to the force balance in the ISM.

1.4 Synchrotron emission

Perhaps the most useful tool in understanding the magnetic fields of spiral galaxies is observation of synchrotron emission. This is the linearly polarized emission from highly relativistic electrons gyrating in a magnetic field. Both the polarized and total intensity of synchrotron emission can be observed; the unpolarized intensity is the difference of the two. The orientation in the plane of the sky of the regular large scale magnetic fields is obtained from the observed polarization direction of the emission. The strength of this field is related to the intensity of the polarized emission, while the total field strength (the sum of the regular and random components) can be deduced from the total intensity. The measured Faraday rotation (see below) probes the direction of the overall

line of sight field component. In the Galaxy, the line of sight averaged field strengths can be obtained by combining the dispersion and Faraday rotation measure of pulsars (see e.g. Rybicki & Lightman 1979). Combining the line of sight components with the measured direction and total strength provides the regular magnetic field projected onto the plane of the sky. We shall see that to calculate meaningful estimates of the perpendicular component of the field strengths and to estimate the ratio of random to regular field strengths from the observed degree of polarization, additional assumptions or information is required. Usually this involves relating the magnetic field energy to the energy in cosmic rays. In addition, the fraction of energy contained in relativistic electrons must be estimated. Despite some consistency between other methods of estimating field strengths, the underlying physical basis for the connections between energies or pressure of cosmic rays and magnetic fields is not clear.

Chapter 2

An overview of galactic magnetic fields and cosmic rays

2.1 Basic ideas and equations

In studying the interstellar medium (ISM) of spiral galaxies at macroscopic scales a fluid description for the gas constituents can be adopted. This gas is mostly plasma (i.e. it is partially or fully ionized) and is permeated by magnetic fields. To model the magnetic fields of such a medium we need to consider the interaction of the gas flow with the magnetic fields. To do this we can combine Maxwell's equations describing the large scale electromagnetic fields with the Navier-Stokes equations describing fluid motion to obtain the equations of magnetohydrodynamics (MHD) for a conducting fluid.

In the following I state some basic ideas and relations for the above that are required in the rest of this chapter.

2.1.1 Maxwell's equations

The appropriate Maxwell's equations (see e.g. Jackson 1975, for more details) describing the large scale evolution of the electromagnetic fields in can be written (in cgs units)

$$\nabla \cdot \mathbf{E} = 4\pi\rho_e, \quad (2.1)$$

$$\nabla \cdot \mathbf{B} = 0, \quad (2.2)$$

$$\nabla \times \mathbf{E} = -\frac{1}{c} \frac{\partial \mathbf{B}}{\partial t}, \quad (2.3)$$

$$\nabla \times \mathbf{B} = \frac{1}{c} \frac{\partial \mathbf{E}}{\partial t} + \frac{4\pi}{c} \mathbf{J}, \quad (2.4)$$

where \mathbf{B} is the magnetic flux density (often referred to as the magnetic field), \mathbf{E} is the electric field, \mathbf{J} is the current density, c is the speed of light, and ρ_e is the charge density. Eq. (2.4) is the key equation relating the currents in the gas to the magnetic field.

2.1.2 The induction equation

The current \mathbf{J} is in general a function of the fields \mathbf{E} and \mathbf{B} . Using the equation for the electric field in a moving medium one obtains

$$\mathbf{J} = \sigma \left(\mathbf{E} + \frac{1}{c} \mathbf{U} \times \mathbf{B} \right), \quad (2.5)$$

where σ is the conductivity (or the inverse of resistivity). In MHD we neglect the displacement current, corresponding to the first term on the right hand side of Eq. (2.4), because for velocities much smaller than c (i.e. non-relativistic), that term will be negligible compared with the left hand side. Taking the curl of Eq. (2.4) and using Eq. (2.5) for \mathbf{J} we can obtain

$$\frac{\partial \mathbf{B}}{\partial t} = \nabla \times (\mathbf{U} \times \mathbf{B}) + \eta \nabla^2 \mathbf{B}. \quad (2.6)$$

where $\eta = c^2/\pi\sigma = \text{const}$ is the resistivity. This is known as the magnetic induction equation.

2.1.3 Electromagnetic waves

Maxwell's equations exhibit travelling wave solutions for the electromagnetic field. In a vacuum the term containing \mathbf{J} on the right hand side of Eq. (2.4) and the term on the right of Eq. (2.1) are both zero. Combining Eqs (2.3) and (2.4) we obtain

$$\nabla \times (\nabla \times \mathbf{E}) = -\frac{1}{c^2} \frac{\partial^2 \mathbf{E}}{\partial t^2} = 0.$$

Then we can use Eq. (2.1) and $\nabla \times (\nabla \times \mathbf{E}) = \nabla (\nabla \cdot \mathbf{E}) - \nabla^2 \mathbf{E}$ to get

$$\nabla^2 \mathbf{E} - \frac{1}{c^2} \frac{\partial^2 \mathbf{E}}{\partial t^2} = 0. \quad (2.7)$$

Using the other relations we obtain a similar equation for \mathbf{B} . The general solutions to both equations are superpositions of

$$\psi(\mathbf{k} \cdot \mathbf{r} - \omega t). \quad (2.8)$$

If we consider travelling wave solutions for both the \mathbf{B} and \mathbf{E} equations one can deduce that \mathbf{E} and \mathbf{B} are orthogonal to each other and the direction \mathbf{k} , of the wave propagation.

2.2 The Stokes Parameters

A flux of electromagnetic radiation can be completely described by a set of four parameters and its frequency. *The Stokes parameters* are one possible choice; mathematically they are convenient and they can also be calculated from directly observable quantities. Since the electric and magnetic vectors perpendicular to the wave propagation direction are perpendicular to each other and follow the same wave equation, we only need to consider Stokes parameters for one of these vectors; we here describe the parameters

for the \mathbf{E} vector. The full details of these parameters can be found, for example in Pacholczyk (1970); here we just briefly outline the relations useful in the subsequent sections.

The \mathbf{E} vector for a general electromagnetic wave at a *single frequency* can be expressed as two components in perpendicular directions with some phase difference. The components along the x and y axis of some plane perpendicular to the propagation direction can be written as

$$E_x(t) = A_1 \cos(\omega t - \phi_1), \quad E_y(t) = A_2 \cos(\omega t - \phi_2). \quad (2.9)$$

(Other than frequency, a particular wave of this type is characterized by three independent quantities; A_1 , A_2 and the difference in the phase, $\phi_2 - \phi_1$.) In this plane, it can be shown that the \mathbf{E} vector components above map out an ellipse. The major axis of this ellipse is oriented at some angle to the x axis which we shall denote ψ . If we define the angle χ by $\tan \chi = E_1/E_2$, with $E_{1,2}$ the components of \mathbf{E} along the major and minor axes of the ellipse, the above components can be written as

$$\begin{aligned} E_x(t) &= A(\cos \psi \cos \chi \cos \omega t - \sin \psi \sin \chi \sin \omega t), \\ E_y(t) &= A(\sin \psi \cos \chi \cos \omega t + \cos \psi \sin \chi \sin \omega t) \end{aligned} \quad (2.10)$$

Notice we can now use A , ψ and χ to define the wave. The Stokes parameters for this wave relate the quantities in Eqs (2.9) and (2.10) and are defined as

$$I \equiv A_1^2 + A_2^2 = A^2, \quad (2.11)$$

$$Q \equiv A_1^2 - A_2^2 = A^2 \cos 2\psi \cos 2\chi, \quad (2.12)$$

$$U \equiv 2A_1A_2 \cos(\phi_1 - \phi_2) = A^2 \sin 2\psi \cos 2\chi, \quad (2.13)$$

$$V \equiv 2A_1A_2 \sin(\phi_1 - \phi_2) = A^2 \sin 2\chi. \quad (2.14)$$

The parameter I is the total flux density (or intensity) of the radiation ($I \propto E^2 \propto B^2$) Here we have four Stokes parameter, but they are not independent as $I^2 = Q^2 + U^2 + V^2$. This is because the wave is completely polarized. The parameter V gives us the shape of the polarization ellipse and its sign determines the direction in which the \mathbf{E} vector maps out the circle. $V = 0$ corresponds to linear polarization. As mentioned above, the magnetic field in the source of the emission is perpendicular to the polarization direction in the plane perpendicular to the propagation direction.

Therefore the magnetic field locally is oriented at an angle

$$\psi_B = \frac{\pi}{2} + \psi = \frac{\pi}{2} + \frac{1}{2} \tan^{-1} \left(\frac{U}{Q} \right) \quad (2.15)$$

i.e. we can deduce the magnetic field *orientation* from the polarization states via Q and U . Generally this will be the mean field orientation when averaging over a source of synchrotron emitting electrons. Note that we cannot determine the direction of the field because this is only the projection of the field onto the observer's plane – we shall see later how we can do this.

In reality, an observed signal is not quite of the form (2.9), but is a superposition of such waves with a finite range of frequencies, which is equivalent to taking A_1 , A_2 and $\phi_2 - \phi_1$ as slowly varying functions of time. A so-called *quasi-monochromatic* wave is partially polarized and can be expressed in terms of the Stokes parameters, as in Eqs (2.11)–(2.14):

$$I = I_p + I_u, \quad (2.16)$$

$$Q = I_p \cos 2\psi \cos 2\chi, \quad (2.17)$$

$$U = I_p \sin 2\psi \cos 2\chi, \quad (2.18)$$

$$V = I_p \sin 2\chi, \quad (2.19)$$

where I_p and I_u are the intensities of the polarized and unpolarized parts of the wave, respectively. These parameters are essentially time averaged superpositions of the monochromatic Stokes parameters (i.e. $I_p + I_u = \langle A_1^2 \rangle + \langle A_2^2 \rangle$). We see here that $I = \sqrt{Q^2 + U^2 + V^2} + I_u$, i.e. unlike in the case of a monochromatic plane wave, the four parameters are independent. Suppose the above Stokes parameters correspond to the radiation at some emitting region. To obtain expressions for the observed Stokes parameters, we then need to solve the transfer equation for the subsequent propagation, which will be trivial only in a vacuum. We shall make use of the above expressions in the next section.

2.3 Synchrotron emission

Synchrotron emission (or magnetobremstrahlung) is the radiation emitted by highly relativistic electrons gyrating in a magnetic field. The radio emission spectrum in the galaxy (and in many other sources) is observed to follow approximately a power law in a wide range of frequencies. In addition it is polarized. These two features are

not characteristic of thermal emission, but are explained by the theory of synchrotron emission; the observed radio emission with this non-thermal character is therefore regarded as synchrotron emission. Synchrotron emission has been found in the optical and X-ray regions of the electromagnetic spectrum in addition to the radio regions that are of interest here. In the following, I shall briefly outline details of the theory necessary for interpreting radio observations and for making synthetic radio maps for model galaxies. For our purposes here, a detailed theory of all the properties of synchrotron emission is not required (see e.g. Pacholczyk 1970; Rybicki & Lightman 1979; Ginzburg & Syrovatskii 1965).

The radiation from a non-relativistic electron gyrating in a magnetic field can generally be observed at any angle relative to its velocity vector. However, a highly relativistic electron in the same field will in contrast radiate electromagnetic waves only within a narrow angle about its velocity vector. This radiation is usually elliptically polarized, with the minor axis of the polarization ellipse parallel to the projection of the magnetic field vector onto the plane perpendicular to the wave propagation direction, within the synchrotron emitting region.

2.3.1 Polarization

The general elliptic polarization of the emission from a single relativistic electron is characterized by the Stokes parameters of Eqs (2.16)–(2.19). An ensemble of electrons in an emission region with a uniform magnetic field will have a distribution of pitch angles and therefore different elliptical polarizations relative to an observer's line of sight. On average, the total emission will be linearly polarized. In terms of the Stokes parameters, V , a measure of the axis ratio of the of the polarization ellipse, vanishes, since the angle χ in expressions (2.16) and (2.19) is zero. The remaining Stokes parameters can be defined with respect to some coordinate system of an observer as

$$I = I_p + I_u, \quad (2.20)$$

$$Q = I_p \cos 2\psi, \quad (2.21)$$

$$U = I_p \sin 2\psi = Q \tan 2\psi, \quad (2.22)$$

where now we only have the angle ψ which is the angle between the polarization plane (or the \mathbf{E} vector) and the x -axis of the coordinate system. Unlike the emission from individual electrons, we now have fractional polarization which can be expressed as the

ratio $p_0 = I_p/I$, or in terms of the other Stokes parameters

$$p_0 = \frac{I_p}{I} = \frac{\sqrt{Q^2 + U^2}}{I}. \quad (2.23)$$

2.3.2 Emissivity

Before considering the propagation of the emission we shall state how I_p and I_u are related to the properties of the emission region. We need to consider an ensemble of electrons for some finite region and calculate the total synchrotron emissivity per unit volume, ϵ , where $I = \int_V \epsilon dV$. Here we shall simply state important known results. If we consider an isotropic power law spectrum of relativistic electron energies

$$N(E) dE = N_0 E^{-\gamma} dE \quad (2.24)$$

(where $N(E) dE$ is the number of electrons with energies between E and $E + dE$ per unit volume), the total emissivity, for a region with uniform field, at a given (sufficiently short) wavelength is related to the field strength, wavelength and number density of relativistic electrons by

$$\epsilon \propto N_0 B_{\perp}^{(\gamma+1)/2} \lambda^{(\gamma-1)/2}. \quad (2.25)$$

If we denote the synchrotron spectral index of the emission α_s (i.e. $I(\lambda) \sim \lambda^{\alpha_s}$) then we see that

$$\alpha_s = (\gamma - 1)/2. \quad (2.26)$$

It can be shown that the degree of polarization for this uniform field region is

$$p_0 = \frac{\gamma + 1}{\gamma + 7/3}, \quad (2.27)$$

which is independent of λ . With $\gamma = 3$, close to locally observed values, the degree of polarization would be 0.75.

One final important point is that an emitting region of isotropic random field has *no* polarization. We shall now write some Stokes parameters, incorporating the above results, which we can use to study the polarization of synchrotron emission from galaxies. The above results can be found, for example, in Pacholczyk (1970) and Ginzburg & Syrovatskii (1965).

2.3.3 Propagation

In spiral galaxies we can neglect most of the interactions of the propagating synchrotron emission with the plasma of the ISM. Absorption of the emission by relativistic electrons should be relatively small at wavelengths of interest, compared with emission and the observed degree of polarization as a function of wavelength is consistent with this. However, we need to consider an effect that can be imparted by thermal electrons gyrating in magnetic fields in regions through which the emission passes. Faraday rotation causes the polarization angle of an electromagnetic wave to change when passing through such a region. This is because two circularly polarized waves with the opposite sense of rotation will pass through the region at different speeds, so that the phase difference between the waves will change. An elliptically (or linearly) polarized wave can be considered to be a superposition of two such waves and therefore in passing through a region of thermal electrons its polarization angle will change. This depends on the sign and strength of the magnetic field in the direction parallel to the wave propagation. If we consider a wave of a given wavelength λ , propagating in the z -direction from $z = 0$, the polarization plane will rotate through an angle

$$F = \frac{\lambda^2 e^3}{2\pi m_e^2 c^4} \int_0^L n_e(z) B_{\parallel}(z) dz \quad (2.28)$$

$$\simeq 0.81 \text{ rad} \left(\frac{\lambda}{1\text{m}} \right)^2 \int_0^L \left(\frac{n_e(z)}{1\text{cm}^{-3}} \right) \left(\frac{B_{\parallel}(z)}{1\mu\text{G}} \right) \frac{dz}{1\text{pc}} \quad (2.29)$$

when it passes through a region of length L . Here $n_e(z)$ is the thermal electron density and $B_{\parallel}(z)$ is the magnetic field component along the propagation direction.

The Stokes parameters (for an observer at $z = \infty$ along the line of sight in the z -direction), corresponding to the emission from multiple emitting regions with homogeneous magnetic field along lines of sight and taking into account the Faraday rotation can be written as

$$I(\lambda) = \int_{-\infty}^{\infty} \epsilon(z, \lambda) dz, \quad (2.30)$$

$$Q(\lambda) = \int_{-\infty}^{\infty} p_0(z) \epsilon(z, \lambda) \cos[2\psi(z)] dz, \quad (2.31)$$

$$U(\lambda) = \int_{-\infty}^{\infty} p_0(z) \epsilon(z, \lambda) \sin[2\psi(z)] dz. \quad (2.32)$$

Here p_0 and ϵ now vary with position along the line of sight and

$$\psi(z) = \psi_0(z) + 0.81 \text{ rad} \left(\frac{\lambda}{1\text{m}} \right)^2 \int_z^{\infty} \left(\frac{n_e(z')}{1\text{cm}^{-3}} \right) \left(\frac{B_{\parallel}(z')}{1\mu\text{G}} \right) \frac{dz'}{1\text{pc}}, \quad (2.33)$$

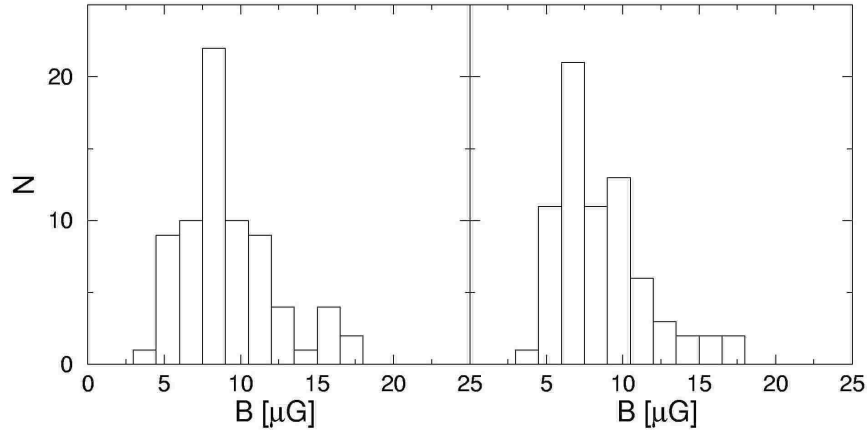


Figure 2.1: Total magnetic field strengths in some spiral galaxies from Niklas (1995). The left and right plot use the same data, but slightly different assumptions to deduce magnetic field strengths.

where the second term on the right accounts for the Faraday rotation from the local position to the observer and

$$\psi_0(z) = \frac{\pi}{2} + \tan^{-1} \left(\frac{B_y(z)}{B_x(z)} \right) \quad (2.34)$$

is the intrinsic polarization angle (cf. Eq. (2.15)). From the observed Q and U at a given wavelength we can obtain a polarization angle, $\Psi = (1/2) \arctan U/Q$. This provides the magnetic field direction perpendicular to the line of sight, averaged along the line of sight, but this is rotated through some angle due to Faraday rotation. For small λ , this rotation will be negligible.

2.4 Observed magnetic field strengths

Assuming we can deduce the spectral index γ of the synchrotron emission (e.g. via (2.26)), then the emissivity at a given wavelength (2.25) depends on both the magnetic field and the number density of cosmic ray electrons. This presents a problem in deducing magnetic field strength estimates from the observed emission. There are a few assumptions that can be made to relate the magnetic field strength to the cosmic ray electrons, the details of which can be found in e.g. Longair (1994, page 292). One is that of minimum total energy in the synchrotron source. Two others relate the energy density of, or pressure due to cosmic rays to the energy density of the magnetic field. To use either of these assumptions, another assumption relating the total energy of the

cosmic rays to the energy in cosmic ray electrons. Recent formula to obtain magnetic field estimates with these methods are outlined in Beck & Krause (2005). The problem with these assumptions is that in general there is no physical basis for them (see e.g. (Longair 1994, page 294), for further discussion). We shall see later that using such assumptions is unfavourable in our modelling.

Distributions of the total magnetic field strength, from a sample of spiral galaxies, obtained from observed I using energy equipartition assumptions are shown in Fig. 2.1 of Niklas (1995). In the Galaxy, estimates of the regular field strength near the sun are typically around $4 \mu\text{G}$ and the random field strength is around $5 \mu\text{G}$.

2.5 Galactic dynamos

A dynamo consists of electrically conducting matter that moves in the presence of a magnetic field in such a way that the field is regenerated. It is generally accepted that magnetic fields in galaxies are generated through dynamo action. Detailed reviews of these processes can be found in e.g. Parker (1979); Moffatt (1978); Krause & Rädler (1980); Ruzmaikin et al. (1988). For spiral galaxies, mean-field dynamo models seem to explain the observed large scale magnetic structures rather well (see e.g. Ruzmaikin et al. 1988; Beck et al. 1996; Widrow 2002, for reviews). An alternative explanation for the observed structures is that they are a consequence of a pre-existing magnetic field being twisted by differential rotation in the galaxies and that no dynamo action is necessary. There are problems with this idea; there are no known mechanisms for obtaining fields of the observed strengths (Beck et al. 1996) and many authors have suggested that without regeneration the fields would be destroyed by turbulent diffusion over very short timescales (e.g. Ruzmaikin et al. 1988). For now, only dynamo action is able to consistently explain the observed field strengths, structures and timescales.

In the following, we briefly mention small scale dynamos before discussing the generation of the large scale regular fields.

2.5.1 Small scale dynamos

Fluctuations in the ISM should drive three-dimensional turbulence, which is capable of dynamo action for sufficiently large magnetic Reynolds numbers. The dynamo-generated magnetic field organizes itself into random flux tubes or sheets (e.g. Zeldovich et al. 1990; Brandenburg et al. 1995; Brandenburg & Subramanian 2005, and references therein). The structures are of the size of the correlation length of the flow. In Sect. 3.4, random helical forcing of the gas is used to produce this kind of dynamo action which

saturates due to the Lorentz force on the flow.

2.5.2 Mean-field models

In the standard galactic dynamo model (known as the $\alpha\omega$ dynamo), turbulent motions in the interstellar medium lift loops of toroidal field out of the galactic disc. These loops are twisted by the Coriolis effect into the poloidal direction, thus enhancing the poloidal field. The toroidal can then be regenerated by differential winding of the poloidal field. The key ingredients to such a dynamo are small scale turbulent motions, stratification and differential rotation. Dynamo action can occur at the scales of these turbulent motions and above. The mean-field approximation involves describing the effects of the turbulent motions at the scale of regular fields. Such an approach often neglects the back reaction of the magnetic field onto the fluid (e.g. via the Lorentz force), so that the problem is kinematic.

To obtain a general mean-field description, the velocity and magnetic fields are decomposed into mean ensemble averages ($\overline{\mathbf{B}}, \overline{\mathbf{U}}$) and small scale fluctuating components (\mathbf{b}, \mathbf{u}). We write

$$\mathbf{B} = \overline{\mathbf{B}} + \mathbf{b}, \quad \mathbf{U} = \overline{\mathbf{U}} + \mathbf{u}, \quad (2.35)$$

then insert \mathbf{B} and \mathbf{U} into the MHD induction equation (2.6). After ensemble averaging we obtain coupled equations for the mean and fluctuating components

$$\frac{\partial \overline{\mathbf{B}}}{\partial t} = \nabla \times (\overline{\mathbf{U}} \times \overline{\mathbf{B}}) + \nabla \times \mathcal{E} + \eta \nabla^2 \overline{\mathbf{B}}, \quad (2.36)$$

$$\frac{\partial \mathbf{b}}{\partial t} = \nabla \times (\mathbf{u} \times \overline{\mathbf{B}} + \overline{\mathbf{U}} \times \mathbf{b} + \mathbf{u} \times \mathbf{b} - \overline{\mathbf{u} \times \mathbf{b}}) + \eta \nabla^2 \mathbf{b}, \quad (2.37)$$

where \mathcal{E} is the mean electromotive force, $\mathcal{E} = \overline{\mathbf{u} \times \mathbf{b}}$, due to the turbulent motions. With further assumptions (see e.g. Krause & Rädler 1980, for some derivations), a suitable form of \mathcal{E} can be found. This can be written as

$$\mathcal{E}_i = \mathcal{E}_{i0} + \alpha_{ij} \overline{B}_j + \beta_{ijk} \frac{\partial \overline{B}_j}{\partial x_k}, \quad (2.38)$$

where higher order terms have been neglected and α and β are tensors that describe the small scale fluctuations in terms of properties of the interstellar medium. Enhancement of the mean (both toroidal and poloidal) field by turbulent motions is known as the α -effect. Expressions for α can be found in e.g. Ruzmaikin et al. (1988). With a mean-field model, an initially small seed magnetic field will grow exponentially. We

should expect that when the mean field strength becomes sufficiently large the effects of feedback onto the small scale processes will become significant. In nonlinear dynamo models, a traditionally used formulation for α is

$$\alpha = \frac{\alpha_k}{1 + \overline{B}^2/B_0^2}, \quad (2.39)$$

where α_k is the kinematic value of alpha, and B_0 is some reference magnetic field strength at which feedback is considered to be important. In many cases this will lead to the saturation of the dynamo when $\overline{B} \simeq B_0$. Assuming energy conservation, we would expect the energy in the mean magnetic field not to exceed the energy in the turbulent motions which generated it, therefore B_0 is often taken to be $B_0^2 = B_{\text{eq}}^2 = 4\pi\rho v_t^2$ i.e. the turbulent kinetic energy. This simple model of α -quenching lacks a physical description of the underlying processes. However, galactic dynamo models using this form of quenching have been very successful in obtaining magnetic fields compatible with observations in both structure and in the large scale field strengths of order B_{eq} .

Several authors have suggested that there are problems with the above form of α -quenching (e.g. Vainshtein & Cattaneo 1992; Kulsrud & Anderson 1992) and that the quenching should occur well below equipartition field strength (B_{eq}) values for mean-field galactic dynamos. This implies that galactic dynamo action can not easily be responsible for the large scale galactic magnetic fields, which are observed to be of a similar strength to the random fields. It is also suggested that the isotropic turbulent diffusivity (playing an important rôle in β) should be quenched, although perhaps not severely, with increasing \overline{B} . Some numerical simulations support this idea of ‘‘catastrophic’’ α -quenching, whereas other do not. It has been noted that the mean-field dynamos do not conserve magnetic helicity, whereas the magnetic induction equation (2.6) does, therefore magnetic helicity loss and transport in mean-field models has been the subject of more recent studies. Blackman & Field (2000) noted that that helicity loss through boundaries may be important for mean-field dynamos. Other authors have found ways of either avoiding the problem of helicity conservation locally or improving dynamo efficiency through helicity losses (e.g. Kleeorin et al. 2002; Shukurov et al. 2006). In such studies, detailed dynamical forms of α and β are employed in contrast to the simplistic algebraic forms traditionally adopted. One general conclusion common to these more detailed treatments is that the crude form of α -quenching in Eq. (2.39) is justified in that the ‘‘catastrophic’’ quenching problems suggested are avoided. It still remains a problem to find physically justified forms of α and β .

The effect of quenching β in galactic dynamos Eq. (2.38) was investigated in Klee-

orin et al. (2003) who found that within the range of models they tested, algebraic quenching of both the α and β was insufficient to saturate the growth of the mean field. With dynamical quenching for both parameters, a non-quenched component of β was required to obtain satisfactory solutions in a simple axisymmetric model. Overall, the effect of β -quenching was thought to produce satisfactory results that are not qualitatively different from those without β -quenching.

Another idea for generating the galactic large scale magnetic field, completely avoiding the scale separation idea of Eq. (2.35) (and therefore the issues of the nature of interstellar turbulence), was suggested by Parker (1992). This is by way of reconnection of the large scale magnetic field, driven by magnetic buoyancy and differential rotation, with the buoyancy facilitated by the pressure of cosmic ray gas. Hanasz et al. (2004) have demonstrated that such a dynamo can operate in numerical simulations, leading to strong field amplification. Moss et al. (1999b) incorporated this idea into an α -effect for the mean-field approach discussed above.

Overall, dynamo solutions for galaxies are often rather quite insensitive to those parameters that are poorly known, such as the form of the α -effect the turbulent magnetic diffusivity. In particular, for barred galaxies the determination of the magnetic field structure is dominated by large-scale velocity shear (Moss et al. 1998a, 2001), so the rôle of the α -effect is simply to maintain the field against decay. In Sect. 5.3 a mean-field dynamo model is used for the global magnetic field configuration in a spiral galaxy.

2.6 Cosmic rays

In the ISM of the Galaxy, with a field strength of a few μG , a proton of almost the highest observed energy will have a gyroradius much smaller than the largest scale of observed turbulent motions $L \simeq 100 \text{ pc}$ (a proton of 1 GeV in a magnetic field of $3 \mu\text{G}$ will have $r_g \approx 10^{12} \text{ cm}$). This suggests that the passage of the cosmic ray particles will be strongly affected by the structure of the galactic magnetic field. The cosmic rays appear almost isotropic near the Earth, i.e. they appear to fill the Galaxy. On the basis that their sources are low in number (based on the observed number of supernova remnants), this again suggests that the cosmic rays are affected by the medium they pass through; rather than streaming freely out of the Galaxy, their residence time is somehow increased (see e.g. Cesarsky 1980, for discussion of this problem). The dominant force on the cosmic rays is usually the Lorentz force, $q/c(\mathbf{v} \times \mathbf{B})$, where q is the charge of the particle. However, at the scale of the particle gyroradius, wave-

particle interactions occur which can become important. If cosmic rays stream along field lines much faster than the Alfvén speed, they excite resonant Alfvén waves which propagate along the magnetic field direction (see e.g. Kulsrud & Pearce 1969; Wentzel 1974). These amplified Alfvén waves are then in turn able to scatter the particles in pitch angle, which effectively limits the magnitude of the streaming velocity to not much more than the Alfvén speed (Skilling 1971). Alfvén waves generated by MHD turbulence can also scatter the cosmic rays, but these are not as effective as the self-generated waves naturally acquire efficient scattering properties. Farmer & Goldreich (2004) suggest that background anisotropic MHD turbulence could cause damping of the self-generated Alfvén waves, therefore indirectly enabling at least some of cosmic rays to stream freely. In the ISM, partially ionized warm regions could lead to ion-neutral damping (Kulsrud & Pearce 1969), which would have probably lead to similar enhancement of cosmic ray streaming (see e.g. Felice & Kulsrud 2001 and references therein).

A transport equation for a particular cosmic ray species can be derived from the collisionless Boltzmann equation (e.g. Skilling 1975a). Following Skilling’s method, this is done by transforming the distribution function $f(\mathbf{p}, \mathbf{x}, t)$ (for particle momentum \mathbf{p}) to the frame of the resonant Alfvén waves, then averaging over the gyrophase to eliminate the Lorentz force. At the lowest, dominant order, the resulting equation for the distribution function f is isotropic and can be written (back in the rest frame)

$$\frac{\partial f}{\partial t} + \mathbf{v} \cdot \nabla f = \nabla \cdot (\mathbf{D} \nabla f) + \frac{p}{3} \nabla \cdot \mathbf{v} \frac{\partial f}{\partial p} + Q(\mathbf{x}, p, t) \quad (2.40)$$

where Q is a source term, \mathbf{D} is a spatial diffusion tensor and $\mathbf{v} = \mathbf{u} + \mathbf{u}_w$, with \mathbf{u} the background gas velocity and \mathbf{u}_w the field-aligned component of the Alfvén wave velocity. This derivation assumes that some scattering by Alfvén waves occurs. It is the same equation as derived by Parker (1965) and other authors in various forms. Assuming a power law distribution (as is observed) for relativistic electrons of the form $f(p) \propto p^{-q}$, this equation can be simplified to simulate electron transport (Jun & Jones 1999). Without such simplifications, detailed numerical calculations for the galactic cosmic ray number density per unit momentum (via an equation derived directly from the above equation) have been performed by Strong & Moskalenko (1998). Both of these approaches do not consider the dynamical effects of the cosmic rays on the background gas or the magnetic field (and in only one is the field considered to be time dependent). The observed spectrum implies that the dynamically important cosmic rays are the low energy ones, consisting of mainly protons.

An equation for the energy density of cosmic rays can be obtained by multiplying (2.40) by the kinetic energy of particles and integrating over momentum. This equation for the energy density e_c is

$$\frac{\partial e_c}{\partial t} + \nabla \cdot (e_c \mathbf{v}) + p_c \nabla \cdot \mathbf{v} = \nabla \cdot (\mathbf{K} \nabla e_c) + Q_c, \quad (2.41)$$

where \mathbf{K} is an energy weighted diffusion tensor (see e.g. Ryu et al. 2003), p_c is the cosmic ray pressure and Q_c is another source/sink term. We assume that the cosmic rays are an ideal gas, i.e. $\gamma_c = 1 + p_c/e_c$, with $\gamma_c \simeq 4/3$ for relativistic protons. In this approach γ_c , \mathbf{K} etc. can not (easily) be prescribed in a self-consistent way and the evolution of the distribution function cannot be followed. The cosmic ray energy density is

$$e_c = 4\pi m c^2 \int_{p_0}^{p_1} p^2 \left(\sqrt{p^2 + 1} - 1 \right) f(\mathbf{x}, p, t) dp,$$

where p here is in units of mc and p_0 , p_1 represent some momentum interval. The details of such values are largely unimportant in this approach.

This hydrodynamic form is often coupled to the MHD equations and is usually referred to as the “two-fluid” model (Drury & Völk 1981; Jun et al. 1994; Hanasz & Lesch 2003). Most cases neglect the Alfvén wave field described above and simply take $\mathbf{v} = \mathbf{u}$. In some applications, where deemed appropriate, authors have prescribed an additional equation that follows the Alfvén wave energy and model the wave velocity \mathbf{u}_w (two examples are Breitschwerdt et al. 1991; Jones 1993). In most cases, it is assumed that the collective effects of exchange between the Alfvén waves and cosmic rays can be taken as a macroscopic pressure acting isotropically on the background gas (e.g. Wentzel 1974). Achterberg (1981) explicitly derives such an expression for the total pressure acting on the background gas as a sum of cosmic ray and Alfvén wave pressure. In the Galactic disk, MHD wave propagation direction should be (on average) isotropic with respect to field lines, so the inclusion of just this pressure gradient in a momentum equation for the background gas seems justified.

The anisotropic diffusion tensor, \mathbf{K} , is usually written in the form

$$K_{ij} = K_{\perp} \delta_{ij} + (K_{\parallel} - K_{\perp}) \hat{B}_i \hat{B}_j, \quad (2.42)$$

where K_{\perp} and K_{\parallel} are the diffusion coefficients perpendicular and parallel to the field, respectively. Estimates for K_{\parallel} seems to be consistently about $10^{27} - 10^{29} \text{ cm}^2 \text{ s}^{-1}$. These estimates have been made from both theory (see e.g. Berezhinskii et al. 1990; Felice & Kulsrud 2001) and making comparisons of observations with simulations (Strong &

Moskalenko 1998). Estimating the relative size of K_{\perp} to field aligned value K_{\parallel} has been an issue for some time. It is widely thought that it depends on the ratio of turbulent to regular field strengths (or the turbulence level). Perhaps the most detailed estimate come from Monte Carlo simulations for test particles in turbulent magnetic fields. The simulations of Giacalone & Jokipii (1999) suggest $K_{\perp}/K_{\parallel} = 0.02$, applicable to at least some energy range of galactic cosmic rays. Casse et al. (2002) extend on this slightly and are able to express the result in terms of the turbulence level. These simulations lack some of the interactions between waves and particles but are able to look at scattering of realistic magnetic irregularities. The estimates for K_{\perp}/K_{\parallel} obtained are larger than theory predicts, partly because particles are able to cross between tangled field lines effectively, which has not been assumed in most theory.

Many studies of the Parker instability as well as recent simulations of the galactic dynamo rely on a hydrodynamic description of cosmic rays which is especially convenient in models involving the large-scale dynamics of the interstellar medium.

Chapter 3

Propagation of cosmic rays in turbulent magnetic fields

3.1 Introduction

The work of this section was done together with Axel Brandenburg.

Our aim here is to use a hydrodynamic approach in order to clarify the relation between cosmic ray energy density and properties of the interstellar medium, in particular with regards to pressure balance (or energy equipartition) with the magnetic field. The idea of overall (statistical) pressure balance in the ISM would be more difficult to maintain if both magnetic and cosmic ray pressures are enhanced or reduced at the same positions simultaneously. Padoan & Scalo (2005) suggest that if the streaming velocity of cosmic rays is proportional to the Alfvén speed (Felice & Kulsrud 2001; Farmer & Goldreich 2004, and references therein), then the local cosmic ray density is independent of the local magnetic field strength and scales with the square root of the (ionized) gas density. Indeed, if both the magnetic flux and the cosmic ray flux are conserved, $BS = \text{const}$ and $n_c US = \text{const}$ (where B is the magnetic field strength, S is the area within a fluid contour, n_c is the number density of cosmic rays and U is their streaming velocity), one obtains $n_c U/B = \text{const}$, which yields $n_c \propto n_i^{1/2}$, given that $U = V_A \propto B n_i^{-1/2}$, with n_i the ion number density and V_A the Alfvén speed.

Here we use the two-fluid model outlined in Sect. 2.6, where cosmic rays are described by an equation for their pressure (or energy density) and an equation of state.

We want to know which processes are responsible for controlling the cosmic ray energy density and what is the relation of cosmic ray energy density to the magnetic field. Is there any equipartition in their energy densities, either locally, or globally on the scale of the galaxy? In addition, it is interesting to understand the dynamical effects of the cosmic rays on the ISM. We begin with the governing equations and discuss issues that arise in connection with the numerical implementation of cosmic ray diffusion along magnetic field lines.

3.2 Method

3.2.1 Cosmic ray hydromagnetic equations

The hydromagnetic equations supplemented by the advection-diffusion equation for the cosmic ray energy density, and the cosmic ray pressure contribution in the momentum equation, are

$$\frac{\partial \rho}{\partial t} + \nabla \cdot (\rho \mathbf{u}) = 0, \quad (3.1)$$

$$\frac{\partial e_c}{\partial t} + \nabla \cdot (e_c \mathbf{u}) + p_c \nabla \cdot \mathbf{u} = D_c + Q_c, \quad (3.2)$$

$$\frac{\partial e_g}{\partial t} + \nabla \cdot (e_g \mathbf{u}) + p_g \nabla \cdot \mathbf{u} = D_g + Q_k + Q_m, \quad (3.3)$$

$$\frac{\partial \rho \mathbf{u}}{\partial t} + \nabla \cdot (\rho \mathbf{u} \mathbf{u}) + \nabla (p_g + p_c) = \mathbf{J} \times \mathbf{B} + \mathbf{f} + \mathbf{F}, \quad (3.4)$$

$$\frac{\partial \mathbf{B}}{\partial t} = \nabla \times (\mathbf{u} \times \mathbf{B} - \eta \mu_0 \mathbf{J}), \quad (3.5)$$

where ρ , \mathbf{u} , e_g and p_g are the gas density, velocity, internal energy and pressure; e_c and p_c are the cosmic ray energy density and pressure, Eq. (3.5) is the induction equation for the magnetic field \mathbf{B} , $\mathbf{J} = \nabla \times \mathbf{B} / \mu_0$ is the electric current density, η is the magnetic diffusivity, $D_g = \nabla \cdot (K \nabla T)$ is the thermal diffusion term (with thermal diffusivity K , treated isotropically here; thermal diffusion is unimportant in the present context, but weak diffusion is necessary in the numerical implementation). Further, T is the temperature related to the internal energy density, e_g , via $e_g = \rho c_v T$ (where c_v is the specific heat capacity at constant volume) and D_c is the divergence of the diffusive cosmic ray energy flux taken with the opposite sign, i.e.

$$D_c = -\nabla \cdot \mathcal{F}_c. \quad (3.6)$$

The usual approach is to treat this term using a Fickian diffusion model, i.e., to assume that the flux is proportional to the instantaneous gradient of the cosmic ray energy density,

$$\mathcal{F}_{ci} = -K_{ij} \partial_j e_c \quad (\text{Fickian diffusion}), \quad (3.7)$$

where K_{ij} is the diffusion tensor. The latter can be written as

$$K_{ij} = K_{\perp} \delta_{ij} + (K_{\parallel} - K_{\perp}) \hat{B}_i \hat{B}_j, \quad (3.8)$$

where $\hat{\mathbf{B}} = \mathbf{B} / |\mathbf{B}|$ is the field-aligned unit vector (see Sect. 2.6). Here, K_{\parallel} and K_{\perp} are the cosmic ray diffusion coefficients along and perpendicular to the magnetic field, respectively. We take both coefficients to be simply an appropriate constant, rather than attempt to prescribe them in a self-consistent manner.

We assume ideal-gas equations of state for both the cosmic rays and the gas, i.e. $p_c = (\gamma_c - 1)e_c$ and $p_g = (\gamma_g - 1)e_g$, where γ_c and γ_g are the ratios of the total number of degrees of freedom to the number of translational degrees of freedom for the cosmic rays and the gas. Unless stated otherwise, we shall take $\gamma_c = 4/3$ and $\gamma_g = 5/3$. Other choices for γ_c include $5/3$ and $14/9$ (e.g. Ryu et al. 2003, and references therein).

The system can be driven by an external force \mathbf{f} in the momentum equation (3.4), and \mathbf{F} in that equation includes additional forces such as the viscous force, $\nabla \cdot (2\nu \rho \mathbf{S})$,

where ν is the viscosity and $S_{ij} = \frac{1}{2}(u_{i,j} + u_{j,i}) - \frac{1}{3}\delta_{ij}u_{k,k}$ is the traceless rate of strain tensor, where commas denote partial differentiation. Furthermore, $Q_k = 2\rho\nu\mathbf{S}^2$ and $Q_m = \eta\mu_0\mathbf{J}^2$ denote the viscous and Joule heating, and Q_c is a cosmic ray energy source.

3.2.2 Non-Fickian diffusion

Typical values of the diffusivity along the magnetic field are of the order $10^{28} \text{ cm}^2 \text{ s}^{-1}$ (e.g. Berezhinskii et al. 1990). Such large values could possibly limit numerical modelling since a large diffusivity implies that the computational time step should be small to ensure numerical stability; for example simulations with a resolution of 1 pc would require a time step of 10 years or less (e.g., Hanasz & Lesch 2003 reduce K_{\parallel} by a factor of 10 to make the system tractable numerically). This problem could be avoided by employing an implicit numerical scheme. (In the context of cosmic ray propagation, one would expect the advection speed to be not too much larger than the Alfvén speed, so that an explicit numerical scheme would be sufficient to handle this term.) However, before discussing a way to remedy the time stepping problem we note that in the case of field-aligned diffusion, there is another problem that is potentially more severe. If we use the product rule and write $D_c = \partial_i(K_{ij}\partial_j e_c)$ in the form

$$D_c = -\mathbf{U}_c \cdot \nabla e_c + K_{ij}\partial_i\partial_j e_c, \quad (3.9)$$

we see that $U_{ci} = -\partial K_{ij}/\partial x_j$ plays the rôle of a velocity transporting cosmic rays perpendicular to curved field lines. This term is proportional to the divergence of the dyadic product of unit vectors, $\nabla \cdot (\widehat{\mathbf{B}}\widehat{\mathbf{B}})$. At magnetic X-points, this term is singular, as explained below (we note that O-type singular magnetic points do not cause difficulties).

We illustrate this complication using a simple magnetic field configuration $\mathbf{B} = (x, -y, 0)^T$ with a null point at the origin, which leads to the singular behaviour of $\nabla \cdot (\widehat{\mathbf{B}}\widehat{\mathbf{B}})$, and hence to a singularity of $|\mathbf{U}_c|$:

$$\nabla \cdot (\widehat{\mathbf{B}}\widehat{\mathbf{B}}) = \frac{1}{r^4} \begin{pmatrix} (3y^2 - x^2)x \\ (3x^2 - y^2)y \\ 0 \end{pmatrix},$$

where $r^2 = x^2 + y^2$. This expression diverges at the origin and leads to infinite propagation speed which would, technically speaking, limit to zero the length of the time step of an explicit time stepping scheme. In spite of this singularity, the cosmic ray

energy density must stay finite. In fact, one can show that, in a closed or periodic domain, the maximum cosmic ray energy density, $\max(e_c)$, can only decrease with time. This is a well-known general property of the diffusion operator; in Appendix A we derive this result for the form of the diffusion tensor of Eq. (3.8). The reason that $\max(e_c)$ can remain finite, despite $\nabla \cdot (\widehat{\mathbf{B}}\widehat{\mathbf{B}})$, and hence \mathbf{U}_c , becoming infinite, is that the parabolic system of equations can adjust itself instantaneously so that ∇e_c tends to zero where \mathbf{U}_c diverges. This does not resolve the time stepping problem, however. In Sect. 3.2.4 we demonstrate a remedy to this X-point problem using a non-Fickian diffusion model. In the following we describe this non-Fickian approach in more detail. A physically appealing, and widely adopted way to improve the diffusion equation so as to limit the propagation speed to a finite value involves a more accurate description of the diffusive flux. This generalization has been applied, e.g., to turbulent diffusion. In turbulence, the classical turbulent diffusion equation, $\partial n/\partial t = D \partial^2 n/\partial x^2$, arises if the turbulent velocity field is assumed to be δ -correlated in time; this approximation is consistent with Eq. (3.7) or its simplifications. In order to ensure finite propagation speed of the diffusing substance, it is sufficient to allow for a finite correlation time τ of the velocity field. This leads to equation (3.10) for the diffusive flux. The corresponding equation for the diffusing quantity reduces to the telegraph equation $\partial n/\partial t + \tau \partial^2 n/\partial t^2 = D \partial^2 n/\partial x^2$, or its generalizations. These arguments have been recently discussed by Bakunin (2003b,a). The telegraph equation has been used to correct acausal cosmic-ray diffusion models (e.g., Gombosi et al. 1993). This type of non-Fickian diffusion also emerges quite naturally in turbulent diffusion of passive scalars (Blackman & Field 2003) and has been confirmed in direct simulations (Brandenburg et al. 2004). On long enough time scales, or for sufficiently small values of τ , the non-Fickian description of diffusion reduces to the Fickian limit.

Thus, we replace Eq. (3.7) by

$$\frac{\partial \mathcal{F}_{ci}}{\partial t} = -\tilde{K}_{ij} \nabla_j e_c - \frac{\mathcal{F}_{ci}}{\tau} \quad (\text{non-Fickian diffusion}), \quad (3.10)$$

where $K_{ij} = \tau \tilde{K}_{ij}$ corresponds to the original diffusion tensor. Similarly to Eq. (3.8), we write

$$\tilde{K}_{ij} = \tilde{K}_\perp \delta_{ij} + (\tilde{K}_\parallel - \tilde{K}_\perp) \widehat{B}_i \widehat{B}_j.$$

Quantitatively, the deviation from Fick's law is controlled by the dimensionless parameter

$$\text{St} = \frac{\tilde{K}_\parallel^{1/2} \tau}{\ell} = \frac{(K_\parallel \tau)^{1/2}}{\ell}, \quad (3.11)$$

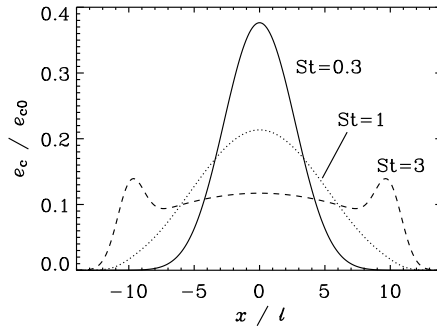


Figure 3.1: The spread of an initial Gaussian distribution of cosmic ray energy density (of a half-width ℓ): the distribution at a time $t = 1$ is shown, as a function of x/ℓ , for three values of the Strouhal number St . Note that the behaviour of the solution becomes more wave-like as St increases.

where ℓ is the typical length scale of the initial structure. In the context of turbulent diffusion, this dimensionless parameter is often referred to as the Strouhal number (Landau & Lifshitz 1987; Krause & Rädler 1980). The larger the Strouhal number, the more important are non-Fickian effects resulting in a wave-like behaviour of the solution. Unlike the solution of the classical diffusion equation, where an initial perturbation to the trivial solution has an effect at every position for any $t > 0$, solutions with non-Fickian diffusion remain unperturbed ahead of a propagating front.

A suitable estimate of the Strouhal number can be obtained assuming that the relevant correlation time is of the order of the Alfvén crossing time for magnetic structures of scale ℓ , i.e. $St \simeq (K_{\parallel}/V_A\ell)^{1/2}$. This yields (for gas number density 0.1 cm^{-3})

$$St \simeq 20 \left(\frac{K_{\parallel}}{4 \times 10^{28} \text{ cm}^2/\text{s}} \right)^{\frac{1}{2}} \left(\frac{B}{5 \mu\text{G}} \right)^{-\frac{1}{2}} \left(\frac{\ell}{10 \text{ pc}} \right)^{-\frac{1}{2}}. \quad (3.12)$$

In Fig. 3.1 we illustrate the one-dimensional spread of an initial Gaussian distribution of cosmic rays, $e_c = \exp(-\frac{1}{2}x^2/\ell^2)$ after $t = \tau$ for three values of St . For small values of St , the solution evolves similarly to that of the diffusion equation (solid and dotted lines in Fig. 3.1). For large values of St , the distribution of cosmic rays develops two local maxima of e_c that propagate outwards as shown with dashed line, a typical wave-like behaviour. In the limiting case of very large values of St the governing equation reduces to the wave equation, and the classical diffusion is recovered for $St \rightarrow 0$.

In some sense, the extra time derivative in the non-Fickian formulation plays a rôle similar to that of the displacement current in electrodynamics. In simulations of hydromagnetic flows at low density, where the Alfvén speed can be very large, the

displacement current can be included with an artificially reduced value of the speed of light in order to limit the Alfvén speed to numerically acceptable values (Miller & Stone 2000).

3.2.3 Numerics

In the following, we use the `PENCIL CODE`,¹ a non-conservative, high-order, finite-difference code (sixth order in space and third order in time) for solving the compressible hydromagnetic equations. The non-Fickian diffusion formulation (in which we solve Eq. (3.10) explicitly) is invoked by using the `cosmicrayflux` module, in addition to the `cosmicray` module for the advection-diffusion equation. As with most parts of the code, these modules are switchable, so we may choose not to solve for the flux vector field when using a simplified diffusion tensor. Whenever possible we display the results in non-dimensional form, normalizing in terms of physically relevant quantities. In all other cases we display the results in code units, which means that velocities are given in units of the sound speed c_s , length is given in units of k_1^{-1} (related to the scale of the box), density is given in units of the average density ρ_0 , and magnetic field is given in units of $\sqrt{\mu_0 \rho_0} c_s$. The units of all other quantities can be worked out from these. For example, the unit of Q_c is $\rho_0 c_s^3 k_1$. For the interstellar medium with $\rho_0 = 10^{-24} \text{ g cm}^{-3}$, $c_s = 10 \text{ km s}^{-1}$, and $k_1 = 2\pi/100 \text{ pc}$, the unit of the cosmic ray injection rate is $3 \times 10^{-26} \text{ erg cm}^{-3} \text{ s}^{-1}$, which is about 10% of the rate of energy injection by supernovae in the galactic disc (Mac Low & Klessen 2004). For these values, the unit for diffusivity will be $c_s k_1^{-1} \approx 5 \times 10^{25} \text{ cm}^2 \text{ s}^{-1}$.

A comment regarding centred finite difference schemes is here in order. In the steady state, the discretization of the cosmic ray diffusion model given by Eqs (3.6) and (3.10) corresponds essentially to a conservative formulation of the diffusion term. (A conservative formulation involving a direct discretization of ∇^2 is not possible with a non-staggered mesh, because two first-order derivatives occur in two separate equations.) As is well known, the discretization of the diffusion term on a centred non-staggered mesh means that structures at the mesh scale cannot be diffused (the discretization error for first derivatives becomes infinite). Therefore, we need to include weak Fickian diffusion in the cosmic ray energy equation. We refer to the corresponding (isotropic) diffusion coefficient as K_{Fick} , and it will be chosen to be comparable to or less than the viscous and magnetic diffusivities.

¹<http://www.nordita.dk/software/pencil-code>

3.2.4 A remedy for cosmic ray diffusion near a magnetic X-point

We test our field-aligned non-Fickian diffusion procedure by simulating in two dimensions a magnetic field configuration similar to the X-point discussed in Sect. 3.2.2. In order to be able to impose normal-field boundary conditions, $\hat{\mathbf{n}} \times \mathbf{B} = 0$ at the domain boundaries, we modify the field to $\mathbf{B} = (\sin k_1 x, -\sin k_1 y, 0)^T$, where k_1 is the smallest wavenumber in a periodic domain. So, for $k_1 = 1$ we consider the domain $-\pi < (x, y) < \pi$. The initial distribution of the cosmic ray energy density is $e_c = x$, which has a constant gradient and therefore, with Fickian diffusion, $D_c = \nabla \cdot (\hat{\mathbf{B}}\hat{\mathbf{B}})$ would have a singularity initially. However, in the non-Fickian approach D_c is not calculated as in Eq. (3.9), which resolves this problem. The evolution of e_c for $\tau = 0.1$ is shown in Fig. 3.2 together with vectors showing the magnetic field. Note that the gradient of e_c becomes small in the neighbourhood of the singularity of $\nabla \cdot (\hat{\mathbf{B}}\hat{\mathbf{B}})$ at the origin, so the otherwise singular term that multiplies ∇e_c has no effect on e_c , as desired. In the case of the Fickian diffusion, the same final solution would have been obtained, but the initial reduction of the gradient in e_c would have involved an infinitely large advection speed U_c (i.e. we can not obtain this solution using Eq. (3.7) for the diffusive flux in our numerical scheme). In the non-Fickian approach, the maximum propagation speed is $\tilde{K}_{\parallel}^{-1/2}$, thereby alleviating the numerical time step problem.

Another example of field-aligned diffusion is shown in Fig. 3.3, where the magnetic field is given by $\mathbf{B} = \mathbf{B}_0 + \nabla \times \mathbf{A}$ with $\mathbf{B}_0 = 0.1\hat{\mathbf{x}}$ and $\mathbf{A} = 0.1\hat{\mathbf{z}} \cos(k_x x) \cos(k_y y)$ with $k_x = 4k_1$ and $k_y = k_1$. Again, this magnetic field is held constant in time. The initial profile of $e_c \propto \exp(-r^2/2\sigma^2)$, with $r^2 = x^2 + (y + 0.5)^2$, is a two-dimensional Gaussian of a half-width of $\sigma = 0.07$, positioned at $(0, -0.5)$. We confirm that our implementation of cosmic ray diffusion allows us to model reliably rather complicated magnetic configurations. The lower panel of Fig. 3.3 confirms that, for large values of the Strouhal number, the wave nature of the telegraph equation manifests itself and e_c develops two waves propagating away from the initial maximum (similar to the dashed line in Fig. 3.1).

3.3 Macroscopic evolution of the cosmic ray gas

3.3.1 Energy balance

In a closed domain, mass is conserved, i.e. $\langle \rho \rangle \equiv \rho_0 = 1$, where angular brackets denote volume averaging. The cosmic ray hydromagnetic equations (3.1)–(3.5) then lead to the following set of equations for the cosmic ray energy $E_c = \langle e_c \rangle$, the gas energy

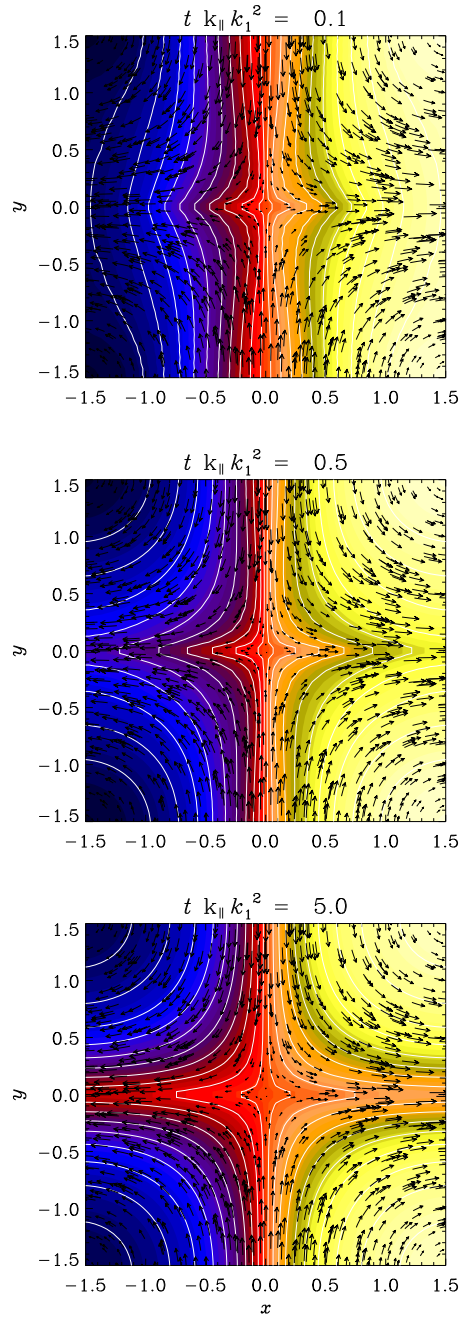


Figure 3.2: Evolution of the cosmic ray energy density near a magnetic X-point: snapshots of e_c (shown as contours and shades of colour) for field-aligned diffusion along a fixed magnetic field $\mathbf{B} = (\sin k_1 x, -\sin k_1 y, 0)^T$ (shown as vectors) displayed for three times indicated at the top of each frame. Increasing cosmic ray energy density is represented with increasing lightness of colour i.e. the minimum is dark blue/black and the maximum is pale-yellow.

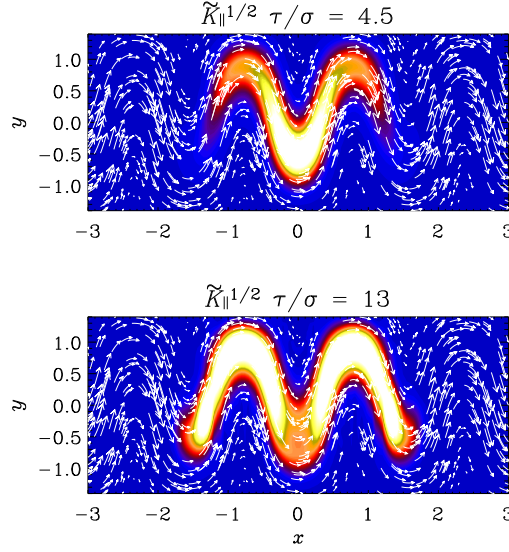


Figure 3.3: Magnetic field vectors together with a colour scale representation of e_c in a kinematic calculation with 128^2 mesh points, for different values of a Strouhal number $St = K_{\parallel}^{1/2} \tau / \sigma$, with $\tilde{K}_{\perp} = 0$, $\tilde{K}_{\parallel} = 10^{-1}$, and $K_{\text{Fick}} = 10^{-3}$, at time $t/\tau = 1$ for two different values of τ ($=1$ and 3 , respectively). (Only part of the computational domain in the y direction is shown.) The bright yellow/white colour corresponds to the maximum density and blue the minimum.

$E_g = \langle e_g \rangle$, the kinetic energy $E_k = \langle \frac{1}{2} \rho \mathbf{u}^2 \rangle$, and magnetic energy $E_m = \langle \mathbf{B}^2 \rangle / 2\mu_0$,

$$\frac{dE_c}{dt} = -W_c + \langle Q_c \rangle, \quad (3.13)$$

$$\frac{dE_g}{dt} = -W_g + \langle Q_k \rangle + \langle Q_m \rangle, \quad (3.14)$$

$$\frac{dE_k}{dt} = W_c + W_g + W_m + W_f - \langle Q_k \rangle, \quad (3.15)$$

$$\frac{dE_m}{dt} = -W_m - \langle Q_m \rangle. \quad (3.16)$$

Here, all the energies are referred to the unit volume. The terms $W_c = \langle p_c \nabla \cdot \mathbf{u} \rangle$, $W_g = \langle p_g \nabla \cdot \mathbf{u} \rangle$, $W_m = \langle \mathbf{u} \cdot (\mathbf{J} \times \mathbf{B}) \rangle$, and $W_f = \langle \mathbf{u} \cdot \mathbf{f} \rangle$ result from work done against cosmic ray pressure, gas pressure, the Lorentz force, and the external forcing, respectively. Terms responsible for viscous and Joule heating and the cosmic ray energy source are simply given by the volume integrated terms in the original equations. Equations (3.13)–(3.16) imply that the total energy, $E_{\text{tot}} = E_c + E_g + E_k + E_m$, satisfies the simple conservation law

$$\frac{dE_{\text{tot}}}{dt} = \langle Q_c \rangle + W_f.$$

Thus, the only sources of energy are the injection of cosmic rays and the external forcing of the turbulence. In the following section we demonstrate how E_c can be enhanced by the conversion of kinetic energy.

3.3.2 Compressional enhancement of cosmic ray energy

We assume $Q_c = W_f = 0$ and that there is initially kinetic energy that is later redistributed among gas and cosmic rays. We investigate, using a simple one-dimensional model ($\partial/\partial y = \partial/\partial z = 0$), how much energy can be converted into cosmic ray energy via the W_c term responsible for work done against cosmic ray pressure. As the initial condition, we use a sinusoidal perturbation of u_x and $\ln \rho$ with unit amplitude and $E_c = E_{c0} = 1$, $E_g = 1.8$, and $E_k = 0.21$. The evolution of velocity, cosmic ray and gas energies, as well as the entropy of the gas are shown in Fig. 3.4. Here the entropy s is defined as $s = c_v \ln(c_s^2/\rho_g^{\gamma-1})$, where $c_s^2 = \gamma(\gamma-1)e_g$ is the gas sound speed squared. It turns out that in this case about 78% of the kinetic energy is transformed into cosmic ray energy and only 22% into thermal energy. This result is, however, sensitive to the phase shift between density and velocity: if the density is initially uniform (keeping all other parameters unchanged), the fractional energy going into cosmic rays is only 23 percent, whilst 77 per cent converts into thermal energy.

These results demonstrate that, at least in principle, a sizeable fraction of the kinetic energy can be converted into cosmic ray energy. Similar experiments have been made in earlier work with a similar model in the context of shock acceleration of cosmic rays (see, e.g., Drury & Völk 1981; Jun et al. 1994). In particular Kang & Jones (1990) showed that the efficiency of conversion varies strongly with γ_c . However, the conversion of kinetic energy into cosmic ray energy requires a background of cosmic ray energy. Decreasing E_c from 1 to 0.1 lowers the fraction of compressionally produced cosmic ray energy density from 78% to 21%. In contrast to dynamo theory where a weak seed magnetic field is sufficient to produce equipartition magnetic fields (albeit only in three dimensions), there is no such mechanism for the cosmic ray energy. This is related to the anti-dynamo theorem for scalar fields (Krause 1972). However, for three-dimensional compressible flows an exponential dynamo-like amplification of a passive scalar is in principle possible if the passive scalar is represented by inertial particles (Elperin et al. 1996). Such a mechanism can work because inertial particles do not feel a pressure gradient. This can lead to particle accumulation in temperature minima (Elperin et al. 1997) and in vortices (Barge & Sommeria 1995; Hodgson & Brandenburg 1998; Johansen et al. 2004). However, here cosmic ray particles are treated as non-inertial particles.

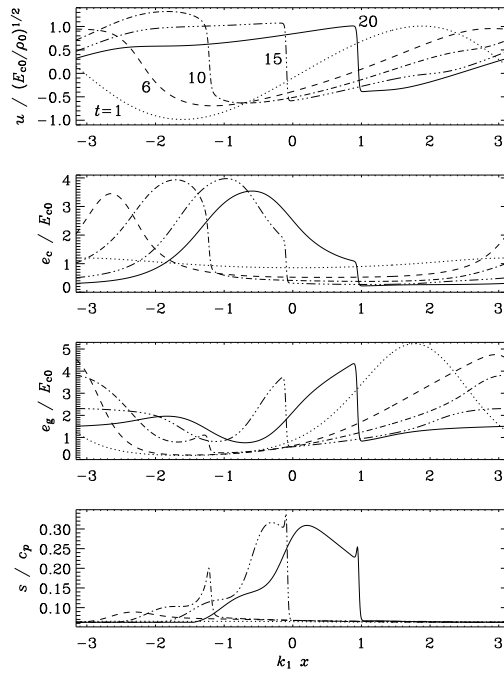


Figure 3.4: Velocity, cosmic ray and gas energy densities, and entropy in an experiment with a non-linear sound wave that piles up to a shock ($\gamma_c = 5/3$). Note the significant conversion of kinetic energy into cosmic ray energy. The conversion into gas energy is comparatively small even though there is noticeable entropy enhancement due to the shock. Curves obtained for different times are shown with different line types as labelled in the first panel. Time is given in units of $k_1^{-1}(E_{c0}/\rho_0)^{-1/2}$.

3.3.3 Effect of cosmic ray pressure

Cosmic rays can be confined at large scales by magnetic tension, where a strong magnetic field can more easily withstand deformation driven by cosmic ray pressure gradients. This could provide a natural mechanism for producing equipartition between cosmic rays and the magnetic field. This feature can be simulated in two dimensions in a doubly periodic domain $-\pi < (x, y) < \pi$, with $k_1 = 1$. The results are illustrated in Fig. 3.5, where we have a magnetic tube in $1 < y < 2$ with its axis along the x direction. We have implemented two local cosmic ray sources with the total energy injection profile

$$Q_c = Q_{c0} \sum_{i=1}^2 \exp \left\{ -\frac{x^2 + (y - y_i)^2}{2R^2} \right\},$$

i.e., both located on the y axis, centred at $y_1 = 0$ and $y_2 = \pi/2$; the initial half-width for both sources is $R = 0.13$, so that one source is within the magnetic tube and the other, outside it. In this experiment, cosmic ray diffusion is negligible ($\tilde{K}_{\parallel} = \tilde{K}_{\perp} = 0$ and $K_{\text{Fick}} = 0.01$) as we intend to explore the effects of cosmic ray pressure alone. As expected, expansion proceeds nearly isotropically outside the magnetic structure, but the cosmic ray energy density is channelled preferentially along field lines inside the tube. At the end of the run, the aspect ratio of the cosmic ray distribution is about two to one inside the tube. For values of Q_c significantly larger than about 10, the gas density decreases strongly so as to maintain pressure equilibrium and oppose expansion driven by cosmic rays.

This confirms that cosmic ray dynamics can be strongly affected by the approximate pressure balance in the ISM.

3.3.4 Cosmic rays in a partially ordered magnetic field

In this section we briefly explore the effects of a random magnetic field on the evolution of the cosmic ray gas. A random component of the interstellar magnetic field can facilitate the isotropic spreading of cosmic rays across the large-scale, preferentially horizontal magnetic field in the Galactic disc. In addition, a turbulent magnetic field can enhance cosmic ray diffusion by destroying the compound diffusion effect (Ptuskin 1979; Kóta & Jokipii 2000, and references therein) due to the exponential local divergence of magnetic lines.

To allow for cosmic ray losses through the x boundaries, we relax the assumption of periodicity in that direction. At $x = \pm\pi$, we assume $e_c = 0$, together with $\partial\rho/\partial x = \partial e_g/\partial x = 0$. This implies that cosmic rays may be lost from the domain but gas may

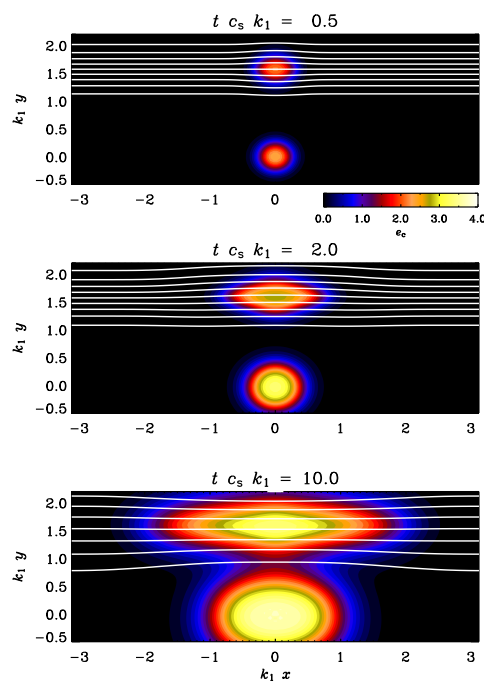


Figure 3.5: Cosmic ray energy density at times indicated at the top of each panel. Cosmic rays expand from two sources (with injection rate $Q_c = 10$ for each), one inside a magnetic flux tube and the other one outside. Magnetic lines are shown with white solid curves whose density is proportional to the field strength.

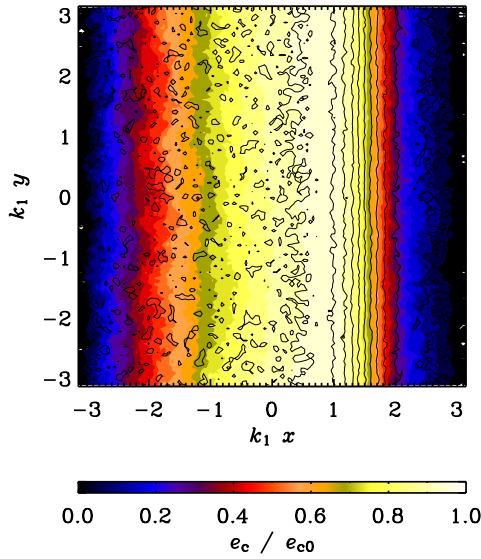


Figure 3.6: Cosmic ray energy density (colour/grey scale coded, with darker/blue shades corresponding to smaller values) together with magnetic field lines (solid) in a two-dimensional simulation with a fixed magnetic flux tube centred around $x = 1.5$ and a random magnetic field superimposed on it. Here, $\tilde{K}_{\parallel} = 0.1$, $\tilde{K}_{\perp} = 0$, and $\tau = 3$.

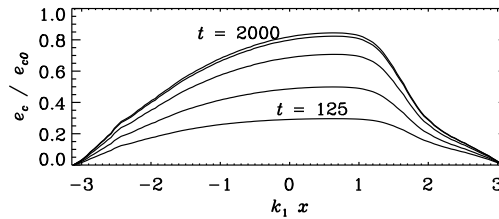


Figure 3.7: Cosmic ray energy density from the model of Fig. 3.6 averaged in the y direction for times 125×2^n with $n = 0, \dots, 4$. The magnetic tube is located at $x = 1.5$ leading to an asymmetric distribution of cosmic ray energy density.

not. In the y direction we again use periodic boundary conditions.

We consider a two-dimensional system with a regular magnetic field \mathbf{B}_0 directed along the y -axis and confined to a flux tube as shown in Fig. 3.6, where the field strength has a profile $B_0 \propto \text{sech}^2[(x - 1.5)/0.5]$. An isotropic random magnetic field $\delta\mathbf{B}$ is superimposed on \mathbf{B}_0 , with $\overline{\delta B^2}/B_0^2 = 1$ at $x = 1.5$ where B_0 is maximum; the magnetic field does not evolve. The random magnetic field is implemented in terms of a magnetic vector potential given as white noise with Gaussian probability density which, because of two dimensions, implies a k^3 power spectrum for the magnetic energy. We also assume zero velocity for all times, so we just advance Eqs (3.2) and (3.10) in time, using Eq. (3.6). Cosmic rays are injected at a constant rate across the domain, $Q_c = \text{const}$.

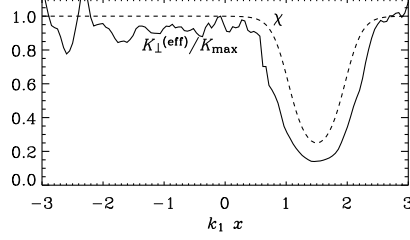


Figure 3.8: The profile of $K_{\perp}^{(\text{eff})}$ (solid) obtained from Eq. (3.18) using e_c corresponding to the upper curve of Fig. 3.7, and $\chi = 3\overline{B_x^2}/\overline{B_y^2}$ (dashed), where B_y has both large-scale and random parts, whereas B_x is a purely random magnetic field. Here, $K_{\text{max}} = 0.023$ is the maximum value of $K_{\perp}^{(\text{eff})}$.

In Fig. 3.6 we show the result of such a calculation with $\tilde{K}_{\perp} = 0$; the distribution of cosmic rays in x is asymmetric reflecting the asymmetry in the relative amount of disorder of the magnetic field, $\overline{\delta B^2}/B_0^2$. This asymmetry can be seen more clearly in Fig. 3.7 which shows the evolution of cosmic ray energy density averaged in the y -direction. (Note however that the steady state is only attained after very long times. Here, $t = 2000$ corresponds to $t\tau\tilde{K}_{\parallel}k_1^2 = 600$.) The effective perpendicular diffusivity due to the randomness of the magnetic field, $K_{\perp}^{(\text{eff})}(x)$, can be obtained from the steady-state equation

$$\frac{d}{dx} \left(K_{\perp}^{(\text{eff})}(x) \frac{de_c}{dx} \right) = -Q_c, \quad (3.17)$$

which can be integrated to obtain

$$K_{\perp}^{(\text{eff})}(x) = (x_0 - x)Q_c \left(\frac{de_c}{dx} \right)^{-1}, \quad (3.18)$$

where x_0 is the position where $de_c/dx = 0$. The resulting profile of $K_{\perp}^{(\text{eff})}$, shown in Fig. 3.8 along with

$$\chi = \frac{\overline{\delta B^2}}{B_0^2 + \frac{1}{3}\overline{\delta B^2}} = 3 \frac{\overline{B_x^2}}{\overline{B_y^2}}, \quad (3.19)$$

confirms that the effective perpendicular diffusion is controlled by the degree of randomness of the magnetic field (see, e.g., Chuvilgin & Ptuskin 1993).

3.4 Propagation in dynamo generated magnetic fields

Most studies of cosmic ray dynamics neglect the specific features of the magnetic fields produced by turbulent dynamos. We provide here a preliminary discussion of cosmic

ray evolution in a magnetic field generated by a turbulent flow of electrically conducting fluid. The magnetic field structure of these simulations is realistic enough to include important physical effects such as the enhancement of cosmic ray diffusion by turbulent fields, as mentioned in Sect. 3.3.4 and discussed in Sect. 2.6.

Magnetic field produced by the dynamo action is rather different from that prescribed as, say, a random vector field with given spectrum and Gaussian statistical properties of the components. In contrast to such *ad hoc* models, dynamo magnetic fields can be strongly intermittent (i.e., dominated by intense magnetic filaments, ribbons and sheets) and varying in time (see Brandenburg & Subramanian 2005, and references therein); both features can affect the propagation of charged particles. Moreover, since both gas flow and magnetic field are random (in space and time), any relation between cosmic ray energy density and other parameters of the medium (e.g., magnetic energy density or gas density) can only be statistical. Therefore, we expect that the energy density of cosmic rays can locally (and at any given moment) significantly exceed, say, the magnetic energy density. However, one would expect that some form of equipartition between energy densities of (or forces due to) cosmic rays and magnetic fields can be maintained *on average*. We note, however, that simulations have not fully confirmed these expectations; see also Padoan & Scalo (2005).

Our model is realistic with respect to modelling fully nonlinear dynamo action as we simulate consistently both a randomly forced flow and the magnetic field produced by it, by solving both the Navier–Stokes and induction equations (with the Lorentz force included in the former, and the velocity field obtained from the Navier–Stokes equation in the latter). The turbulent motions in our model are driven by a random force explicitly included in the Navier–Stokes equation. In reality, interstellar turbulence is driven by supernova explosions that produce strongly compressible flows with very large Mach numbers locally (some aspects of the relevant models are reviewed by Mac Low & Klessen 2004). However, we deliberately restrain ourselves from a detailed discussion of such more realistic models here (which would also include stratification, disc–halo connections, velocity shear, etc.), but instead explore just the effects of magnetic intermittency and variability. We believe that our simulations capture at least some of the most important effects of interstellar dynamo action on the cosmic ray propagation (within the limits of our model for the cosmic rays). We chose here an isothermal equation of state i.e. $\gamma_g = 1$.

The turbulence in our simulations is driven helically by a forcing function \mathbf{f} in the Navier–Stokes equation, as was done in the simulations of Brandenburg (2001), for example. At $x = \pm\pi$, we use stress-free normal field boundary conditions (Brandenburg

& Dobler 2001), and assume $e_c = 0$ on the boundaries as in Sect. 3.3.4. In the other directions we take periodic boundary conditions. Our analysis of the results presented below only uses positions that are some distance away from the domain boundaries ($L_x/8$ on both boundaries) to reduce their influence. (Including boundary points merely tends to decrease the magnitude of the correlation coefficients between the various energy densities, but it does not change the results qualitatively.)

The forcing function is given in Appendix B and its (dimensionless) amplitudes for the two simulations shown here are chosen to be $f_0 = 2$, producing an rms Mach number of about 1.2, and $f_0 = 0.05$, producing a corresponding Mach number of about 0.2. Other than the forcing amplitude, the simulations differ in that the former requires additional viscosity (see below). However, this would have no effect in the latter simulation because the Mach number is never sufficiently large to activate this viscosity.

The forcing wavenumber is chosen to be $k_f = 1.5 k_1$. This value is close to the wavenumber corresponding to the box size, $k_1 = 2\pi/L_x$, so we do not expect to have clearly distinct large-scale and small-scale magnetic fields. Generally, the flow helicity allows us to obtain dynamo action at relatively small values of the magnetic Reynolds number defined as $R_m = u_{\text{rms}}/(\eta k_f)$. However, because of the non-periodic boundaries in the x direction, and also because of the weak scale separation (k_f/k_1 is not very large), the critical value of R_m with respect to the onset of dynamo action is still around $R_{m,\text{cr}} = 30$, which is similar to what would be expected for a non-helical random flow in a periodic domain (see, e.g. Brandenburg & Subramanian 2005). The simulations presented here have $R_m \approx 150$. The kinematic growth rate of the rms magnetic field is about $0.06 u_{\text{rms}} k_f$. In Fig. 3.9 we show the evolution of the magnetic energy together with kinetic and cosmic ray energies for the simulation with $f_0 = 2$. We see that the magnetic field grows exponentially for $t \lesssim 150/(u_{\text{rms}} k_f)$ and then saturates – in agreement with earlier simulations quoted above. Fig. 3.10 is the corresponding figure for the simulation with $f_0 = 0.05$.

We note that the energy density of cosmic rays is much larger than magnetic energy density at these early times; nevertheless, the cosmic ray energy increases rather slowly after $t \gtrsim 50/(u_{\text{rms}} k_f)$. The steady-state energy density of cosmic rays is controlled by their injection rate Q_c and their diffusivity: solutions of Eq. (3.17) are proportional to $Q_c/K_{\perp}^{(\text{eff})}$. However, the effective diffusivity of cosmic rays is controlled by the degree of tangling of the magnetic field rather than by the field strength itself; see, e.g., Eq. (3.19). It is not surprising, then, that even a weak magnetic field can confine cosmic rays at early times in this model. The linear dependence of the steady-state energy density

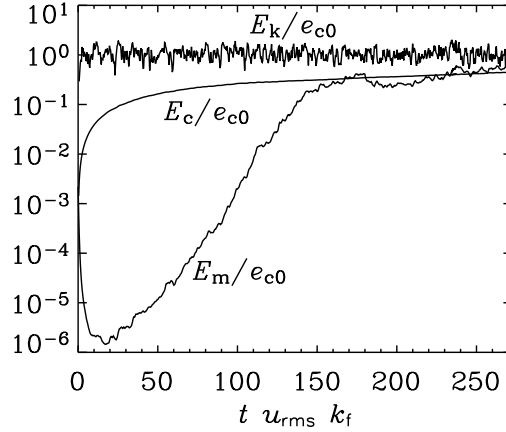


Figure 3.9: Time series of magnetic (E_m), kinetic (E_k) and cosmic ray (E_c) energies in a dynamo simulation. Here, time is given in turnover times $(u_{\text{rms}}k_f)^{-1}$, and $e_{c0} = L_x^2 \tilde{Q}_c / K_{\parallel}$ is used to normalize energies per unit volume. The thermal energy of the gas is constant with $E_g/e_{c0} \approx 0.7$.

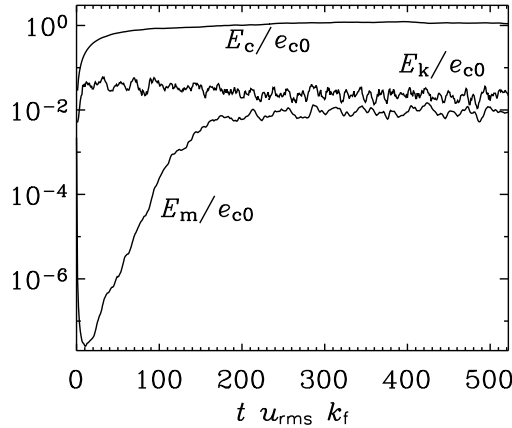


Figure 3.10: As Fig. 3.9, but with Mach=0.2

of cosmic rays on their injection rate is a direct consequence of the (almost) linear nature of the cosmic ray dynamics as described by Eq. (3.2); the only nonlinearity here is that the cosmic ray energy density affects the flow through the pressure term, and then the velocity field enters the induction equation and the advection term for the cosmic rays. However, this nonlinearity is not very strong, and our simulations confirm a linear dependence of e_c on Q_c within a broad range of the latter (at least two orders of magnitude). The magnetic field part B_0 is understood, in the present context, as an average over a scale smaller than the domain size but larger than, say, the gyroradius of cosmic ray particles.

For the simulations shown here we have chosen $Q_c = 0.01$, which yields a steady-state cosmic ray energy of $E_c \approx 1$ in units of $L_x^2 Q_c / K_{\parallel}$. The other parameters of

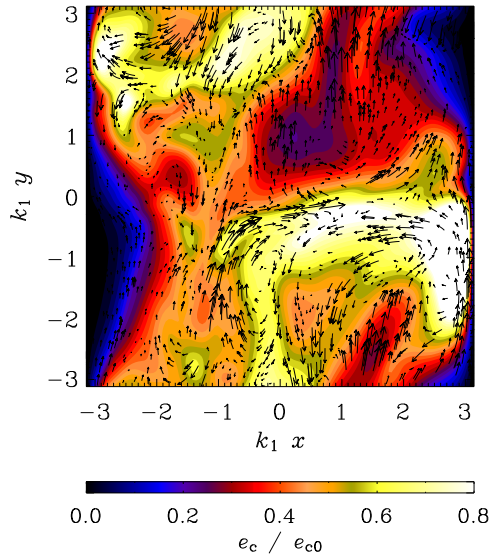


Figure 3.11: Cosmic ray energy density (colour coded, with redder colour corresponding to larger values) and magnetic field vectors in a slice taken from a dynamo simulation with $\text{Mach} = 1.2$. The magnetic field vectors are more numerous where magnetic field strength is larger. Fig. 3.12 shows a typical snapshot for $\text{Mach} = 0.2$.

the simulations presented here are $\tilde{K}_\perp = 0$, $\tilde{K}_\parallel = 0.3$, $K_{\text{Fick}} = 2 \times 10^{-2}$, $\tau = 0.3$, $\eta = 5 \times 10^{-3}$, $\nu = 0.5$. Furthermore, because the Mach number is slightly larger than unity for the $f_0 = 2$ simulation, an additional bulk viscosity proportional to the negative velocity divergence has been included. This is usually referred to as a shock viscosity; see Haugen et al. (2004) for details and the definition of a non-dimensional parameter c_{shock} which is here chosen to be 10. The value of \tilde{K}_\parallel is chosen to be close to the maximum Alfvén speed squared. The magnetic field produced by the dynamo has pronounced magnetic filaments whose half-width (radius) is about $\ell = 0.2$, which is consistent with the estimate $\ell \simeq \pi k_f^{-1} R_{\text{m,cr}}^{-1/2}$ suggested by Subramanian (1999). For $\tau = 0.3$ and $\ell = 0.2$, we have $\text{St} \approx 1$ from Eq. (3.11). The steady-state mean kinetic energy density depends directly on the intensity of the forcing. On the other hand, the ratio of magnetic to kinetic energy densities is controlled by the nature of the dynamo action. The above parameter values have been chosen as to ensure that the energy densities of magnetic field and cosmic rays are of the same order of magnitude in the statistically steady state.

In Fig. 3.11 we show a typical cross-section of the cosmic ray energy density and magnetic field vectors from the three-dimensional dynamo simulation of Fig. 3.9 at $t = 250/(u_{\text{rms}} k_f)$. The cosmic ray energy density declines toward the boundaries at $x = \pm\pi$, where the boundary condition $e_c = 0$ is imposed, and shows some moder-

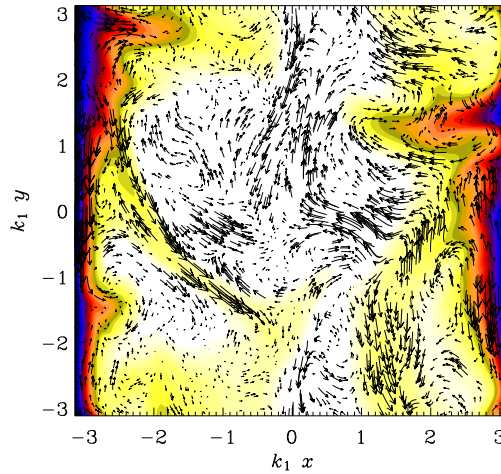


Figure 3.12: As Fig. 3.11, but for the simulation with Mach = 0.2 and at $t = 510/(u_{\text{rms}}k_f)$.

ate variation inside the domain. There is no pronounced correlation with magnetic field strength even though imprints of the field-aligned diffusion can clearly be seen, e.g., between $(x, y)k_1 = (-1, -1)$ and $(0, 0)$. For the simulation with $f_0 = 2$, we show in Fig. 3.13 a two-dimensional joint probability density function of $\log B^2$ and e_c (normalized to unit integral as usual), which demonstrates the lack of any noticeable correlation between these variables. The finite lifetime of magnetic structures produced by the dynamo must be one of the reasons of the lack of correlation between the two variables. There is some correlation between gas density and cosmic ray energy density, as shown in Fig. 3.14, but the cross-correlation coefficient is only 0.54, with the best-fitting dependence $e_c/e_{c0} \simeq \rho/\rho_0$.

In this run, if the injection rate of cosmic rays is reduced by a factor of ten to $Q_c = 10^{-3}$, the resulting steady-state mean value of the cosmic ray energy density is found to be reduced by about the same factor. The relation between cosmic ray energy density and gas density still appears to be nearly linear, but the cross-correlation coefficient is now larger, varying with time in the range 0.7–1.

In the run with Mach number of 0.2, the resulting steady-state mean energy density of cosmic rays exceeds those of magnetic field and turbulence, $E_c/e_{c0} \simeq 1$, $E_k/e_{c0} \simeq 0.02$ and $E_m/e_{c0} \simeq 0.01$. This produces significant anticorrelation between cosmic ray energy density and gas density (cross-correlation coefficient of -0.94), with a linear dependence between e_c and ρ . The joint probability plots for this run are Figs 3.15 and 3.16.

The latter anticorrelation may be attributed to the average pressure equilibrium in the domain, while a positive correlation in the supersonic flow may arise as both gas

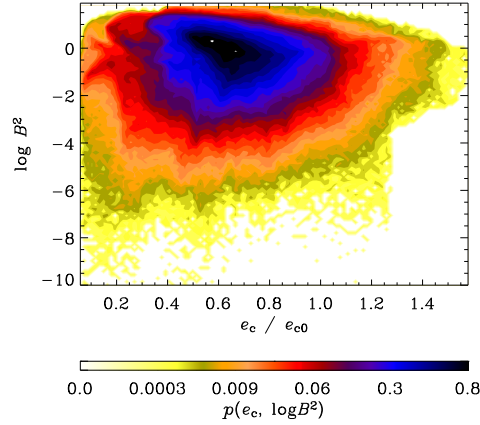


Figure 3.13: Two-dimensional histogram (or joint probability density) of magnetic pressure and cosmic ray energy density. Here, $e_{c0} = L_x^2 Q_c / K_{\parallel}$ is used to normalize e_c . The two-dimensional probability density is calculated using only points at a distance greater than $L_x/8$ from the boundaries in an attempt to avoid the regions where the distribution of e_c is affected by the boundary conditions.

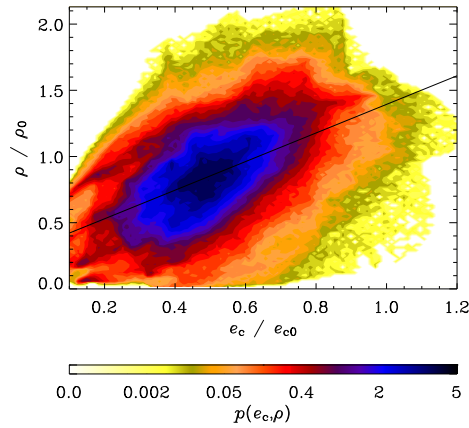


Figure 3.14: As in Fig. 3.13, but for gas density and cosmic ray energy density, showing a modest correlation between the two. The correlation coefficient is $r = 0.54$, and the straight line is a best-fitting line.

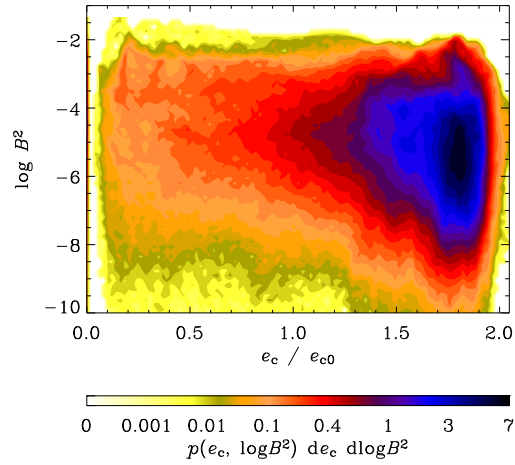


Figure 3.15: As Fig. 3.13, but for Mach =0.2

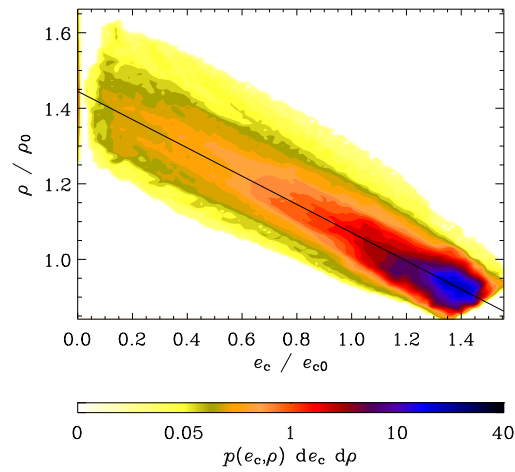


Figure 3.16: As Fig. 3.14, but for Mach =0.2

and cosmic rays are compressed by the gas flow. We have confirmed that no positive correlation between cosmic rays and gas density occurs if the cosmic ray advection is neglected.

The model illustrated in Figs 3.9 and 3.11 is close to energy equipartition between cosmic rays, magnetic field and turbulence. We note however that the Lorentz force and the cosmic ray pressure gradient have very different magnitudes because the field-aligned cosmic ray diffusivity is much larger than the magnetic diffusivity. As a result, the cosmic rays are distributed more uniformly than the magnetic field and the gas density and so the cosmic ray pressure gradient is comparatively small. For the values of the diffusivities given above, the ratio the rms cosmic ray pressure gradient, F_c , and the rms Lorentz force F_m , is typically about 0.1 of the ratio of the corresponding mean energy densities; this also applies if the Lorentz force is replaced by the gradient of kinetic energy density. The typical length scale of the magnetic field is about $\ell \simeq l_0 R_{m,cr}^{-1/2}$ and $F_m \simeq e_m/\ell$, with $l_0 \simeq 100$ pc the turbulent scale and $R_{m,cr} \approx 30$ the critical magnetic Reynolds number for the onset of dynamo action (see above). The length scale of the cosmic ray distribution can be estimated as the diffusion scale over the confinement time $\tau_c \simeq 10^7$ yr, $l_c \simeq (K_{\parallel}\tau_c)^{1/2}$. Then, for $K_{\parallel} = 10^{28}$ cm² s⁻¹,

$$\frac{F_c}{F_m} \simeq \frac{\ell}{l_c} \frac{E_c}{E_m} \simeq \frac{1}{30} \frac{E_c}{E_m}.$$

This conclusion appears to be model-independent and suggests that energy equipartition between cosmic rays and other constituents of the interstellar medium does *not* necessarily imply that cosmic rays play an important rôle in the dynamical balance.

3.5 Discussion

We have presented a preliminary analysis of cosmic ray propagation in a magnetic field produced by dynamo action of a turbulent flow. The confinement of cosmic rays resulting from their scattering by magnetohydrodynamic waves can be modelled with an equation similar to Eq. (3.2), where the advection velocity is a linear combination of gas velocity and Alfvén velocity (Skilling 1975b). Our results are based on advection with the local gas velocity. Padoan & Scalo (2005) considered local variations in cosmic ray density in the case where the advection velocity is given by the Alfvén velocity. They predict that $e_c \propto n_i^{1/2}$, with n_i the ion density. This scaling is expected if the diffusive streaming velocity, $-K_{\parallel}\nabla e_c$, and the effects of cosmic ray pressure are negligible. Our model can be adapted to test and generalize these results; the anticorrelation between

e_c and gas density in one of our models (with low Mach number) seems to be a direct consequence of pressure balance, while a positive correlation (obtained at larger Mach number) may reflect the fact that both cosmic rays and thermal gas experience similar compression by the gas flow. We have shown that our model captures naturally the dependence of the effective diffusivity of cosmic rays on the ratio of random to ordered magnetic field, $\delta B^2/B_0^2$.

The diffusivity of cosmic rays along the magnetic field is rather large; the corresponding Strouhal number, defined in Eq. (3.11) may significantly exceed unity, as shown in Eq. (3.12). For comparison, a similar estimate yields $St \simeq 1$ for the turbulent kinetic and magnetic diffusivities in the ISM. This motivates our suggestion that the standard Fickian diffusion model, which leads to the classical diffusion equation, may be a poor approximation for cosmic rays, and a more accurate description leading to some form of the telegraph equation might be more appropriate. Formally, the difference between the two approximations consists of retaining, in the latter approximation, higher-order terms in the correlation time of the random process underlying diffusion. We have introduced this effect to alleviate numerical problems, but it can be a real physical effect which deserves further careful study.

In summary, we have found that the cosmic ray distribution can be more uniform than the distributions of magnetic field and gas density. Consequently, we may argue that energy equipartition between cosmic rays and other constituents of the interstellar medium does not necessarily imply that cosmic rays play a significant rôle in the dynamical balance.

Chapter 4

Synthetic radio maps

4.1 Overview

Synthetic radio maps are a useful tool in interpreting radio observations and understanding physical the processes involved. By making comparisons of synthetic with observed data, some validation of the underlying models can be made and may help obtain estimates of some physical quantities. Many authors have attempted to make these comparisons by incorporating calculations of synchrotron emissivity into their astrophysical problems; e.g. Pariev et al. (2003) were able to make estimates of velocities in relativistic jets using observational data. Models suffer to varying degrees in how the distributions of cosmic rays is obtained in order to calculate the Stokes parameters. Examples exist where this is handled in a rather self-consistent manner, such as that of Jun & Jones (1999), where equations for electron transport were solved within a MHD simulation of a supernova remnant.

In the present context of spiral galaxies, synthetic radio maps allow us to explore how each piece of underlying physics affects the observations. As discussed in the first two chapters, assumptions about the distributions of cosmic rays and thermal electrons are often made in deriving properties of the magnetic fields from radio observations. In addition, derived information about the fields in a particular galaxy can be sensitive to the assumed distance to the galaxy and orientation with respect to the observer (i.e. the angle i of inclination between the line of sight and plane of the galactic disc). In making synthetic maps we can study the effects of making plausible variations of these quantities. In chapter 5 synthetic maps are used in making comparisons between models of barred galaxies and radio observations.

In this chapter a method for generating maps of synthetic Stokes parameters Q , U and I (and associated quantities P , RM, etc.) for spiral galaxies at the position of an observer at the Earth is discussed. In principle, these methods can be applied to objects other than galaxies; the main difference in such cases would probably be in the formulas for the Stokes parameters introduced in chapter 2. In the following I shall use ‘galaxy’ and ‘object’ synonymously.

We are most interested in how the large scale regular magnetic fields relate to polarization maps; to produce the simplest appropriate synthetic polarization maps we then need to (i) define or provide some field configuration in the galaxy (and somehow approximate other quantities), (ii) change the orientation of the galaxy so that it appears how we would like to ‘observe’ it in the sky, (iii) perform integration along an appropriate number of lines of sight, (iv) perform integration (convolution with a beam profile) over the plane of the sky.

We mention here two examples of several previous studies that employed synthetic polarization maps in a similar fashion to that described in the following sections. Otmianowska-Mazur et al. (2000) used synthetic radio maps to try and understand magnetic field structures in irregular galaxies. Soida et al. (2006) studied the interaction of galaxies with their surrounding medium. One of the main differences between the maps used in these examples and the current work is in the modelling of cosmic ray electron distributions; they took Gaussian distributions decreasing in both the radially outward direction and with perpendicular distance from the galactic midplane, whereas here we considered the cosmic rays to depend directly on modelled and observed quantities (see Sect. 4.3). Several earlier studies of polarization maps for models of spiral galaxies neglected some potentially important features included here such as Faraday rotation and variations in the distribution of cosmic ray electrons.

4.2 Stokes parameters for model galaxies

In Sect. 2.3 we state how the various physical quantities relate to the observable Stokes parameters. Here we shall summarize the form of the parameters we adopt with synthetic maps of model galaxies that can be deduced directly from the expressions in Sect. 2.3. They are not in the same units as real observer's Stokes parameters would be, but can be converted to the same units by multiplying by some dimensional constant; for comparison of the relative spatial distributions we need not worry about this. If we choose some right-handed Cartesian coordinate system with the origin at the observed galaxy's centre and the positive z -direction pointing towards an observer (i.e. perpendicular to the plane of the sky), the 'raw' Stokes parameters (Q and U) in the sky plane (x, y) at the observer's location can be written as

$$Q_{raw}(x, y) = \int_{-\infty}^{\infty} p_0 \epsilon(\mathbf{r}) \cos[2\psi(\mathbf{r})] dz, \quad (4.1)$$

$$U_{raw}(x, y) = \int_{-\infty}^{\infty} p_0 \epsilon(\mathbf{r}) \sin[2\psi(\mathbf{r})] dz, \quad (4.2)$$

where $\mathbf{r} = (x, y, z)$ and the positive x -direction points westwards in the sky. The local polarization angle ψ , including Faraday rotation is given by $\psi_0(\mathbf{r}) = (1/2) \arctan U/Q$ (in terms of the Stokes parameters) and

$$\psi(\mathbf{r}) = \psi_0(\mathbf{r}) + K \lambda^2 \int_z^{\infty} n_e(\mathbf{r}) B_{\parallel}(\mathbf{r}) dz,$$

where $K = 0.81 \text{ rad m}^{-2} \text{ cm}^3 \mu\text{G}^{-1} \text{ pc}^{-1}$, n_e is the thermal electron number density, B_{\parallel} is the line of sight magnetic field component and ψ_0 is the intrinsic polarization angle, measured anticlockwise from the positive x -direction. The number density of thermal electrons n_e can be modelled in several ways (e.g. see Sect. 5.3.3), all in some way consistent with observations.

We assume a power-law distribution of relativistic electron energies, therefore the synchrotron emissivity, ϵ , is approximately related to the other quantities like

$$\epsilon(\mathbf{r}) \propto n_{\text{cr}} B_{\perp}^{(\gamma+1)/2} \lambda^{(\gamma-1)/2}$$

where B_{\perp} is the magnitude of regular magnetic field component perpendicular to the line of sight and we have adopted n_{cr} (assuming $n_{\text{cr}} \sim N_0$ in Eq. (2.25)) as the number density of cosmic ray electrons. In the above expression, n_{cr} , B and γ can all vary with \mathbf{r} . In the examples of this thesis the synchrotron spectral index is taken to be a constant, $\alpha_s = 1$, which gives $\gamma = 3$ via Eq. (2.26). The emissivity then reduces to $\epsilon \propto n_{\text{cr}} B_{\perp}^2 \lambda$. For comparison with real observations it is sufficient set a constant of proportionality to 1 (with some dimensions), then re-scale the resulting Stokes parameters to observed values. Absolute values of the various quantities can be important, for example, if we are to include Faraday depolarization effects: then we need to know the thickness of the galactic disc, the thermal electron density and the magnetic field (at least the component parallel to the line of sight) in the correct units. Also, if we want to compare with realistically smoothed maps, then the distance to the galaxy becomes important.

The ‘smoothed’ synthetic Stokes parameters are obtained by convolving the map of raw parameters with a Gaussian beam of full width at half maximum (FWHM) d in the sky plane e.g. for Q

$$Q(x, y) = W \int_{-\infty}^{\infty} \int_{-\infty}^{\infty} Q_{\text{raw}}(x - x', y - y') \exp\left(-4 \ln 2 \frac{x'^2 + y'^2}{d^2}\right) dx' dy', \quad (4.3)$$

where $W = 4 \ln 2 / \pi d^2$. With the above Stokes parameters we can calculate maps of the polarized intensity, $P = \sqrt{Q^2 + U^2}$, the observed polarization angles, $\Psi = \frac{1}{2} \arctan(U/Q)$ and the rotation measure RM between any two wavelengths,

$$\text{RM} = \frac{\Psi_2 - \Psi_1}{\lambda_2^2 - \lambda_1^2}. \quad (4.4)$$

When comparing the angles Ψ with observations we need to adjust the synthetic angles so that they are measured from the polarization plane of the telescope.

Note that we have adopted a constant for the intrinsic degree of polarization, p_0 . Usually we do not model random magnetic fields so have no meaningful total intensity I . The appropriate expression for I_{raw} would be like that for Q_{raw} above, but with the omission of the cosine term and p_0 . The *observed* degree of polarization using I , Q and U from these expressions, $p = P/I = \sqrt{Q^2 + U^2}/I$, would (together with the assumed value of p_0) provide the degree of polarization attributable to only the regular field (which is able to depolarize the emission).

If we neglect the Faraday correction to ψ in Eqs (4.1) and (4.2) (which can usually be neglected at short wavelengths for galaxies), we often have n_{cr} as the key unknown (as discussed in Sect. 2.3). In the next section we introduce some models for this quantity which are explored in Chapter 5.

4.3 Models for cosmic ray distribution

We shall consider several models for the cosmic ray distribution in the model galaxies, all assuming a power-law distribution in the energy spectrum. For simplicity we fix the power, γ , to be constant over space. We then only need to specify the number density of cosmic ray electrons or some quantity proportional to it, since we are not usually interested in absolute units. There are no direct measurements of this quantity in external galaxies, and there are no sufficiently detailed theories that might supply it. In some of the following models we include the idea of equipartition between cosmic ray energy density and the total magnetic field strength, i.e. $n_{cr} \propto B_{tot}^2$. This can be done by including random magnetic fields from both models and simulation.

We chose to study the following empirical models for the cosmic ray number density n_{cr}

$$\begin{aligned}
 & \text{(i) } n_{cr} = \text{const}, \\
 & \text{(ii) } n_{cr} \propto \sqrt{I}, \\
 & \text{(iii) } n_{cr} \propto B^2 p^{-1}, \\
 & \text{(iv) } n_{cr} \propto B^2 + 4\pi\rho v_t^2 \kappa,
 \end{aligned} \tag{4.5}$$

where I is the observed total radio intensity and p is the percentage polarization of synchrotron emission at short wavelengths, as in Eqs (4.1) and (4.2). The first model is the simplest possible and it attributes all the variation in synchrotron intensity to that of the magnetic field and geometric factors.

In models (ii) and (iii) we make an attempt to relate n_{cr} to observable quantities.

The motivation for model (ii) is that, if cosmic rays are in equipartition with the total magnetic field, $n_{\text{cr}} \propto B_{\text{tot}}^2$, then the total intensity of synchrotron emission is roughly proportional to n_{cr}^2 . Since I is defined only in the plane of the sky, with this model we need to additionally prescribe how the distribution of n_{cr} varies along a line of sight. We take simply $n_{\text{cr}} = \text{const}$ along lines of sight. Model (iii) relies again on the idea of equipartition between cosmic rays and magnetic fields, but now we use the observed p via the expression $p \simeq p_0 B^2 / B_{\text{tot}}^2$ (Burn 1966; Sokoloff et al. 1998) to estimate n_{cr} as $n_{\text{cr}} \propto B_{\text{tot}}^2 \simeq B^2 p_0 / p$, where $p_0 \approx 0.75$ and B can be taken from our magnetic field model. This rough estimate neglects any depolarization effects and any contribution of anisotropic random magnetic fields to polarized intensity (Sokoloff et al. 1998). Obviously, it is only reasonable to use models (ii) and (iii) when comparing models to real data. Since both these models use two-dimensional maps to estimate n_{cr} in the plane of the sky, in practice we must make an assumption about the variation of n_{cr} along lines of sight. The choice $n_{\text{cr}} = \text{const}$ for each line of sight is the easiest to implement because we can incorporate n_{cr} directly into the sky frame calculation for Q and U .

For model (iv), we use the same idea as in (ii) and (iii), but now take $n_{\text{cr}} \propto B_{\text{tot}}^2 = B^2 + 4\pi\rho v_t^2 \kappa$, where ρ is gas density, v_t is a typical turbulent velocity value and κ is a constant parameterizing the relative strengths of regular and random fields. Here we assume that the random magnetic field is in equipartition with turbulent energy. This model can be used in conjunction with the dynamo model quantities in Sect. 5.3.

4.4 Generating synthetic radio maps

4.4.1 Outline

We shall force our galaxy to be contained within some finite volume to make any numerical integration calculations feasible. Usually we begin by prescribing a large-scale magnetic field in the coordinate system of the galaxy. Models for n_{cr} , n_e , etc. , can then be made in this frame of reference if desired. The coordinate system and field are rotated so that the galaxy is at the orientation at which it appears in the sky. In the frame of sky, points at which the Stokes parameters should be evaluated are chosen. At each of these points a collection of positions in the galaxy along the line of sight are defined; these are points at which quantities in Eqs (4.1) and (4.2) will be evaluated. The magnetic field and other quantities are then interpolated onto these lines of sight.

4.4.2 Dealing with different types of model

At any point in the plane of the sky a synthetic Stokes parameter is calculated by performing a numerical integration along a line of sight (to obtain a ‘raw’ quantity), then smoothing the result between corresponding values obtained for neighboring lines of sight (effectively an integration over the sky plane; see Eq. (4.3)). We shall consider two slightly different approaches in constructing the maps depending on whether the model data is given at finitely many points or defined over some continuous region of space. If, for example, the model magnetic field is output from a grid based finite difference calculation as in Sect. 5.3, then an arbitrary line of sight may not pass through any points where the field is defined. Therefore, in general we are forced to interpolate the quantities present in the integrand onto lines of sight. In this case it can be convenient to store all the values on some mesh, then re-mesh (with interpolation) onto lines of sight before performing integrations. Computationally, this is fast, but has memory constraints if too many points are used; at most we should need only slightly more points for each quantity than in the original mesh (if memory use is a problem we can choose to store only ψ_0 , ϵ , B_{\parallel} and n_e in the sky frame). If we prescribe a field in some functional form (i.e. in terms of spatial coordinates) of position in the galaxy, we need not perform any interpolation; nor do we have any constraints on memory usage. However, we need to choose enough points on the lines of sight so that the smallest scale variations in the field are captured. The advantage in this case is that there are no limitations on the size or resolution of the calculations that can be done other than computer time. The problem naturally sub-divides into calculations that can be done independently (e.g. as separate processes on multiple computers) for each line of sight; the tricky part is performing a convolution over a large number of lines of sight. We could put these onto a mesh for the lines of sight as with the simulation data, but this adds artificial constraints and limits what can be done.

Typically, one would want to define each component of a model galaxy with respect to either a cylindrical or Cartesian coordinate system, with one of the coordinate axes being the galactic rotation axis. The models presented in this thesis all have a bar feature, so it makes sense to align the major axis of the bar with the x or y -axis of a Cartesian coordinate system or with the plane $\phi = 0$ in a cylindrical system (r, ϕ, z) (where in both cases it is assumed that the bar lies perpendicular to the rotation axis). Assuming some magnetic field and other quantities have been defined with respect to such a coordinate system, the task is then to ‘observe’ the galaxy from the Earth. A simple way of doing this is to transform the coordinate system defined in the galaxy to a

Cartesian one appropriate for the observer. For example, we could take a right-handed coordinate system with the positive z -direction pointing towards the observer and the x -axis pointing westwards. Given a Cartesian coordinate system in the galaxy (possibly with quantities transformed from a cylindrical one) we can describe the transformation by rotation through three angles, as outlined in Sect. 4.4.3.

4.4.3 Rotation to the sky frame

We have already defined a coordinate system in the frame of the sky in which the Stokes parameters in Eqs (4.1) and (4.2) should be calculated; let us denote a point in this system (x_s, y_s, z_s) , with the positive z_s direction pointing towards the observer. In the following we describe how vector and scalar quantities defined with respect to some coordinate system in the galaxy can be expressed in the observer's frame. It is convenient to adopt an equivalent right handed Cartesian coordinate system (x_g, y_g, z_g) in the galaxy, with the positive z_g direction corresponding to the galactic rotation axis.

In order to understand the rotations, I shall refer to an example model of the galaxy NGC 1365, as discussed in more detail in Sect. 5.3. The initial configuration in the galactic midplane is shown in the top-left panel of Fig. 4.1 where the density distribution is shown in contours and a corresponding magnetic field projected into that plane is shown with vectors. We have a 200×200 grid where each node has an associated position vector \mathbf{x} , a magnetic field vector \mathbf{B} and a density value ρ . The panel corresponds to an area $30 \text{ kpc} \times 30 \text{ kpc}$, but has been scaled to 2×2 units for easy comparison with the other figures. The bar major axis lies on the x_g -axis. For reference, the final orientation in the plane of the sky (bottom-right figure) can be compared with either a radio map for the galaxy (Fig. 5.1), or the optical image of this galaxy (which can be seen in Fig. 5.1).

When describing the orientation of barred galaxies, we can measure several angles; (i) the angle at which the galaxy is inclined to the observer, (ii) the angle between the inclination axis and x_s -axis in the sky, (iii) the angle between the x_g -axis in the galaxy and the inclination axis. These three angles are usually in distinct planes and correspond to angles (known as Euler angles) which describe the general rotation of one Cartesian coordinate system into the other. The form z_g - x_s - z_s (z - x - z , or the so-called “ x -convention”) for Euler angles is the appropriate one to adopt in the current context. This means first a rotation about the z -axis (e.g. the galactic rotation axis), then one about the new x -axis (through the inclination angle i) and a final rotation about the z -axis (i.e. rotation in the frame of sky). In a typical model, the first rotation corresponds to rotation in the galaxy plane about the z -axis, moving the x -axis which is initially at

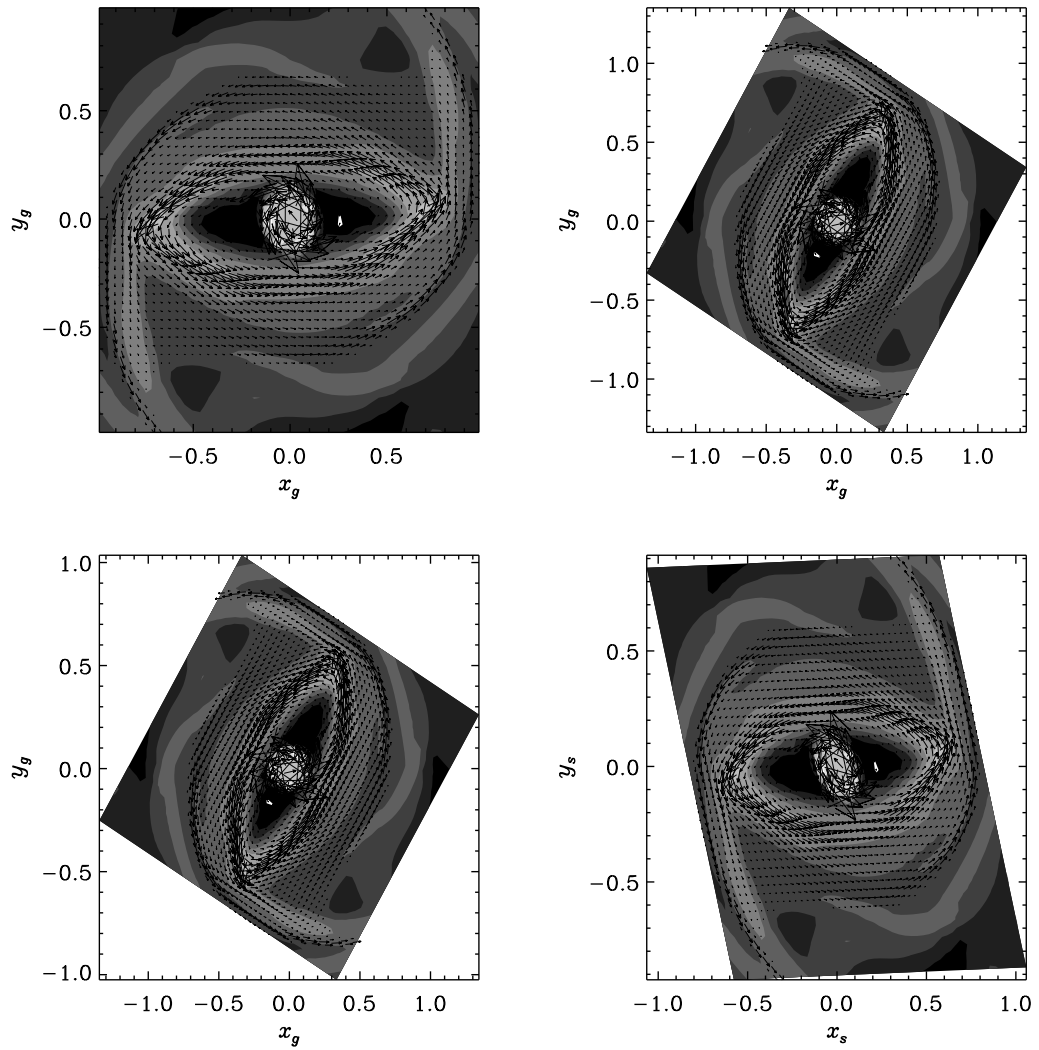


Figure 4.1: Example of rotating to the sky. scale is 1 unit to 15kpc.

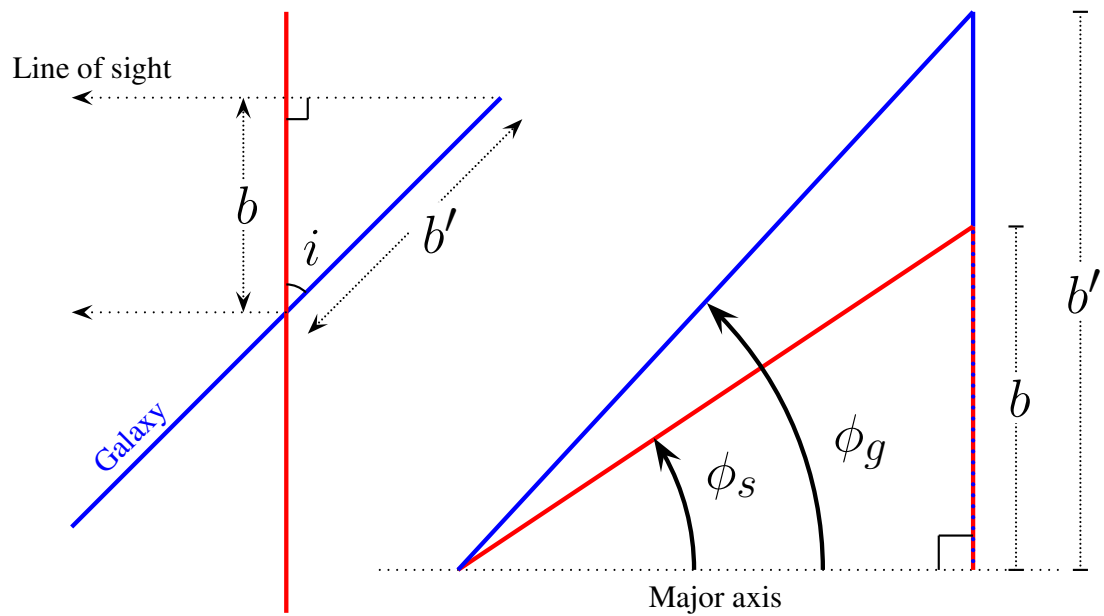


Figure 4.2: Relation between the angles i , ϕ_g and ϕ_s . In the left panel the major axis is at the intersection of the red (sky plane) and blue (galaxy plane) lines, perpendicular to the page. A measured distance b in the sky corresponds to a real distance b' in the galaxy and the two are related by $b = b' \cos i$. In the panel on the right, ϕ_s is the angle between the major axis and the projection of the bar into the sky and ϕ_g is the actual angle between the bar major axis and the major axis of the galaxy. If we denote a , the length of the base of the two triangles, $b/a = \tan \phi_s$ and $b'/a = \tan \phi_g$, then $\tan \phi_s = \cos i \tan \phi_g$.

the position of the bar, to the location of the inclination axis. We can measure angles in the plane of the sky and estimate the inclination angle i , but to obtain the first Euler angle one must calculate the difference angle between the bar and the inclination axis *in the plane of the galaxy*. The relation between the angle ϕ_s between the bar and the inclination axis in the plane of the sky and the angle ϕ_g as measured in the plane of the galaxy is given by (see Fig. 4.2)

$$\tan \phi_g \cos i = \tan \phi_s, \quad (4.6)$$

where i is the angle of inclination (this angle is usually denoted θ in an Euler angle rotation matrix).

For NGC 1365 the bar major axis is almost aligned with the x_s -axis and the inclination axis is about 130° anticlockwise from the positive x_s direction (see the bottom-right figure of Fig. 4.1), therefore $\phi_s = 130^\circ$. The angle of inclination i is about 40° so by (4.6), $\phi_g \approx 123^\circ$. This rotation can be made by applying the matrix

$$R_1 = \begin{bmatrix} \cos \phi_g & \sin \phi_g & 0 \\ -\sin \phi_g & \cos \phi_g & 0 \\ 0 & 0 & 1 \end{bmatrix} \quad (4.7)$$

to all the position vectors \mathbf{x} of the grid in the top-left figure of Fig. 4.1. The magnetic field vectors need to be expressed with respect to the new coordinate system, so we must apply R_1 to the magnetic field, so we have $\mathbf{B}' = R_1 \mathbf{B}$ and $\mathbf{x}' = R_1 \mathbf{x}$. The result is the top-right figure of Fig. 4.1 where the coordinates have been rotated 120° anticlockwise, which from our point of view rotates the galaxy clockwise through this angle. Notice the mapping of the small white mark in the central black area on the first figure; this appears in all the figures. The shaded square of density in the top-right figure of Fig. 4.1 is still 2×2 units. The remaining rotations can now be applied in the same way as this first rotation.

The next rotation is about the x -axis (or in the yz plane), which is now aligned with the major axis (or inclination axis). This turns the galaxy plane through an angle i so that in the new coordinate system the galaxy is correctly inclined. If we apply the rotation matrix

$$R_2 = \begin{bmatrix} 1 & 0 & 0 \\ 0 & \cos i & \sin i \\ 0 & -\sin i & \cos i \end{bmatrix}, \quad (4.8)$$

with $i = 40^\circ$ to the top-right figure of Fig. 4.1 ($\mathbf{x}'' = R_2 \mathbf{x}'$ and $\mathbf{B}'' = R_2 \mathbf{B}'$) we end

up with the bottom-left configuration if viewed from the xy plane. In this plane we appear to have squashed the panel in the y -direction.

The final rotation in the plane of the sky can be made using matrix

$$R_3 = \begin{bmatrix} \cos \phi_s & -\sin \phi_s & 0 \\ \sin \phi_s & \cos \phi_s & 0 \\ 0 & 0 & 1 \end{bmatrix}, \quad (4.9)$$

via $\mathbf{x}''' = R_3 \mathbf{x}''$ and $\mathbf{B}''' = R_3 \mathbf{B}''$. Since the x -axis (in the second and third panels) corresponds to the inclination axis, a rotation through $-\phi_s$ is required to put the inclination axis to the correct position in the sky. In summary, we perform $\mathbf{B}_{(\text{sky})} = R_3 R_2 R_1 \mathbf{B}_{(\text{galaxy})}$ and $\mathbf{x}_{(\text{sky})} = R_3 R_2 R_1 \mathbf{x}_{(\text{galaxy})}$. The difference between the angles as defined here and the so-called z - x - z convention for Euler angles is that the equivalent angle to ϕ_s in R_3 has the opposite sign.

4.4.4 Lines of sight

We require a finite number of points in the sky at which our Stokes parameters should be evaluated and also a finite number of points on each line of sight to perform numerical integration. Since our model galaxy is in some finite volume, by mapping the points in the galaxy to the observer's frame we can obtain bounds in the sky plane by simply taking the maximum and minimum extent of the resulting x_s and y_s coordinates. Then we can define a regular rectangular mesh with equal resolution in both the x_s and y_s directions within these bounds.

Selection of sky plane points in this manner does not guarantee that the corresponding line of sight will pass through the galaxy; it merely provides a reasonable rectangular map presentation that can be compared with observed maps; see e.g. Fig. 4.1 where the white space background in the panels corresponds to missing data.

First let us assume that model data for some galaxy is stored on a mesh aligned with the frame of the galaxy and that the rotations above have been applied at each point. At a point (x, y) in the sky, the line of sight (in the positive z -direction towards the observer) will either pass through the object at some point or miss it completely. In order to perform integration along the lines of sight, the various quantities need to be evaluated at points along that line. To choose which locations to use it is best to decide where along the z -axis the object is or if it misses it completely. One could just take minimum and maximum values along the observer's z direction by mapping all the points in the object to the sky frame, then define a set of equidistant positions

at which the integration should be performed. This can be somewhat inefficient. To demonstrate this consider a thin rectangular slab inclined at 45° to the plane of the sky which is 10 units long and 1 unit thick. The extent of a plane of the slab in the z -direction is then is about $\sqrt{50} \approx 7$. units. Take 100 equidistantly spaced points in the z -direction defined by $z_i = z_0 + idz$, with z_0 the minimum value z for the object and $dz \approx 0.07$. The width of the slab in the sky is $w = 1/\cos(\pi/4) \approx 1.4$. Since the points are equidistant, only about 20 points will pass through the slab on a given line of sight. This approach would not be so much a problem where the aspect ratio (thickness:length) of the object is close to 1. However, this is certainly not the case for many galactic disc type objects.

All examples in this text were prescribed on a regular Cartesian (or transformed to Cartesian) mesh aligned with the original coordinate system, allowing a more efficient method than the one above to be employed. Given a point (x_s, y_s) in the sky and a value of z in the original coordinate system, z_g , values of z (z_s) along the line of sight can be found via

$$z_s = \tan i (z_g \sin i - y'_s) + z_g \cos i, \quad (4.10)$$

where y'_s is the value of y obtained by de-rotating the final rotation R_3 (by replacing ϕ_s with $-\phi_s$ in R_3 and applying it to \mathbf{x}'''), i.e. $y'_s = -x_s \sin \phi_s + y_s \cos \phi_s$. The above expression is derived directly from the expression R_2 applied to $\mathbf{x}' = (x'_g, y'_g, z_g)$. Therefore, using the maximum and minimum values of z in the galaxy coordinates for z_g in the above expression, the extent of the object along a particular line of sight are obtained. Having “found” the object in the sky, appropriate integration points can now be constructed, as explained above.

4.4.5 Integration along the lines of sight

Since the points along the line of sight where the various quantities are to be evaluated will generally not coincide with a known value on the mesh, where necessary quantities are interpolated to the line of sight using trilinear interpolation. To find the mesh indices of the neighbouring points to a particular point (x_s, y_s, z_s) on the line of sight it is convenient to take the point and de-rotate it back to the point (x_g, y_g, z_g) in the galaxy coordinate system, then map the point to some integer value. The interpolation can then be performed on the \mathbf{B}''' values using simple expressions for the distances between mesh points. Using values along lines of sight, the trapezium rule is applied to numerically evaluate the integrals.

4.4.6 Implementation of beam smoothing

To incorporate the effects of the finite resolution of a telescope beam, a convolution of each of the Stokes parameters with some beam profile is made in the plane of the sky. The Stokes parameters of interest, Q and U , should by this stage have been evaluated at many points along various lines of sight. The adopted beam profile has a Gaussian of the form in Eq. (4.3). The beam smoothing is implemented in two ways: one directly calculates a double integral over the whole sky at each point in the sky; the other performs the convolution with a FFT. In the direct method, it is convenient to truncate the integration of Eq. (4.3) to 3 or 5 times the beamwidth d to save time; in such a case the normalization W is adjusted accordingly. The disadvantage with the FFT implementation is that it is limited in how many points can be used in the plane of the sky, due to limited memory. The implementation of the direct method does not have this constraint, but is (usually) much slower.

4.5 Example

Here we show an example using simple models, in which the effects of Faraday depolarization and beam smearing can be seen. In addition, we demonstrate how by calculating RM between two wavelengths we can deduce the direction of the magnetic field. We consider only a regular magnetic field. Interpolation is avoided by prescribing the field with respect to the lines of sight for our chosen orientation.

For representation purposes and simplicity we take the model galaxies to be contained within a region $-L \leq (x, y, z) \leq L$, with $L = 10$ kpc and the galactic midplane at $z = 0$. We take two magnetic field models with pointwise identical field strengths, the difference being oppositely directed field for $y < 0$. In the plane of the galaxy, the magnetic field has no z -component. The two fields can be written in cylindrical coordinates in the galaxy as

$$B_r = \begin{cases} -B_0(z) \sin(\phi/2), & 0 < \phi \leq \pi, \\ \mp B_0(z) \cos(\phi/2), & \pi < \phi \leq 2\pi, \end{cases}$$

$$B_\phi = \begin{cases} -B_0(z) \cos(\phi/2), & 0 < \phi \leq \pi, \\ \pm B_0(z) \sin(\phi/2), & \pi < \phi \leq 2\pi, \end{cases}$$

$$B_z = 0,$$

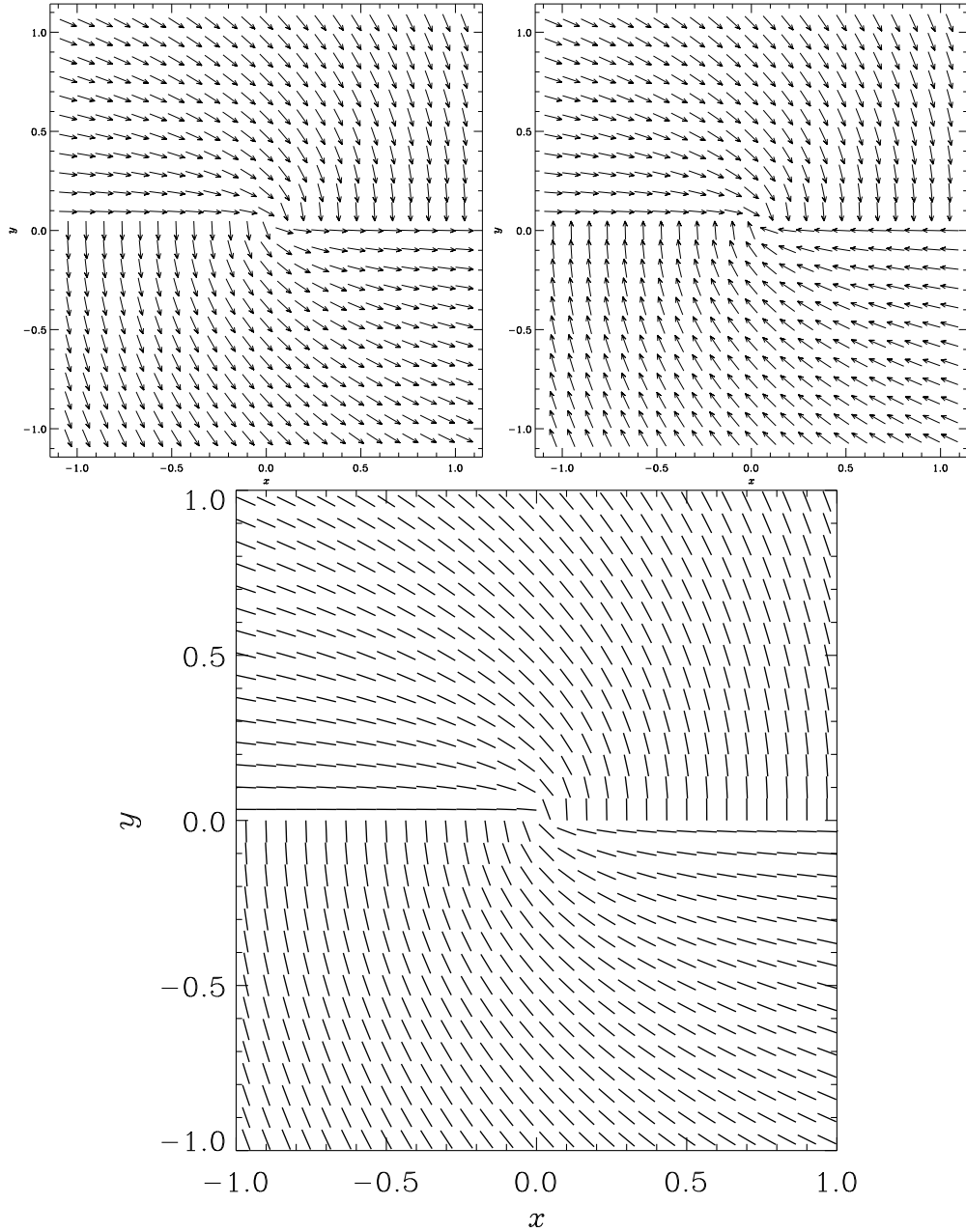


Figure 4.3: The two field configurations at $z = 0$ (top panels) and the polarization map (bottom panel) from both configurations (the map is the same for both), with the lines of sight parallel to the z axis, obtained using the given parameters.

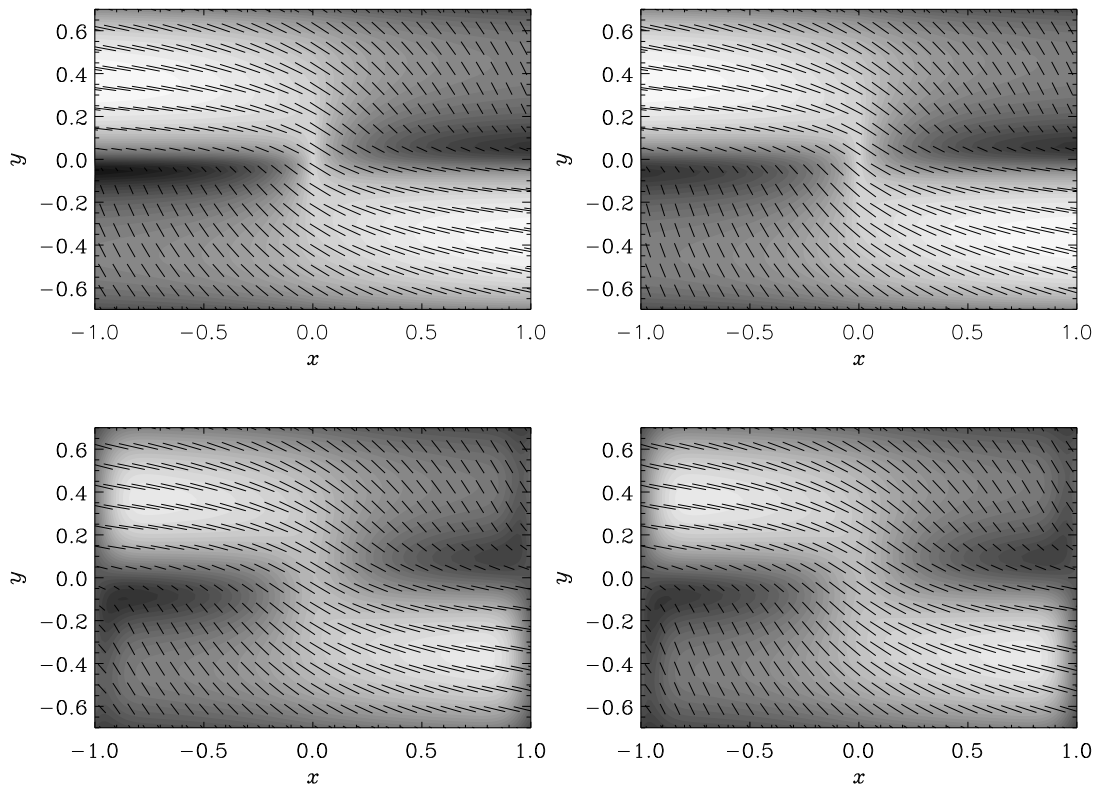


Figure 4.4: P in grey scale at $\lambda = 6.2$ cm for the two configurations inclined at 45° to the x axis. The figures on the right are for the first model and on the left for the second. The upper panels have no beam smoothing and the lower panels are smoothed to $d = 0.2$ units (1 unit represents 10 kpc). The scale runs from dark (min) to light (max).

where the \mp and \pm provide different field directions for $\phi > \pi$ (or $y < 0$) and

$$B_0(z) = A \exp(-|z|/h).$$

We take constant n_{cr} ($= 1$ arbitrary unit), $n_e = 0.01 \text{ cm}^{-3}$, $A = 5 \mu\text{G}$ and $h = 4 \text{ kpc}$. The two field configurations are shown in the top two panels of Fig. 4.3 in the $x - y$ plane for $z = 0$. The polarization map obtained when the lines of sight are parallel to the z axis is shown in the bottom panel of Fig. 4.3. P is uniform across the whole galaxy when viewed face-on like this. Since there is no z component of magnetic field, there is no Faraday rotation. The dashes represent both the observed polarization angles (in their orientation) and the polarized intensity P (in their length).

For the rest of this section we take the configurations to be inclined at 45° , by rotating about the x axis. When the configurations are inclined, the first magnetic field configuration will everywhere point towards the observer, whereas the second will point away in the bottom half (i.e. for $y < 0$). Polarization maps for the inclined field configurations are shown in Fig. 4.4, both with and without some smoothing. The maps do not have rotational symmetry about the origin. We can see this by taking two cuts in the y direction equidistant from $x = 0$. For the top left panel of Fig. 4.4, two cuts of P at $x = -0.5, 0.5$ are shown in Fig. 4.5. Notice that the minimum for the $x = -0.5$ is lower than for the one for $x = 0.5$. By removing the synthetic Faraday rotation, we obtain instead Fig. 4.6, where now the minima have the same level. Therefore, the asymmetry is caused by unequal amounts of Faraday depolarization for $x > 0$ and $x < 0$. The same set of plots for P is obtained by instead inclining at -45° . Figs 4.7 and 4.8 contain equivalent cuts for the bottom left panel of Fig. 4.4 i.e. as with Figs 4.5 and 4.6, but with smoothing.

Using the synthetic RM from each model we can determine which way the magnetic field points (on average) along the line of sight. The left panel of Fig. 4.9 shows that on the bottom right sides of the polarization maps of Fig. 4.4 (i.e. for $x, y < 0$), the measured magnitude of the RM is the same, but of opposite sign depending on the configuration. It is positive for the field towards the observer and negative for away. For $y > 0$, the cuts match. For the right panel of Fig. 4.9 with smoothing, this is not quite the same; there is no match for $y > 0$ and the RM is not equal in magnitude for $y < 0$. This means the smoothing in the region near the rapid turning of the field at $y = 0$ causes the *apparent* orientation of the field to change. To some extent the smoothing also controls the width of the minima via depolarization.

We shall see an example with similar properties to this in the next chapter.

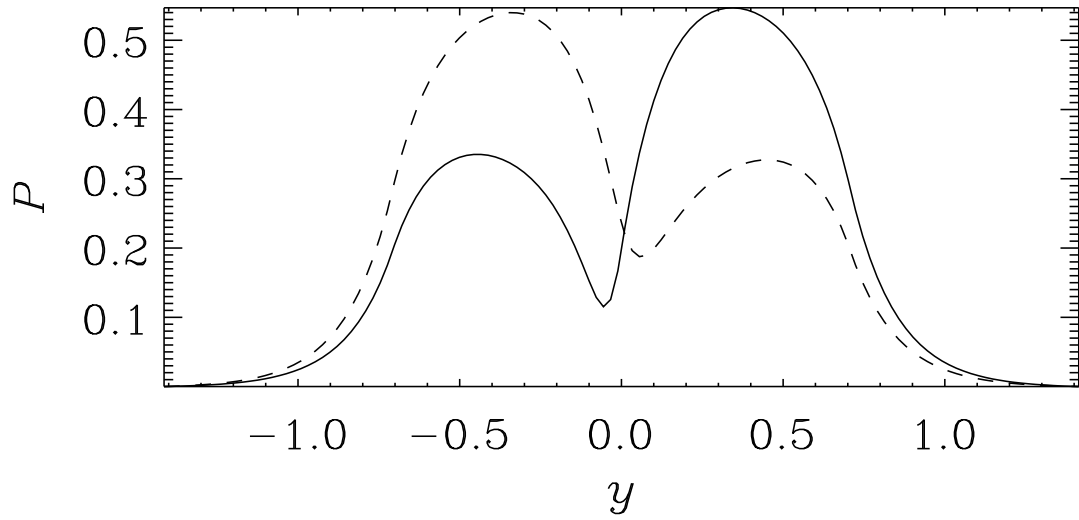


Figure 4.5: Cuts of P at $x = -0.5$ (solid) and $x = 0.5$ (dashed) for the top right panel of Fig. 4.4 .

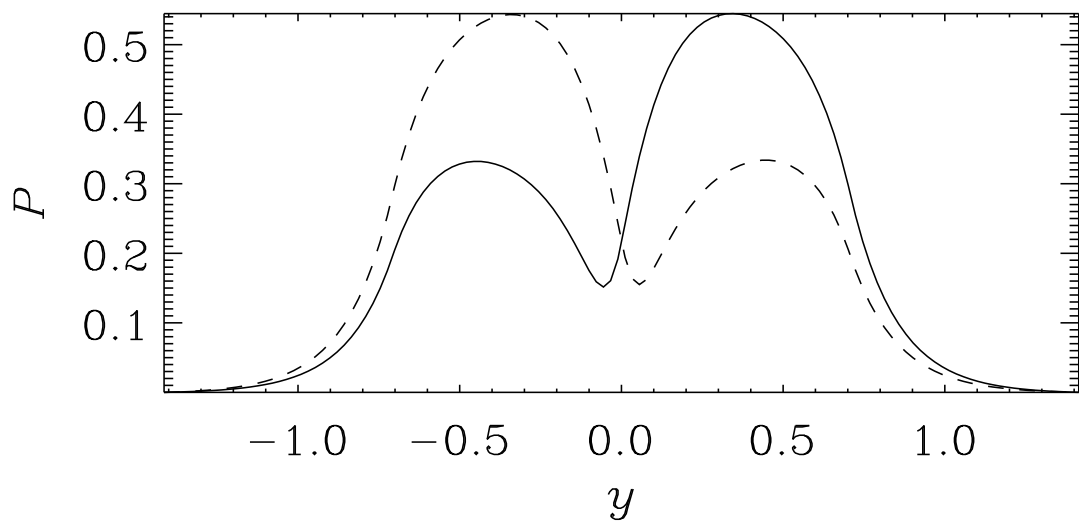


Figure 4.6: As Fig. 4.5, but without including Faraday rotation.

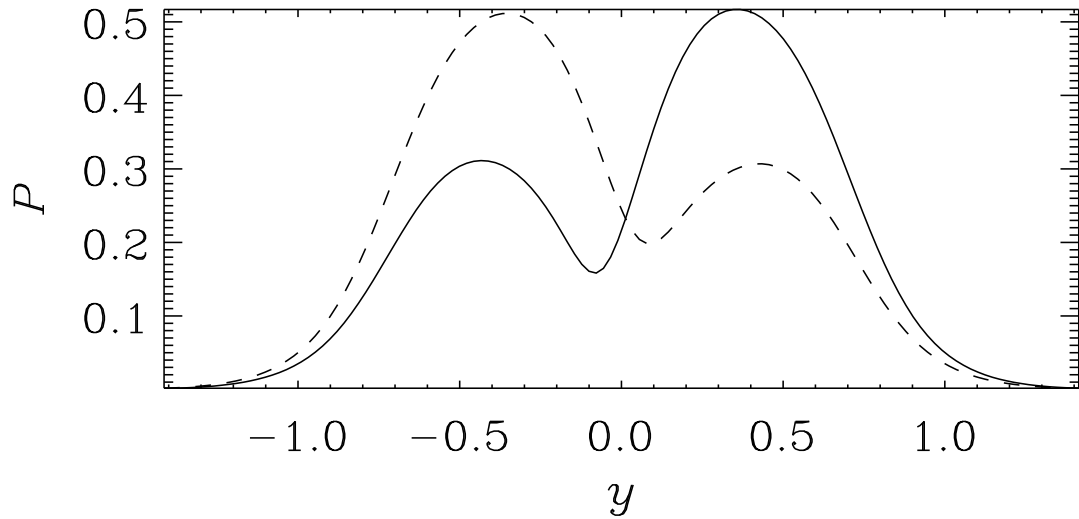


Figure 4.7: Cuts of P at $x = -0.5$ (solid) and $x = 0.5$ (dashed) for the bottom right panel of Fig. 4.4 (i.e. with smoothing).

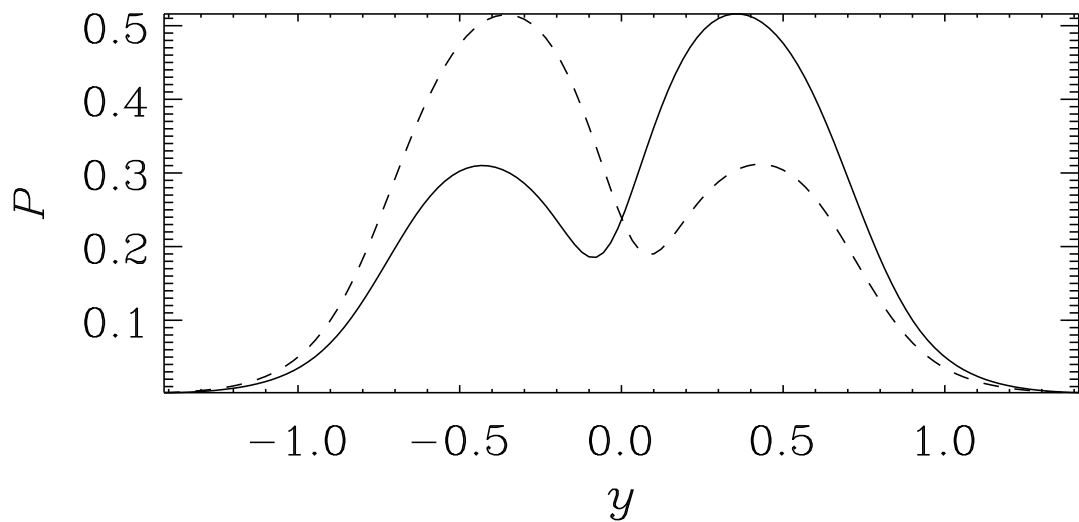


Figure 4.8: As Fig. 4.7, but without including Faraday rotation.

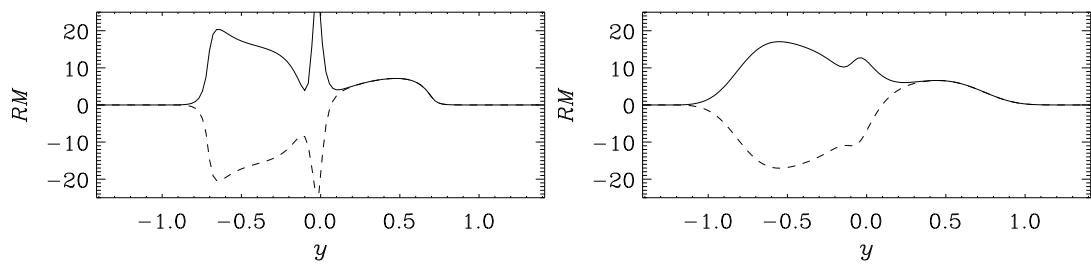


Figure 4.9: Cuts of RM for the two field configurations at $x = -0.5$. The left panel shows a cut for the first configuration (solid) and second (dashed). The right panel is as the left, but with beam smoothing applied as in Fig. 4.4.

Chapter 5

Detailed modelling of the magnetic fields in the barred galaxies NGC 1097 and NGC 1365

In this chapter, we consider models of the magnetic fields in NGC 1365. This is one of the more interesting galaxies included in a radio survey of 20 barred galaxies by Beck et al. (2002); this chapter contains some further collaborative efforts to this ongoing series of papers on magnetic fields in barred galaxies.

NGC 1365 is one of the best studied barred galaxies. It has been observed in a broad range of wavelengths, including HI (Ondrechen & van der Hulst 1989), molecular gas (Curran et al. 2001), H α (Lindblad 1999), and the radio range (Sandqvist et al. 1995; Beck et al. 2005), in addition to numerous optical and infrared observations (see Lindblad 1999 and references therein). Detailed gas dynamical modelling by Lindblad et al. (1996) provided quantitative models for the gravity and gas velocity fields in this galaxy that fit the HI and, to some extent, the CO observations. Sect. 5.1 consists of an overview of the radio observations of NGC 1365 provided by R. Beck. The gas dynamical modelling of the galaxy, detailed in Sect. 5.3.1 was performed by P. Englmaier. The dynamo modelling outlined in Sect. 5.3.2 was performed by D. Moss, with inputs from myself.

5.1 Radio observations

Observations of NGC 1365 in the total and polarized radio continuum were made with the DnC array of the Very Large Array (VLA) at 4.86 GHz ($\lambda 6.2$ cm) and 8.46 GHz ($\lambda 3.5$ cm). The full details and the maps at 15'' and 25'' angular resolution are given in Beck et al. (2005). The total radio intensity (a measure of total magnetic field strength and thermal emission) follows well the optical bar and the spiral arms. According to the observed spectral indices, the thermal fraction is about 20% at $\lambda 6.2$ cm.

The polarized emission (Fig. 5.1) is strongest in the central region and inner bar, but decreases rapidly towards the outer bar. There is also significant polarized emission between the bar and the spiral arms. No concentration in the spiral arms can be detected. At $\lambda 6.2$ cm, where the sensitivity is highest, the polarized emission forms a smooth halo around the bar. The degree of polarization is low in the bar and spiral arms, indicating that the turbulent magnetic field dominates in the regions of high gas density and strong star formation, while the regular field is strong between the bar and the spiral arms. At $\lambda 3.5$ cm, most of the extended polarized emission outside the bar is lost in the noise because of the steep synchrotron spectrum. Furthermore, the sensitivity of the VLA to extended structures is reduced for scales beyond 3 arcminutes at $\lambda 3.5$ cm, which affects the visibility of the large-scale polarized emission in NGC 1365, while at $\lambda 6.2$ cm the critical limit is 5 arcminutes and so does not affect our observations.

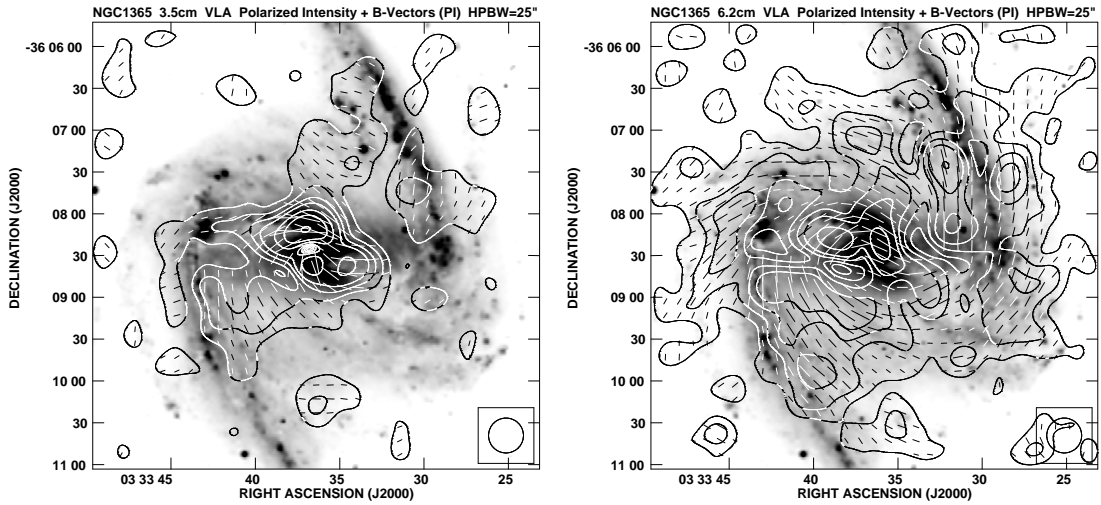


Figure 5.1: The polarized intensity contours and magnetic vectors of the polarized radio emission at the wavelengths $\lambda 3.5$ cm (left hand panel) and $\lambda 6.2$ cm (right hand panel) (both smoothed to a resolution $25''$; the beam size is shown in the lower right of each panel), superimposed onto an ESO optical image of NGC 1365, kindly provided by P. O. Lindblad. The contour levels are 1, 2, 3, 4, 6, 8, 12, ... times $30 \mu\text{Jy}/\text{beam}$ at $\lambda 3.5$ cm and $40 \mu\text{Jy}/\text{beam}$ at $\lambda 6.2$ cm; the r.m.s. noise is $15 \mu\text{Jy}/\text{beam}$ at $\lambda 3.5$ cm and $14 \mu\text{Jy}/\text{beam}$ at $\lambda 6.2$ cm.

The peak polarized intensity is 368 mJy per beam at $\lambda 3.5$ cm in the massive dust lane northeast of the centre (Beck et al. 2005). The fractional polarization is 0.8. At the same position the $\lambda 6.2$ cm map reveals a local *minimum* with polarized intensity of $150 \text{ mJy}/\text{beam}$, corresponding to a fractional polarization of only 0.2, which is near the expected contribution from instrumental polarization by the bright nuclear region. This indicates that strong depolarization occurs at $\lambda 6.2$ cm in the central region, by a factor of at least 4. In the bar and spiral arms the depolarization factor is 2–3 (Beck et al. 2005).

Polarized emission can emerge from coherent, regular magnetic fields or from anisotropic random magnetic fields; these possibilities can be distinguished with the help of Faraday rotation measures. In NGC 1097, anisotropic fields dominate in the bar region (Beck et al. 2005). However, due to the weak polarized intensity in NGC 1365, the observations available cannot provide a large-scale map of Faraday rotation, so that the relative contributions of coherent and anisotropic random magnetic fields remains unclear.

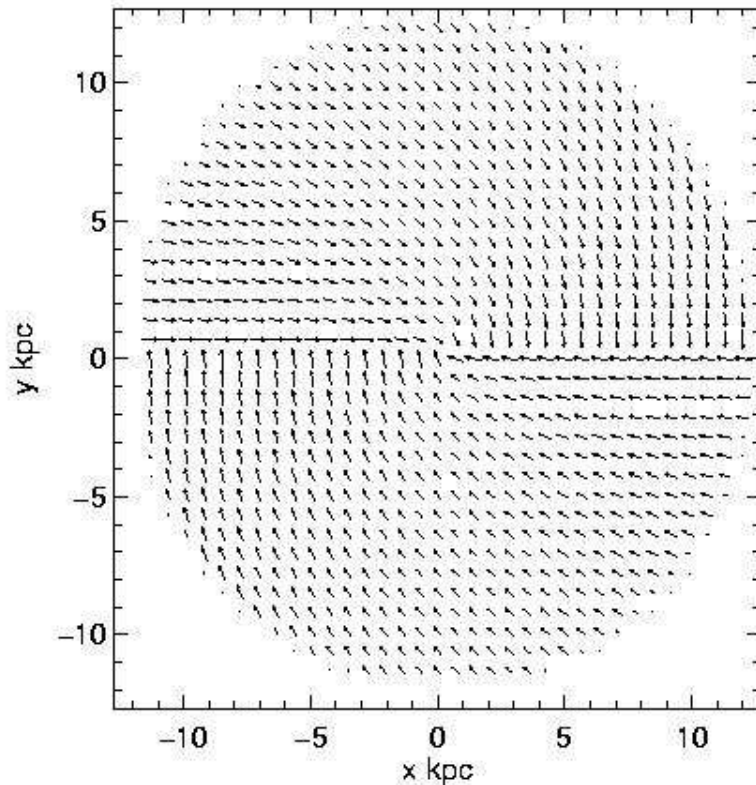


Figure 5.2: The configuration of the magnetic field used to explore the effects of geometry and beam smoothing. The model bar is located at $y = 0$.

5.2 Models of the magnetic fields in the bar region of NGC 1097 and 1365

In this section, simple models for large scale magnetic field configurations in NGC 1365 are tested by comparing synthetic radio maps with the observations of the galaxy presented in Sect. 5.1. The purpose of these models is to understand how the underlying magnetic field can give rise to a strong depolarization region (see Beck et al. 2005) which is slightly offset from the dust lanes. This feature was observed by Beck et al. (1999) and can not be explained by Faraday depolarization since it has a similar structure at both the observed wavelengths. A smooth turning in the B -vectors is observed near the bar region which suggests (when compared with hydrodynamic models) that the magnetic field lines do not follow gas streamlines.

We use synthetic polarization maps to look at the effect of inclination of the galactic disk to the observer and smoothing to finite resolution using a model of the galaxy in which the magnetic field sharply changes its direction by 90° in the bar. We consider

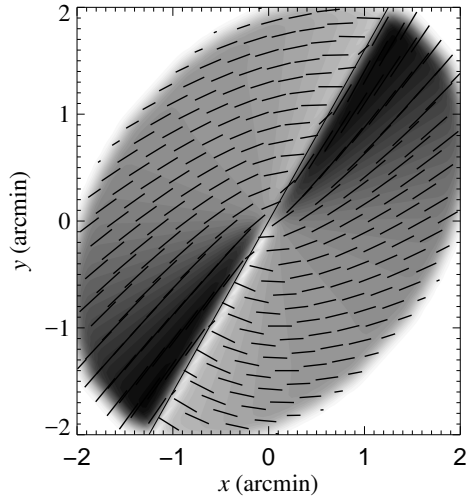


Figure 5.3: Synthetic map obtained by rotating the field shown in Fig. 5.2 with the vertical dependency given by Eq. (5.1) to the orientation of NGC 1097. The cosmic ray electron distribution is assumed to be uniform and the Stokes parameters Q and U are integrated along all lines of sight, prior to smoothing with a Gaussian beam of FWHM $10''$. The grey scale shows polarized intensity in arbitrary units (with darker shades corresponding to larger values), and the dashes represent the orientation of the polarization plane. The continuous solid line shows the bar major axis.

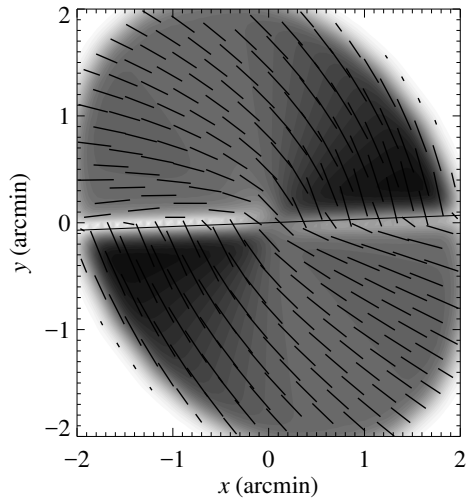


Figure 5.4: Same as Fig. 5.3, but for the inclination and major axis orientation of NGC 1365 and a Gaussian beam of FWHM $15''$.

this also as a model for the field in NGC 1097. We prescribe a magnetic field in the plane of the model galaxy in cylindrical coordinates (r, ϕ, z) , with ϕ measured in the galaxy's plane from the north-western end of the bar major axis to model NGC 1097 and NGC 1365. The positive z -direction (in the galaxy frame) points towards the observer in both cases. The mid-plane horizontal magnetic field $(\overline{B}_r, \overline{B}_\phi)$ is shown in Fig. 5.2 and is defined as:

$$\overline{B}_r = \begin{cases} -B_0(z)\phi/\pi, & 0 < \phi \leq \pi, \\ B_0(z)(1 - \phi/\pi), & \pi < \phi \leq 2\pi, \end{cases}$$

$$\overline{B}_\phi = \begin{cases} B_0(z)(\phi/\pi - 1), & 0 < \phi \leq \pi, \\ B_0(z)(\phi/\pi - 2), & \pi < \phi \leq 2\pi, \end{cases}$$

$$\overline{B}_z = 0.$$

The dependence of the modelled field on z is described by

$$B_0(z) \propto \exp(-|z|/h_B) \quad (5.1)$$

with the assumed scale height $h_B = 4$ kpc.

A z -dependent distribution of the form (5.1) is adopted for thermal electron number density n_e , with the h_B replaced with $h_e = 1$ kpc and the radial distribution truncated at $r = 12$ kpc. The number density of cosmic rays is assumed to be uniform and the synchrotron spectral index is assumed to be $\alpha_s = 1$. After rotating the major axis position angle and inclining the galaxy to the line of sight by the same angles as observed in the galaxies NGC 1097 and NGC 1365, we calculate the Stokes parameters Q and U (as Q_{raw} , U_{raw} of Sect. 4.2) along lines of sight between points corresponding to $z = \pm 2h_B$ in the galaxy coordinate system. We convolve the result with a Gaussian of FWHM $10''$ and $15''$ in the plane of the sky for NGC 1097 and NGC 1365, respectively. Depolarization due to both differential Faraday rotation along the line of sight and beam smearing occurs. Figures 5.3 and 5.4 show the obtained synthetic polarized intensity in grey scale with apparent polarization B -vectors superimposed. Not surprisingly, the abrupt turn of magnetic field by 90° results in strips of small polarized intensity, similar to the depolarization valleys observed in NGC 1097 (Beck et al. 1999) and NGC 1365.

The combination of inclination and smoothing to the beam resolution leads to valleys in P parallel to the bar's major axis which are offset by $15''$ from the ridge of maximum P , consistent with the observations. The width of the valleys of one Gaussian FWHM is also consistent with the observations. Because of the inclination

of the galaxies, the two valleys in each model are not equally deep, but the difference is unimportant compared with the intrinsic asymmetries found in the observations. The B -vectors turn by about 90° in front of the bar, much more sharply than in the observations, especially in NGC 1365. This implies that the turn of magnetic field near the depolarization valley in real galaxies is smoother than that in this model, and so it is *partially* resolved in our observations.

We conclude that the effects of disc inclination and beam smoothing can explain the observed offset of the “depolarization valleys” from the ridges, but the observed turning of the B -vectors is much smoother than that predicted from our simple model; we have tried varying the magnetic field models in the mid-plane so that the turning of the vectors is smoother, but the resulting depolarization is reduced and apparently becomes inconsistent with what is observed.

5.3 Global models of NGC 1365

Here we present models of the global magnetic field in NGC 1365 based on mean-field dynamo theory and the large-scale velocity field of interstellar gas fitted to HI and CO observations of this galaxy by Lindblad et al. (1996). We make fairly stringent direct comparison with the radio observations of Sect. 5.1 by producing synthetic polarization maps. This allows both the dynamo and gas dynamical models to be tested against independent radio data, which have not been used in the the model construction.

The magnetic field modelling made here is quite similar to that of a previous study of NGC 1097 (Moss et al. 2001), the main difference being that we use a gas dynamical models specific to NGC 1365, whereas generic models were applied to NGC 1097. Another difference is that the dynamo model here is fully three dimensional, rather than using the ‘no- z ’ approximation (Subramanian & Mestel 1993) to remove the explicit dependence on the vertical coordinate.

There are some similarities with the work in this section to other earlier models of magnetic field generation in barred galaxies, such as that of Otmianowska-Mazur et al. (2002). In that study, stick particle methods were used to generate three dimensional velocity fields for generic barred galaxies, which were then used in dynamo calculations. They found that magnetic field arms were obtained offset from the gas arms, similar to what we find here.

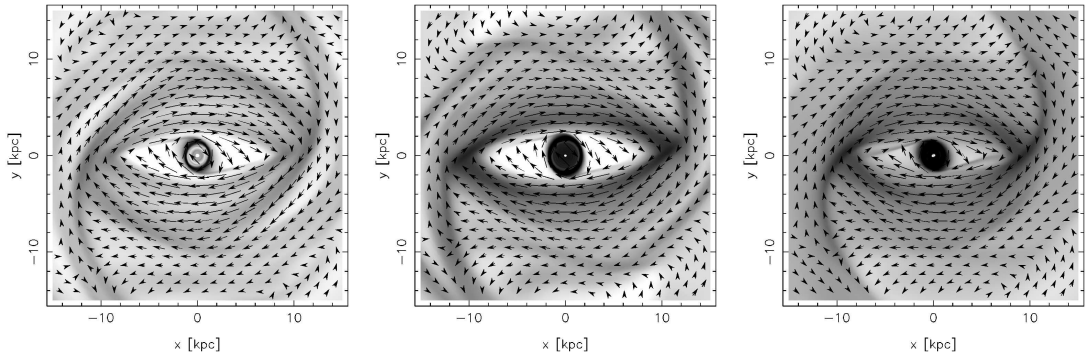


Figure 5.5: The model gas density with superimposed velocity vectors in the reference frame corotating with the bar, in gas dynamical models based on **(a)** the rotation curve of the LLA model with $c_s = 10 \text{ km s}^{-1}$ (left hand panel), and the rotation curve of Sofue et al. (1999) with **(b)** $c_s = 10 \text{ km s}^{-1}$ (middle panel) and **(c)** $c_s = 30 \text{ km s}^{-1}$ (right hand panel), with c_s the sound speed. Shades of grey represent the logarithm of gas density (darker shades corresponding to larger values), with each shade corresponding to the same density in each panel. Note the smaller density contrast in the bar region in the model with higher speed of sound (panel c).

5.3.1 The gas dynamical models

These models are based on the gas dynamical model of Lindblad, Lindblad, & Athanassoula (1996). Their gravitational potential (labelled ‘BSM’ in the original paper, kindly provided by P. O. Lindblad; denoted LLA in this chapter) includes gravitational potentials of the disc and spiral arms and was derived from the nonaxisymmetric part of the deprojected J -band image. Their best fit parameters are $A_{\text{bar}} = 1.2$ and $A_{\text{spiral}} = 0.3$ for the relative contributions of the bar and spiral arms. The model rotation curve fits the HI rotation curve for galactocentric distances $r > 120''$ ($\approx 11 \text{ kpc}$) and gives reasonable resonance locations inside this radius. Various versions of the LLA model used the bar angular velocity of $\Omega_p = 18 \text{ km s}^{-1} \text{ kpc}^{-1}$ (model BSM) and $17 \text{ km s}^{-1} \text{ kpc}^{-1}$ (model BSM2), with the corotation radius close to 14 kpc in both cases.

The full gravitational potential of the LLA model is obtained from two independent observations: (i) the HI rotation curve, used to fix the total radial mass distribution of the galaxy including dark matter, and (ii) the J -band data, tracing the stellar mass distribution, which is only used to derive (after deprojection) the amplitude of nonaxisymmetric perturbations in the disc plane. The latter cannot be used to derive the rotation curve reliably because of the presence of dark matter, and the former also can be misleading when the gas flow is significantly nonaxisymmetric.

Lindblad et al. adopted 20 Mpc ($1'' = 97 \text{ pc}$) as the distance to NGC 1365, but

here the adjusted the model is based on a distance of 18.6 Mpc ($1'' = 90$ pc), which is the distance obtained by Madore et al. (1998).

Calculating two-dimensional isothermal gas dynamical models with the code ZEUS 2D (Stone & Norman 1992), a close match to the model of Lindblad et al. (1996) was found. The warp in the outer disc was neglected as the region of interest is the inner one. The basic models, shown in Fig. 5.5b,c have the bar angular velocity $\Omega_p = 16.16 \text{ km s}^{-1} \text{ kpc}^{-1}$ and the corotation radius at $R_c = 15.5 \text{ kpc}$; a model with $\Omega_p = 17 \text{ km s}^{-1} \text{ kpc}^{-1}$ and $R_c = 16.3 \text{ kpc}$ was also considered (Fig. 5.5a). The angular velocity of the spiral pattern is taken to be equal to that of the bar. For reasons explained below in Section 5.3.3, the resulting gas density in the bar region was too low to reproduce the observed magnetic field within the dynamo model. The gas density in the LLA model can be argued to be underestimated inside the corotation radius because the rotation curve used had poor resolution, and underestimates the depth of the potential well. We derived our basic model from the LLA model by replacing the rotation curve used by Lindblad et al. (1996) with the more recent CO rotation curve of Sofue et al. (1999). This modified model was much better able to reproduce the observed magnetic field, while remaining in agreement with the overall morphology of the molecular gas distribution. A significant difference is that there is more material in the central regions when Sofue's rotation curve (Sofue et al. 1999) is used. The rotation curve used here is shown in Fig. 5.6a, with the positions of resonances illustrated in Fig. 5.6b.

We also studied the dependence of the gas dynamics and magnetic field on the sound speed adopted in the isothermal gas model. This parameter is uncertain in our models for several reasons. Englmaier & Gerhard (1997) showed that the large-scale gas distribution in isothermal gas flow models of barred galaxies can depend on the sound speed, even if the pressure forces are negligible. Since the position, and even existence, of shocks depends on Mach number, the global gas flow configuration can change as a result of a relatively small change in the speed of sound. Different parts of the multi-phase interstellar medium (ISM) may not follow the same global gas flow. Different numerical methods have been shown to represent different aspects of the ISM with varying success. Sticky particle methods, for example, model better the clumpy ISM, while grid-based methods give a better description of the shocks and the smooth gas component.

The global magnetic field depends on the gas flow via Eqs (5.2) and (5.3); however, it is not *a priori* clear which component of the ISM carries the magnetic field and, therefore, what is the appropriate sound speed of the gas. We have considered models

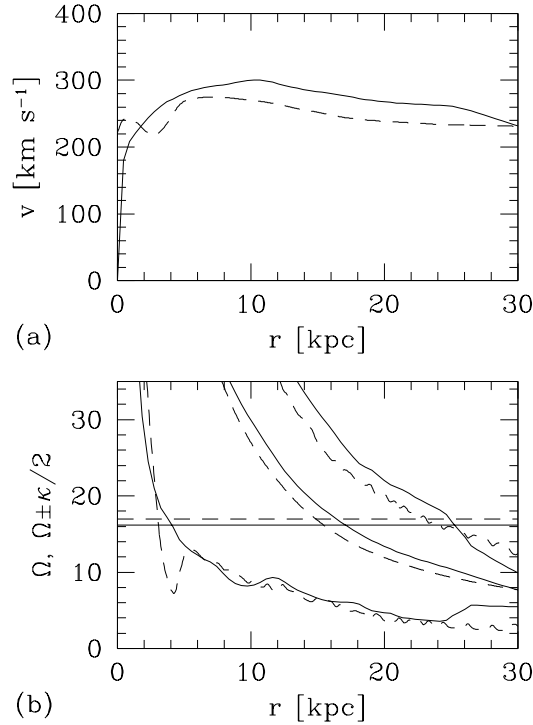


Figure 5.6: **(a)**: The rotation curves used in the gas dynamical modelling: that from Lindblad et al. (1996) (solid; as in Fig. 5.5(a)), and one more consistent with more recent CO observations (Sofue et al. 1999) (dashed; as in Fig. 5.5(b),(c)). The plot assumes the distance of NGC 1365 to be 20 Mpc as in Lindblad et al. (1996). The radius of corotation is $R_c \approx 14 \text{ kpc}$. **(b)**: The linear resonance diagram for the rotation curves shown in (a) with the same line style. From bottom to top: $\Omega - \kappa/2$, Ω , and $\Omega + \kappa/2$ in units of $\text{km s}^{-1} \text{kpc}^{-1}$. The resonances are located at the intersections with the horizontal lines corresponding to $\Omega_p = 16.16 \text{ km s}^{-1} \text{kpc}^{-1}$ (solid) and $17 \text{ km s}^{-1} \text{kpc}^{-1}$ (dashed). The small scale structure in the $\Omega \pm \kappa/2$ curves is an artefact of plotting.

with the speed of sound equal to 10 and 30 km s^{-1} (see Sect. 5.3.9).

As well as the velocity field, our magnetic field model also relies on the gas density obtained from gas dynamical simulations; this is discussed in Sect. 5.3.2 – see Eq. (5.5).

5.3.2 The dynamo models

Our model can be regarded as a development of the dynamo model of Moss et al. (2001), used to model the large-scale magnetic field in a generic barred galaxy. For barred galaxies, shear in the large-scale velocity provides the dominant induction effect. As a consequence, we are able to demonstrate that the gross features of the model galactic magnetic field are rather insensitive to the (poorly known) details of the dynamo system (in particular, the α -coefficient). Therefore, we can plausibly constrain the freedom

Table 5.1: Parameters of models discussed in the text, as defined in Sect. 5.3.2. In all the models, the angular speed of the bar is $\Omega_p = 16.16 \text{ km s}^{-1} \text{ kpc}^{-1}$ with the corotation radius at 15.5 kpc .

Model	R_α	η_0 [$10^{26} \text{ cm}^2 \text{ s}^{-1}$]	q_η	r_η [kpc]	f_η	c_s [km s^{-1}]
1	3.0	1.0	3	3.0	0	10
2	3.0	1.0	3	1.5	2	10
3	0.0	1.0	3	1.5	2	10
4	2.7	2.5	3	1.5	2	10
5	3.0	2.0	3	1.5	2	10
6	3.0	1.0	3	1.5	2	30

within the dynamo models, and so draw conclusions about the interstellar medium in barred galaxies.

We here introduce further developments required to reproduce the basic features of the global magnetic pattern in NGC 1365. We solve the standard mean field dynamo equation for the large-scale (regular) magnetic field \mathbf{B}

$$\frac{\partial \mathbf{B}}{\partial t} = \nabla \times (\mathbf{u} \times \mathbf{B} + \alpha \mathbf{B} - \frac{1}{2} \nabla \eta \times \mathbf{B} - \eta \nabla \times \mathbf{B}), \quad (5.2)$$

in three spatial dimensions, using Cartesian coordinates (x, y, z) , where x and y are horizontal dimensions, and the disc midplane is at $z = 0$. Here α and η are the turbulent transport coefficients responsible for the α -effect and turbulent magnetic diffusion, respectively, \mathbf{u} is the large-scale velocity field, and the term with $\nabla \eta$ allows for the turbulent diamagnetism associated with the spatial variation of the turbulent diffusivity (Roberts & Soward 1975). In our standard case, our computational domain covers the region $-L \leq (x, y) \leq L$, $0 \leq z \leq aL = z_{\max}$, where a is the domain's aspect ratio. We take a mesh of size $n_x \times n_y \times n_z$, with uniform spacing in the horizontal directions and also, separately, vertically. The maximum resolution readily available to us was $n_x = n_y = 200$, $n_z = 31$, and in order to resolve satisfactorily the solutions we took $L = 15 \text{ kpc}$ and $a = 0.12$, so $z_{\max} = 1.8 \text{ kpc}$. (Thus we study only the inner part of this unusually large barred galaxy.) The total thickness of the gas layer that hosts the large-scale magnetic field is taken as $2h = 0.9 \text{ kpc}$, compatible with the thickness of the diffuse warm gas in the Milky Way. Our procedure is to time-step the x and y components of Eq. (5.2), and then to use the condition $\nabla \cdot \mathbf{B} = 0$ to update B_z . We restrict ourselves to solutions of even (quadrupolar) parity with respect to the disc plane $z = 0$, and so the latter step is straightforward, given that $B_z = 0$ at $z = 0$. This

is the same procedure used in the three-dimensional galactic dynamo models described in Moss (1997), except that cylindrical polar coordinates were used there.

In Eq. (5.2), α parameterizes the dynamo action of the interstellar turbulence, and η is the turbulent magnetic diffusivity. We assume both of these quantities to be scalars (rather than tensors) and, in order to obtain a steady state with saturated dynamo action, introduce a simple α -quenching nonlinearity into the problem, writing

$$\alpha = \frac{\alpha_0}{1 + \xi B^2/B_{\text{eq}}^2}, \quad B_{\text{eq}}^2 = 4\pi\rho(\mathbf{r})v_t^2, \quad (5.3)$$

$$\alpha_0 = \alpha_* \frac{\Omega(r)}{\Omega_0} f(z), \quad (5.4)$$

with

$$f(z) = \begin{cases} \sin(\pi z/h), & |z| \leq h/2, \\ [\cosh(2|z|/h - 1)]^{-1} \operatorname{sgn} z, & |z| > h/2. \end{cases}$$

Here Ω_0 is a typical value of Ω , B_{eq} is the magnetic field strength corresponding to equipartition between magnetic and turbulent kinetic energies, and α_* is a constant, which we can adjust. Quite arbitrarily, we adopt $\Omega_0 = \Omega$ at $r = 3 \text{ kpc}$, and Eq. (5.4) shows that α_* is the maximum value of α at this radius. Thus we are assuming that the large-scale magnetic field significantly reduces the α -effect when its energy density approaches that of the turbulence; the constant ξ is introduced to suggest formally some of the uncertainty about the details of this feedback. The dependence of α on height, defined by $f(z)$, is implicitly odd with respect to the midplane, with $|\alpha|$ increasing with $|z|$ from 0 at $z = 0$ to a maximum at $|z| = h/2$, and then decreasing to zero as $|z| \rightarrow \infty$ (remembering that we only explicitly model the region $z \geq 0$). Because of the symmetry of the dynamo model, if \mathbf{B} is a solution, then $-\mathbf{B}$ is also a solution.

We take $\xi = O(1)$, assuming that there is no catastrophic α -quenching (e.g. Brandenburg & Subramanian 2005). The models were computed with $\xi = 1$, and the field strength then scales as $\xi^{-1/2}$. The turbulent speed that enters B_{eq} is taken to be equal to the speed of sound as adopted in the gas dynamical model. The gas density $\rho(x, y, 0)$ is taken from the gas dynamical model described in Sect. 5.3.1. We extend this away from $z = 0$ by writing

$$\rho(x, y, z) = \frac{\rho(x, y, 0)}{\cosh(|z|/h)}. \quad (5.5)$$

The magnitude of the gas density is relatively unimportant in our dynamo model (where the Lorentz force is not included into the Navier–Stokes equation) as it affects only the magnitude of the magnetic field in the steady state, via Eq. (5.3), but not its spatial

distribution. The only aspect where the magnitude of gas density plays a rôle is the Faraday depolarization and, hence, the modelled distribution of polarized intensity; see Sect. 5.3.3. This effect is, however, relatively weak at $\lambda = 3\text{--}6$ cm and it is plausible that other depolarization effects (e.g., Faraday dispersion) are more important in the real galaxy. The gas density in our model is shown in Fig. 5.8.

The gas velocity in the plane $z = 0$, $\mathbf{u}(x, y, 0)$, is also taken from the gas dynamical model. For convenience, we split this into rotational and non-circular parts,

$$\mathbf{u}(x, y, 0) = \Omega(r)r\hat{\phi} + \mathbf{v}(x, y, 0), \quad (5.6)$$

respectively, where $r = (x^2 + y^2)^{1/2}$ is axial distance.

We then introduced two significant modifications. We found that, in the gas dynamical model, $\Omega(r)$ increases very rapidly towards the rotation axis (very approximately, as $1/r$). The gas dynamical model appears to handle this feature satisfactorily, but it causes significant numerical problems for the dynamo code at attainable numerical resolution. Thus Ω was softened by introducing an explicit parabolic profile within a radius of 2.1 kpc, with the maximum of Ω truncated to $110 \text{ km s}^{-1} \text{ kpc}^{-1}$ (as compared to $1730 \text{ km s}^{-1} \text{ kpc}^{-1}$ at $r = 0.013 \text{ kpc}$, the smallest distance from the axis in the gas dynamical model used). This modification can be expected to reduce the magnetic field strength in regions close to the galactic centre, but as this region is not well resolved by the radio observations, we cannot in any case make a comparison between these and the computed magnetic field. Further, we continued the velocity field above the disc by introducing z -dependence into the horizontal velocity components via

$$\mathbf{u}(x, y, z) = \frac{\mathbf{u}(x, y, 0)}{\cosh(|z|/1.2 \text{ kpc})}, \quad (5.7)$$

and $u_z = 0$ everywhere.

In order to model a galaxy surrounded by near-vacuum, we allow the magnetic diffusivity to become large high in the halo (Sokoloff & Shukurov 1990),

$$\eta = \eta_0 \begin{cases} 1, & |z| \leq h, \\ 1 + (\eta_1 - 1) \left[1 - \exp\left(-\frac{|z| - h}{1.5 \text{ kpc}}\right) \right]^2, & |z| > h, \end{cases}$$

where η_0 and η_1 are constants; thus $\eta = \eta_0$ near the disc midplane and $\eta \rightarrow \eta_0\eta_1$ in the halo region ($|z| > h$). We adopted a nominal $\eta_1 = 2$ – larger values led to numerical difficulties. A conventional value of η_0 is $10^{26} \text{ cm}^2 \text{ s}^{-1}$; however, we also

considered models with values larger than that – see Table 5.1. In order to reproduce polarized radio maps of NGC 1365 in sufficient detail, we had to introduce further spatial variation in η . Following Moss et al. (2001), we have assumed that the turbulent diffusivity is enhanced by the shear of the nonaxisymmetric velocity according to

$$\eta_0 \propto \left(1 + f_\eta \frac{S}{S_{\max}} \right), \quad S = \left| \frac{\partial u_x}{\partial y} \right| + \left| \frac{\partial u_y}{\partial x} \right|,$$

where S_{\max} is the maximum value of S . The effect of $f_\eta \neq 0$ is, firstly, to broaden magnetic structures near the spiral arms, and, secondly, to reduce the central peak of magnetic field. The values of f_η adopted are shown in Table 5.1. We did not consider a similar enhancement in α as Moss et al. (2001) found it to be unimportant. The values of f_η that were sufficient to produce realistic magnetic fields in spiral arm were still too small to reduce the central maximum of magnetic field to an acceptable level. Therefore, we introduced an additional enhancement of η in the central part of the galaxy, multiplying η_0 by $q_\eta \exp(-r^2/2r_\eta^2)$; the values of q_η and r_η are given in Table 5.1 for each model studied.

Clearly, we have made a number of rather arbitrary choices, in particular when extending the two dimensional gas dynamical model into three dimensions. Our overall impression, from a substantial number of numerical experiments, is that the overall nature of our results does not depend very strongly on these choices.

At $z = z_{\max}$, and on $x, y = \pm L$, the boundary conditions are $B_x = B_y = 0$. On $z = 0$, $\partial B_x / \partial z = \partial B_y / \partial z = 0$, $B_z = 0$, and so the integration of $\nabla \cdot \mathbf{B} = 0$ gives the values of B_z on the other boundaries. These are conservative boundary conditions on B_x and B_y , in that they will increase the field gradients and thus raise the threshold for dynamo action to occur.

We nondimensionalize the problem in terms of the length $L = 15 \text{ kpc}$, time h^2/η_0 and magnetic field B_{eq} . Given that the velocity field, including the angular velocity, is given by the dynamical model, the only free dynamo parameter is α_* ; the corresponding dimensionless parameter is

$$R_\alpha = \frac{\alpha_* h}{\eta_0}, \quad (5.8)$$

where α_* is defined in Eq. (5.4). The dynamo action prevents magnetic field from decay for values of R_α exceeding about 1 for $\eta_0 = 10^{26} \text{ cm}^2 \text{ s}^{-1}$; the critical value of R_α increases roughly proportionally to η_0 .

Henceforth, we will use dimensionless variables, unless explicitly otherwise stated; with the assumed density profile of Eq. (5.5), the units of gas number density and magnetic field strength are 44 cm^{-3} and $30 \mu\text{G}$, respectively.

5.3.3 Results

In previous efforts, comparisons of radio observations with model magnetic fields for spiral galaxies has been made using either the modelled B^2 or synthetic observables. Comparison of cuts or radial/azimuthal profiles have been relatively successful (e.g. Moss et al. 2001). However, most of these models attempted to compare only generic features with those found in observations, rather than compare directly a model for a particular galaxy, as we do here. In this modelling, we initially employed radial and azimuthal profiles of polarized intensity, derived from several dynamo and gas dynamical models together with a range of models for synthetic radio emission intensity. In terms of azimuthally averaged radial profiles, by arbitrarily rescaling the model polarized intensity we were able to fit some models to the the observed profiles, but only in either the inner part of the galaxy (say roughly $r < 0.8r_c$), or the outer regions. Some of these models are shown in Fig. 5.7, where the points with error bars are the observed polarized intensity. This prompted refinement of the comparison techniques as detailed below. Suitable gas dynamical and dynamo models were then able to be identified and their properties refined. Attention to *where* the model data and the observed data should be expected to coincide (based on both what features are incorporated into the models and where the observed data is unsatisfactory to make meaningful comparison) was a key consideration in this effort. In the following we describe a range of models exhibiting some observed features which we were able to (iteratively) select while making these important refinements.

The gas dynamical and dynamo models described above together yield the gas density and the distribution of the large-scale magnetic field in the galaxy. The distribution of magnetic field in the galaxy plane resulting from Model 2 (introduced in Table 5.1), which we argue below to be our best model, is shown in Fig. 5.8. Given the number density of cosmic rays (n_{cr}) and thermal electrons (n_e) we can now construct synthetic radio observables using the procedure detailed in Sect. 4.4 in order to assess the quality of the model. We have computed synthetic radio polarization maps at wavelengths of 3.5 cm and 6.2 cm using the dynamo generated magnetic field and compared them with the observed radio maps. Since we do not model turbulent magnetic fields, we are unable to calculate the total radio intensity and to estimate the degree of polarization from the model.

We considered the models from Sect. 4.3 for n_{cr} . For all but one of the dynamo models listed in Table 5.1 we find that the simplest possible choice, $n_{\text{cr}} = \text{const}$, provides the best fit to the observed data, regardless of the other quantities adopted. The larger

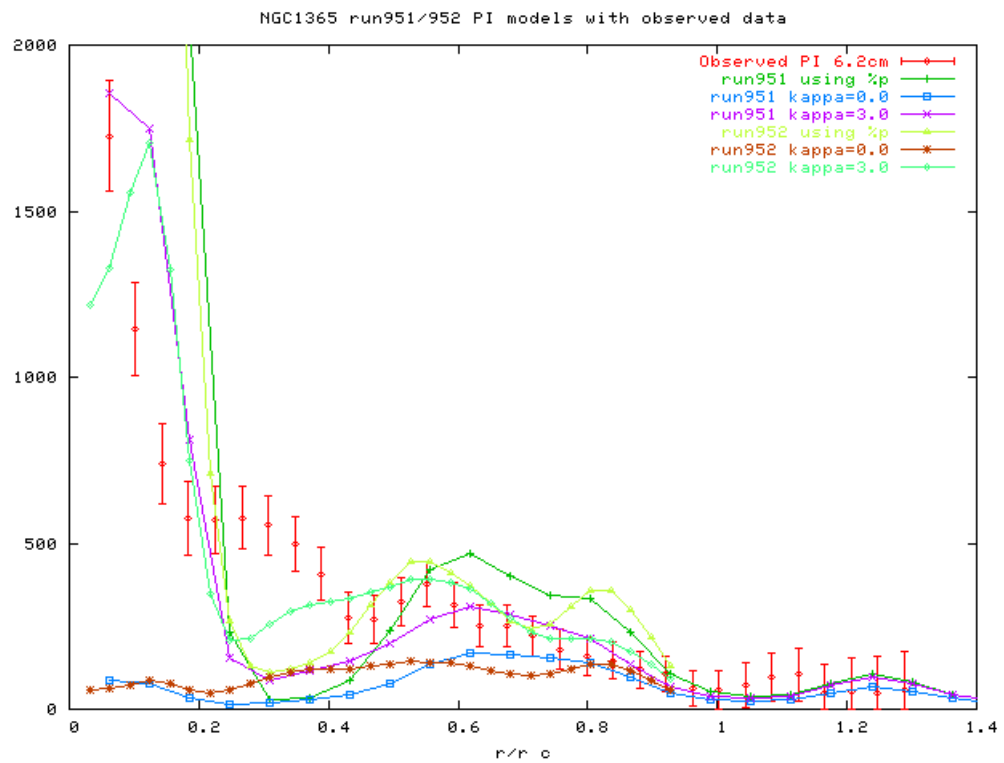


Figure 5.7: Azimuthally averaged radial profiles of polarized intensity for various models of NGC 1365 along with the observed values (as points with error bars). The parameter ‘kappa’ is the ‘ κ ’ defined in Eq. (4.5).

value of r_η in Model 1 produces a relatively weak magnetic field throughout a large central region compared with that at the ends of the bar. In order to fit the observed central peaks of polarized intensity, P , an implausibly non-uniform distribution of n_{cr} would be required in this model. Specifically, the cosmic ray distribution required to reconcile this model with observations would have a high peak within 3 kpc of the centre where magnetic field strength is minimum. For the other dynamo models, any plausible non-uniform distribution of n_{cr} produces too strong a central maximum of P relative to all other structures. In particular, the polarized intensity in the spiral arms is almost lost in models with non-uniform n_{cr} , being far weaker than that within 1–2 kpc of the centre. Since we have truncated the angular velocity at $r < 2.1$ kpc, the untruncated differential rotation would lead to an even stronger discrepancy.

Our synthetic maps, produced via the methods described in Sect. 4, do not include any depolarization effects due to random magnetic fields (see Burn 1966; Sokoloff et al. 1998), although they allow for depolarization by the regular magnetic fields (differential Faraday rotation and beam depolarization). In order to include Faraday depolarization effects due to the large-scale magnetic field, we assumed a nominal constant ionization fraction of $X = n_e/n = 0.1$, corresponding to a thermal electron density of 0.1 of the total gas density obtained from the gas dynamical simulations as described in Sect. 5.3.2. Guided by analogy with the Milky Way, where the average total gas density is 1 cm^{-3} whereas the thermal electron density is 0.03 cm^{-3} , a smaller value of X might be appropriate. We show results for X close to this value in Sect. 5.3.4. In Sect. 5.3.10, we discuss the effect of variations in X and argue that $0.01 \lesssim X \lesssim 0.2$.

We used two main techniques to compare the synthetic maps with observations and therefore to select the optimal magnetic field model. We chose to use the $\lambda 6.2$ cm map of polarized intensity in the analysis since it has the best signal-to-noise ratio. All model data, including synthetic radio maps, have been smoothed (in terms of the Stokes parameters Q and U) to match the resolution of the observations. In Sect. 5.3.5 we compare the distributions of polarized intensity on cuts along various paths in the plane of the sky. In Sect. 5.3.6 we analyse the difference between the computed and observed polarized intensities in two dimensions. In addition, we compare the orientations of the magnetic B -vectors obtained from the observed and synthetic Stokes parameters (Sect. 5.3.8).

To rotate the model galaxy to the position of NGC 1365 in the sky, we took the inclination angle $i = 46^\circ$ and the position angle of the galaxy's major axis (i.e the intersection of the sky plane and the galaxy plane) $\text{PA} = 222^\circ$, which are those assumed in obtaining the rotation curve for our (favoured) gas dynamical model. Results are

quite sensitive to these values, and it is possible that a reappraisal could result in noticeable changes.

5.3.4 Synthetic polarization maps

Overall, Model 2 (specified in Table 5.1) appears to provide the best fit to the observed polarization map; Model 4 is only slightly worse – see Sect. 5.3.5. Contours of B^2 shown in Fig. 5.8 indicate that the regular magnetic field is stronger in the bar region where gas density is large, and outside the regions of high density in the spiral arms. There are magnetic features apparently unrelated to the density distribution [e.g., those passing through the positions $(x, y) \approx (-5, 8), (5, -8)$]; they are presumably formed by a locally enhanced velocity shear. The magnetic field has a deep minimum within the bar, mainly produced by the density deficiency in that region. Other important features clearly visible in Fig. 5.8 are the magnetic field enhancements in the dust lane region, where magnetic field is amplified by both compression and shear, and the prominent central peak.

The synthetic polarization map for this model is shown in Fig. 5.9 and the equivalent map for model 4 is shown in Fig. 5.10. This can be compared directly with the observed map in the right-hand-panel of Fig. 5.1; the maps (and all other maps we show) are at a similar scale to facilitate the comparison; we make this comparison more quantitatively in Sect. 5.3.6. Our models have a high degree of symmetry, whereas the ‘real’ NGC 1365 is only approximately symmetric; since the observed map looks more regular on the eastern side, we shall mostly refer to that part of the galaxy unless stated otherwise. Despite the difference in symmetry, there is broad agreement between these two maps; for example, both have a deep minimum of P near the bar’s major axis where gas density is low, and both have the magnetic spiral arms displaced from the gaseous ones (although both magnetic arms are displaced to larger radii in the synthetic map, only one arm is so displaced in the observed map). The minimum of the synthetic P in the bar (corresponding also to a minimum of magnetic field within the bar, as seen in Fig. 5.8), is broader than of the observations (see Sect. 5.3.5). The reason for this is the very low gas density in this region, leading to weaker magnetic fields via Eq. (5.3). This feature is further discussed in Sect. 5.4 where we argue that the gas dynamical model underestimates significantly the amount of molecular gas in the bar region. Synthetic P is large both to the north and south of the bar major axis. In particular, the model reproduces a maximum of P upstream of the bar major axis, centred in the $\lambda 6.2$ cm map of Fig. 5.1 at (RA = 03h 33 min 40 sec, Dec = $-36^\circ 09'00''$). These maxima apparently arise from slightly enhanced velocity shear (that locally amplifies magnetic field) rather

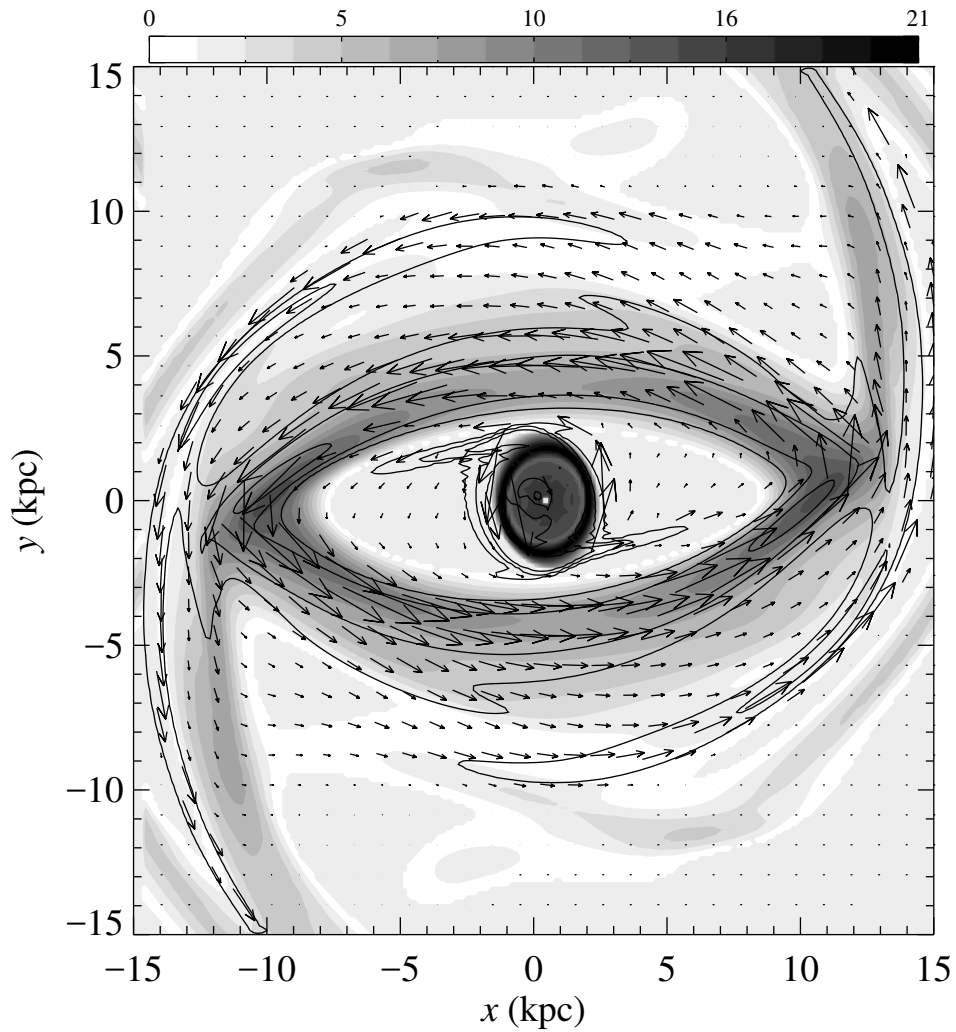


Figure 5.8: Energy density contours and vectors of the regular magnetic field \mathbf{B} from Model 2 (see Table 5.1), both at $z = 0$, are shown together with gas number density represented with shades of grey. The contours shown correspond to approximately 0.1, 0.6 and 3.0 times the r.m.s. value; the length of the vectors is proportional to B^2 . The scale bar at the top of the frame refers to the gas number density in the units of hydrogen atoms per cm^3 .

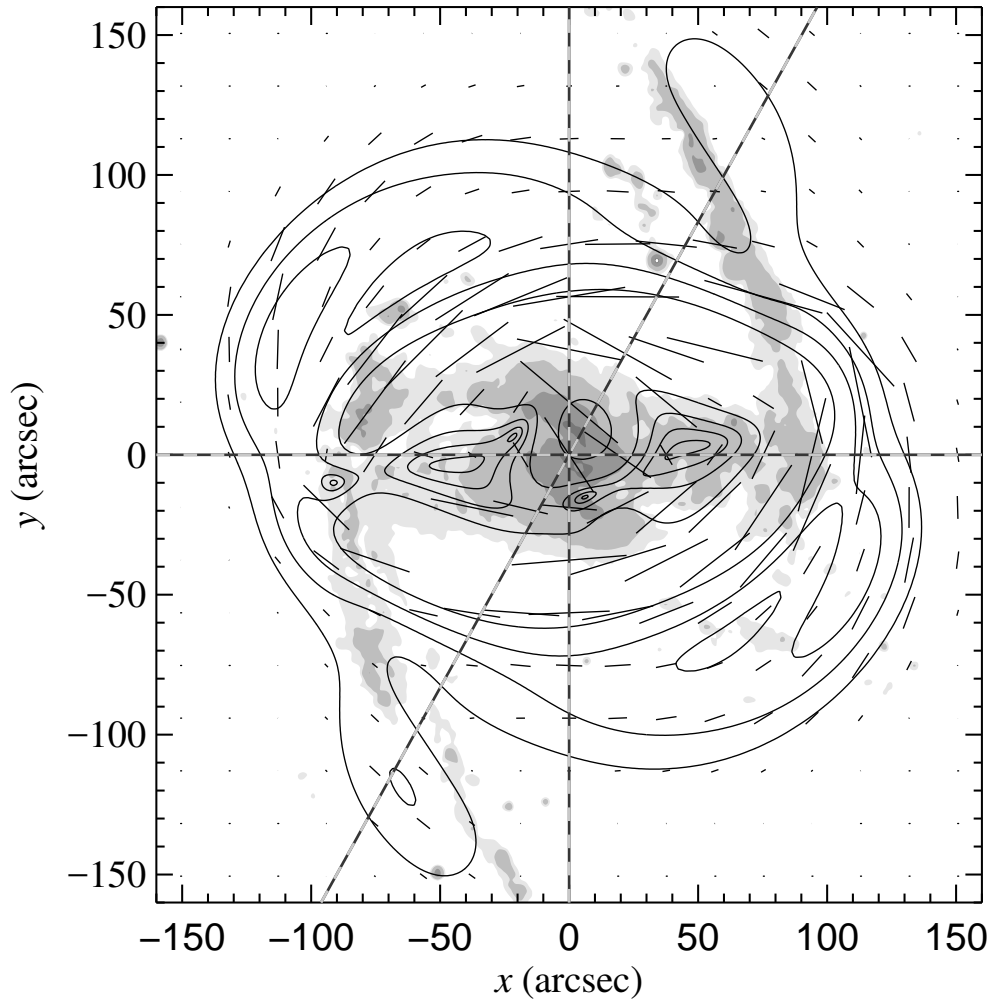


Figure 5.9: A synthetic map of polarized synchrotron intensity (contours) and polarization planes at $\lambda 6.2$ cm, resulting from Model 2 (see Table 5.1) assuming that $n_{\text{cr}} = \text{const}$, are shown superimposed on the optical image of the galaxy NGC 1365 (shown in only a few shades of grey for clarity). The synthetic map has been smoothed to the resolution of $25''$ to match that of the observed map shown in Fig. 5.1. The contour levels shown are approximately $(1, 3, 6, 12, 32) \times P_{\text{max}}/45$, where P_{max} is the maximum of P in the synthetic map. Dashed lines show the position of cuts discussed in Sect. 5.3.5.

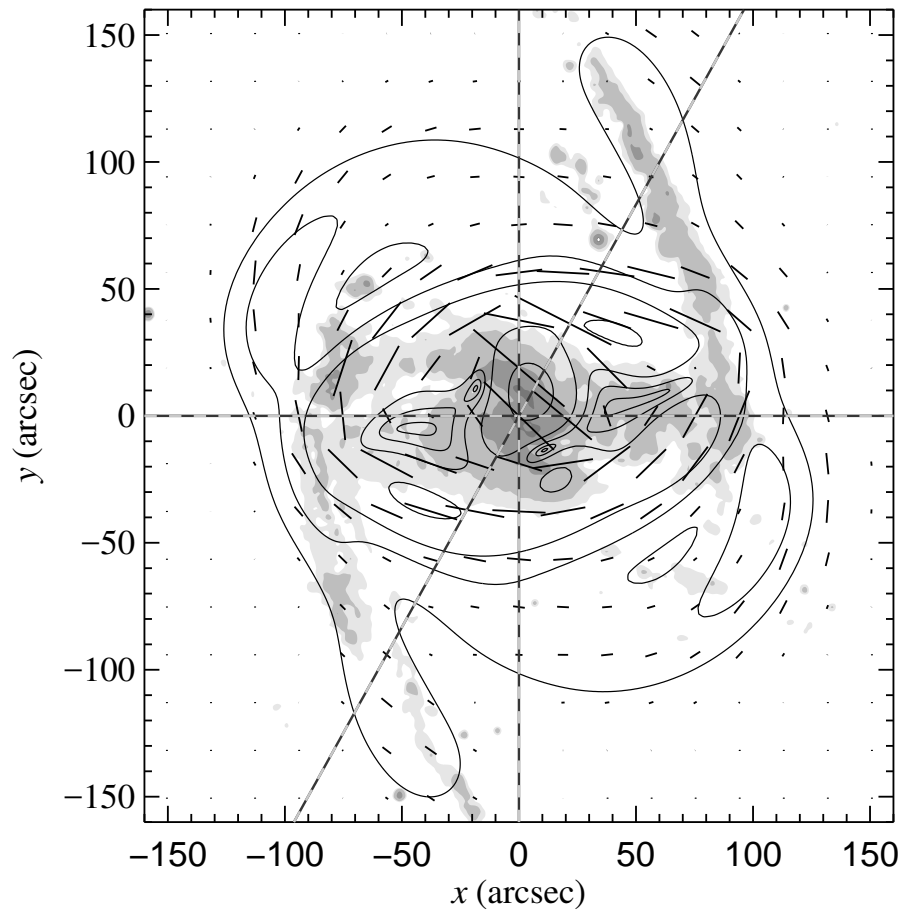


Figure 5.10: As Fig. 5.9, but for Model 4.

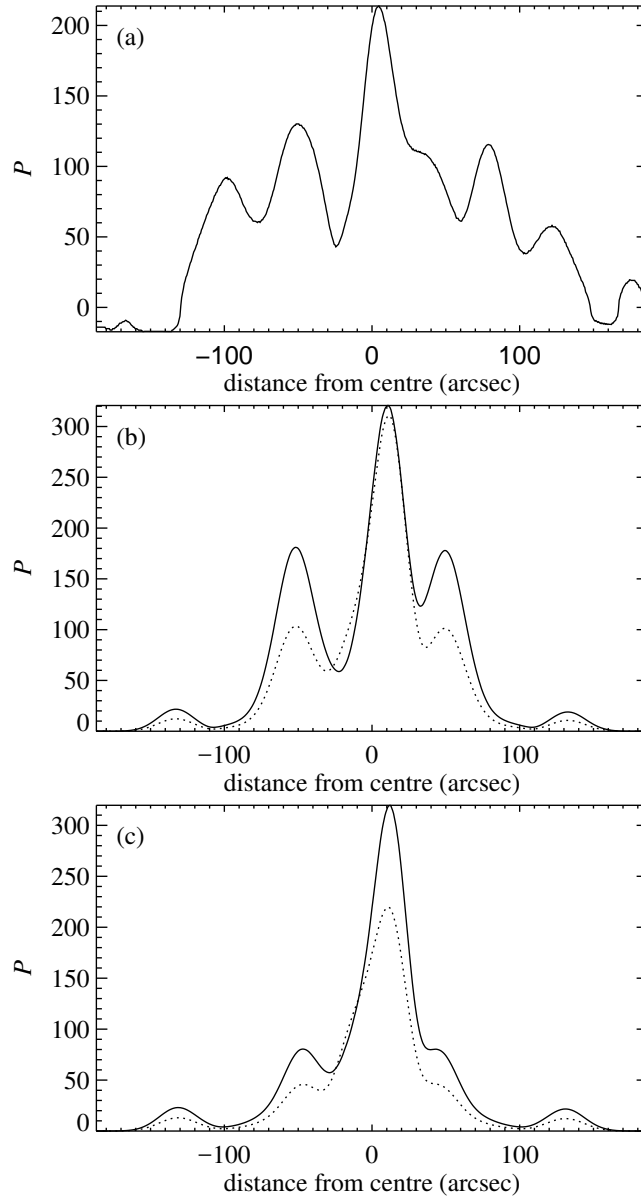


Figure 5.11: Cuts, at position angle -31° passing through the galactic centre (left to right in the plots corresponds moving from south-east to north-west in the sky), through polarized intensity maps at $\lambda 6.2$ cm smoothed to $\text{HPBW} = 25''$, for **(a)** the observed map, and synthetic maps from **(b)** Model 2 and **(c)** Model 4, both for $n_{\text{cr}} = \text{const}$. In panels (b) and (c), the synthetic profiles for $\lambda 6.2$ cm and $\lambda 3.5$ cm are shown solid and dotted, respectively; the difference is due to Faraday and beam depolarization for the assumed ionization degree $X = 0.1$. The units of P are as in Fig. 5.1 for (a) and arbitrary in (b) and (c), but adjusted to fit a similar range. The dotted profiles for $\lambda 3.5$ cm with $X = 0.1$ also correspond to P at $\lambda 6.2$ cm with $X = 0.032$.

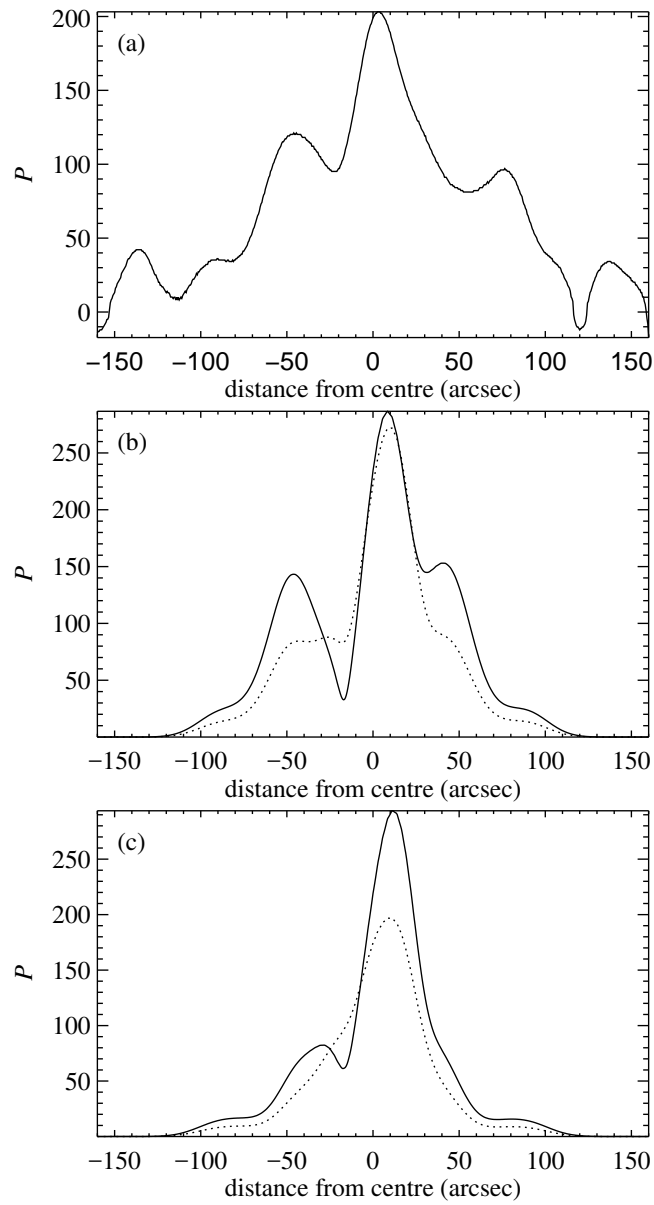


Figure 5.12: As in Fig. 5.11, but at position angle 0° (left to right is south to north in the sky).

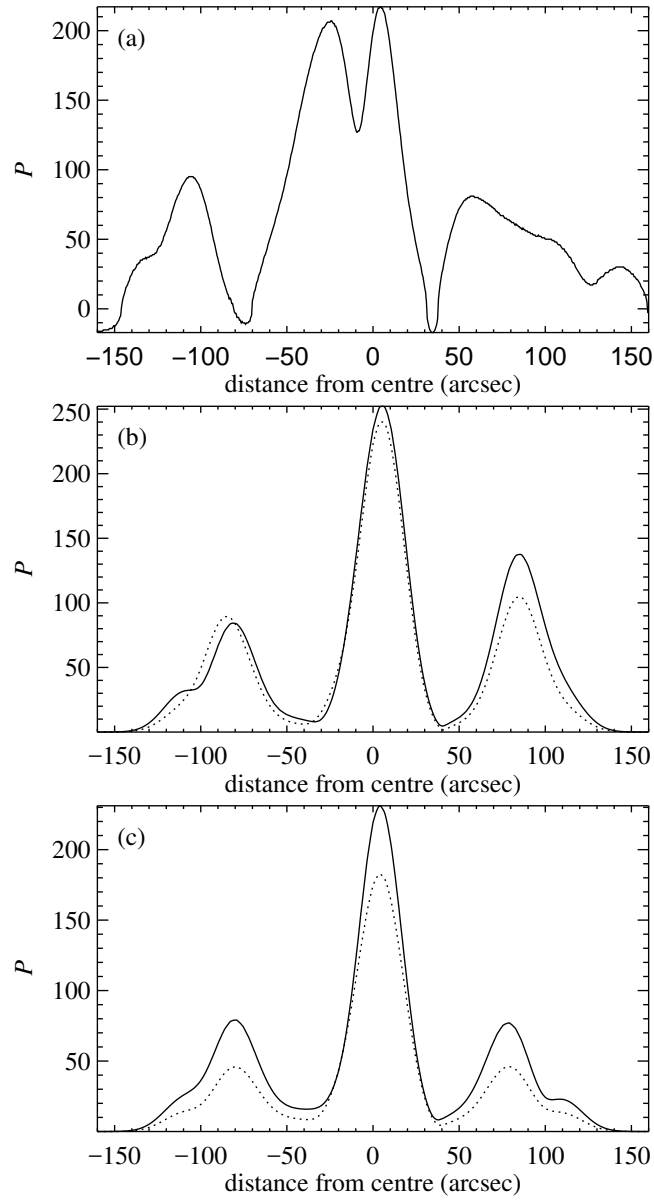


Figure 5.13: As in Fig. 5.11, but at position angle -90° (left to right is east to west in the sky).

than from local density maxima. We also note maxima of P near the ends of the bar and the beginning of the spiral arms, at (RA = 03h 33 min 45 sec, Dec = $-36^\circ 08'15''$) and (RA = 03h 33 min 28 sec, Dec = $-36^\circ 08'30''$). We note that the observed total emission (not shown here; see Beck et al. (2005)) is related to gas density in a rather straightforward manner being correlated with the gas density. The fact that this is not the case with the polarized intensity (as seen in both observed and synthetic maps) confirms that the observed regular magnetic field is not frozen into the gas, apparently being affected by the dynamo action.

5.3.5 Cuts through polarization maps

We found that comparisons can be usefully quantified and detailed using the cuts in the sky plane mentioned above. We show cuts only through the map at $\lambda 6.2$ cm because this map has higher signal-to-noise ratio and includes the large-scale emission fully. However, depolarization is significant at this wavelength (see Sect. 5.1) and has to be taken into account when comparing the model and observations. We use cuts through the centre of the galaxy at position angles PA = 0° , -90° and -31° , where PA is measured counterclockwise from the north as shown in Fig. 5.9. (The angle -31° is chosen so that the cut goes through the spiral arms; this corresponds roughly to a diagonal in the computational frame of Fig. 5.8.) The synthetic P has been normalized to make the mean difference between that and the observed P approximately zero. We have superimposed another profile from cuts through synthetic maps which represents both P at $\lambda 3.5$ cm with our favoured value of $X = 0.1$, and also at $\lambda 6.2$ cm with $X = 0.032$ (incidentally, this is close to the mean ionization degree of the warm diffuse gas in the Milky Way). The coincidence of these two cuts is due to equivalent Faraday depolarization, which depends directly on the quantity $\psi(z) \propto \lambda^2 X \int_z^\infty n B_{\parallel} dz$ (see Sect. 4). Here B_{\parallel} is the line of sight field component and $n_e = Xn$, therefore $\lambda^2 X = \text{const}$ identifies equivalence in depolarization. We see that this value is about the same in both cases (i.e. $6.2^2 \times 0.032 \approx 3.5^2 \times 0.1$). The difference between the polarization for these two possibilities is then just a λ -dependent scale factor.

The cuts are presented in Figs 5.11, 5.12 and 5.13 for the best-fit Model 2 and also for Model 4. The latter model has the background turbulent magnetic diffusivity η_0 enhanced by a factor of 2. This leads to a significantly smoother, less structured distribution of P . Thus, comparison of Models 2 and 4 allows us to suggest that the effective turbulent magnetic diffusivity in the interstellar gas of barred galaxies is, on average, close to $\eta_0 = 10^{26} \text{ cm}^2 \text{ s}^{-1}$. This value is typical of spiral galaxies in general and is that obtained if the turbulent speed v_t is close to 10 km s^{-1} and the turbulent

scale is about $l = 0.1$ kpc; $\eta_0 \simeq \frac{1}{3}lv_t$.

Our model neglects depolarization due to random magnetic fields which can reduce the value of P in the central parts more strongly than in the outer galaxy and therefore affect the relative height of the central peaks in Figs 5.11–5.13. Depolarization due to internal Faraday dispersion reduces the degree of polarization to

$$p = p_0 \frac{1 - e^{-S}}{S}, \quad (5.9)$$

where $S = 2\sigma_{\text{RM}}^2\lambda^4$ with $\sigma_{\text{RM}}^2 = 2C_1^2\langle b^2\rangle\langle n_e^2\rangle dL$ the variance of the Faraday rotation measure. Here C_1 is the dimensional constant appearing in the definition of the Faraday rotation measure (see Sect. 4), b is the turbulent magnetic field, angular brackets denote averaging (the fluctuations in magnetic field and thermal electron density are assumed to be uncorrelated), d is the turbulent scale and L is the path length (Sokoloff et al. 1998). The best available estimate of the random magnetic field in the central region of NGC 1365, $b \simeq 40 \mu\text{G}$, follows from the total synchrotron intensity assuming equipartition between cosmic rays and magnetic fields (see however Sect. 5.3.9 for a discussion of the validity of this assumption). For $n_e = 0.03 \text{ cm}^{-3}$, $d = 0.1$ kpc, $L = 1$ kpc and $\lambda = 6.2$ cm, we then obtain $S \simeq 6$, implying that this mechanism can depolarize the central peak significantly, giving $p/p_0 \simeq 0.2$. Since the height of the secondary peak should also be affected by depolarization, albeit to a lesser extent, we expect that the ratio of the two peaks will be reduced by a factor smaller than five. We note, however, that this estimate is uncertain since the number density of thermal electrons, their filling factor, turbulent scale and other parameters are not known well enough. An alternative is to assess the importance of this depolarization effect by comparing polarized intensities at $\lambda 6.2$ cm and $\lambda 3.5$ cm. The ratio of the central peak to the secondary ones at $\lambda 3.5$ cm is about 6–8, as opposed to 2–3 at $\lambda 6.2$ cm. The difference can be attributed to Faraday depolarization (by both regular and random magnetic fields). Assuming that Faraday depolarization at $\lambda 3.5$ cm is negligible, we conclude that it can reduce the degree of polarization at $\lambda 6.2$ cm by a factor as large as 4, which is consistent with the analytical estimate. We conclude that the relative height of the central peak in the synthetic cuts of Figs 5.11–5.13 would be reduced by Faraday dispersion, therefore improving the agreement of our models with observations, although this is difficult to estimate accurately.

Given the above uncertainties in the amount of depolarization, all three cuts for Model 2 are similar to those observed. In particular, the relative heights of the peaks in P and, more importantly, the positions of both maxima and minima are remarkably

realistic. The characteristic feature of this model is that η is further enhanced by a factor of $q_\eta \simeq 3$ in the inner region of NGC 1365, $r \lesssim 3$ kpc. This enhancement can be due to a higher rate of star formation, and hence more hot gas, with a correspondingly higher speed of sound, which would allow the turbulent speed to be larger than elsewhere.

The Model 2 cut at PA = -31° (Fig. 5.11), which passes through the spiral arms, shows an encouraging agreement with observations. For example, B has a maximum slightly outside the northern arm in both this model and the real galaxy. However, the outermost maxima produced by the spiral arms are slightly too far away from the centre in the model. As illustrated in Fig. 5.11(b), the relative heights of the peaks at $\lambda 6.2$ cm are significantly affected by Faraday rotation even for $X = 0.1$, where they clearly differ by more than just a scale factor between $\lambda 6.2$ cm and $\lambda 3.5$ cm.

The cut at PA = 0 (Fig. 5.12) exhibits similar degree of agreement with the observations. The main deficiency of the model here is the too narrow distribution of P (the magnetic structure of the model is too poor outside the bar) and the minimum is too deep near the centre of the cut.

The cut at PA = -90° in the synthetic map, shown in Fig. 5.13, has a central maximum that is too narrow (or off-centre minima that are too broad). This difference results in the deep minima in the difference parameter δ discussed in Sect. 5.3.6. The sharp minimum in the observed cut near the centre is a result of beam depolarization; it occurs in the synthetic cuts as well, but is removed by smoothing.

Model 2 seems to be almost optimal. The model could be fine tuned by changing η_0 and r_η within the ranges $(1-2) \times 10^{26} \text{ cm}^2 \text{ s}^{-1}$ and 1.5-3, respectively. For example, the secondary peaks in the PA = 0 cut decrease in strength in Model 4. Further, increasing n_{cr} by a factor of 2 within the central 1.5 kpc would make the central peak higher. However, we have not made such *post hoc* adjustments.

5.3.6 The difference maps

To obtain a global comparison of the models and observations, we produced maps of the difference between the observed and synthetic polarization at $\lambda 6.2$ cm, with the synthetic polarization scaled to make the mean difference approximately zero; this measure was further normalized by dividing the difference by the appropriately normalized noise level of the observed map giving

$$\delta = \frac{(1.4P/P_{\text{max}})_{\text{model}} - (P/P_{\text{max}})_{\text{obs}}}{(\sigma_P/P_{\text{max}})_{\text{obs}}} . \quad (5.10)$$

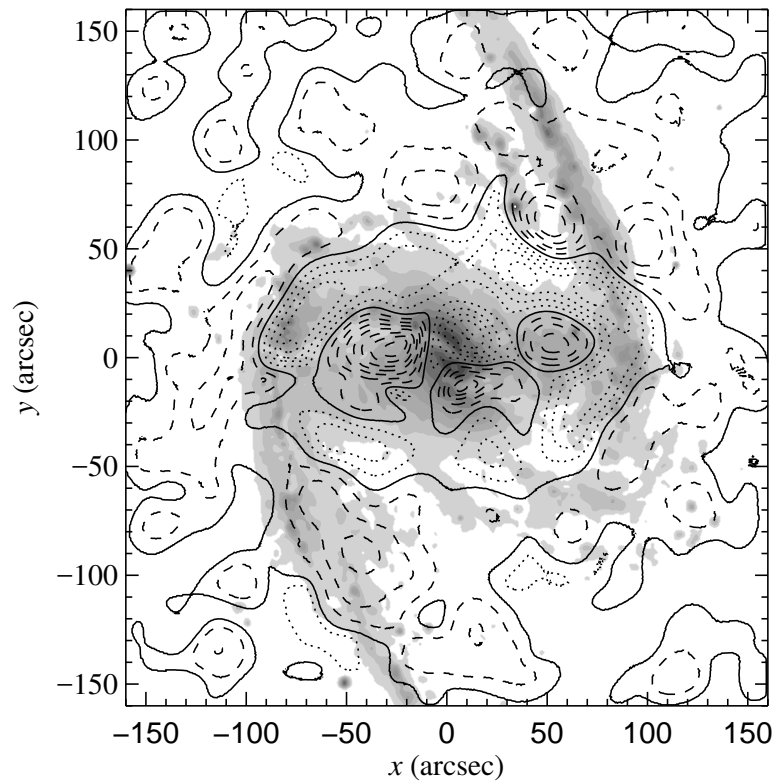


Figure 5.14: The relative difference δ between normalized synthetic and observed polarization maps at $\lambda 6.2$ cm, as defined in Eq. (5.10), superimposed on the optical image of NGC 1365. The contour spacing is 2, with the zero contour shown solid, negative values of δ dashed, and positive, dotted.

Thus, all comparisons were performed pointwise after their reduction to the common resolution $25''$ – this is quite a stringent test of the model. The result is shown in Fig. 5.14 for Model 2.

Since the models – unlike the real galaxy – possess perfect symmetry, the difference can hardly be uniformly small: a perfect fit in one half of the galaxy would produce significant systematic discrepancy in the other half. With this caveat, the difference map shows an acceptable global agreement of the model with observations, in that it does not show much of the basic morphological elements of the galaxy. The normalized relative difference is about 6–14 in four spots observed to the east, south and north-west of the galactic centre, indicating that synthetic polarized intensity is too small upstream of the dust lanes and at two positions at the inner edge of the western spiral arm. Otherwise, $|\delta| \lesssim 4$ across the whole field of view. Given the limited scope of our model (e.g., it does not include any turbulent magnetic fields which can produce polarized radio emission where they are anisotropic), we consider this degree of agreement to be acceptable. We discuss in Sect. 5.3.9 a cosmic ray distribution that would provide an almost perfect fit of Model 2 to observations.

5.3.7 Faraday rotation

We can use polarized intensity (as in the comparisons above) to probe the distribution of the large-scale magnetic field strength, and also to deduce the orientation of the magnetic field in the plane of the sky (via polarization vectors). However, knowledge of this quantity does not determine the field direction. The Faraday rotation measure RM is sensitive to the direction of the magnetic field, but the observed RM map is very patchy because of the lower signal-to-noise ratio at $\lambda 3.5$ cm. Therefore, we used RM data only to establish a minimum acceptable degree of gas ionization.

5.3.8 Magnetic field structure

An analysis of the observed global magnetic structure in NGC 1365 that is sensitive to the direction of magnetic field was performed by Beck et al. (2005) by fitting the polarization angles obtained from multi-frequency observations. This analysis provides the large-scale magnetic field expanded into Fourier series in the azimuthal angle. Results there indicate the presence of a significant component with the azimuthal wave number $m = 1$ at almost all distances from the galactic centre. However, our underlying gas dynamical model has even symmetry in azimuth, so that modes with odd values of m do not occur in the modelled magnetic field. The contribution of the $m = 1$ mode to

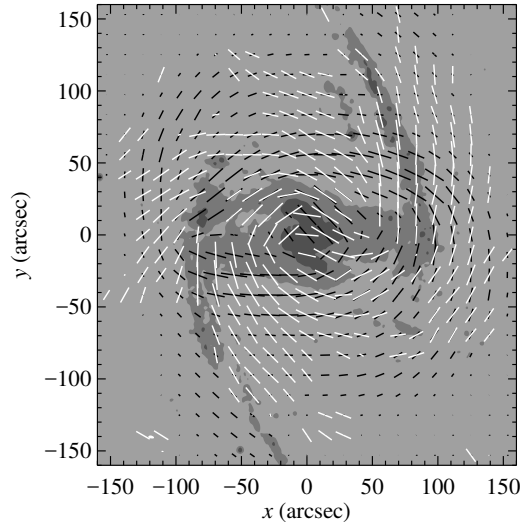


Figure 5.15: Orientations of the B -vectors of polarized emission obtained from the observed (white) and synthetic (black, Model 2) Stokes parameters at $\lambda 6.2$ cm. The vector lengths are proportional to \sqrt{P} . For the observed B -vectors, positions where polarized intensity is weaker than three times the noise level, $P < 3\sigma_P$, are neglected.

those Fourier expansions is more important than just producing the overall asymmetry. In particular, superposition of various azimuthal modes produces local magnetic features at kiloparsec scale which are lost if only even modes are retained in the observed structure to facilitate comparison with the model. Therefore, we did not find it useful to compare the modelled and observed magnetic structures in this manner. (The presence of unmodelled odd- m structure was also a feature of our study of NGC 1097 in Moss et al. 2001)

We instead compare directly the orientation of the magnetic field vectors in the observed and synthetic polarization maps. Comparison of two-dimensional vector fields is difficult. We could approach this by taking cuts through maps of the magnetic field orientation angles, as was done with the polarized intensity. However, a small shift in a feature such as a shock front can result in drastic differences between any such cuts made parallel to the front.

In Fig. 5.15 we show the orientation of both the synthetic and observed magnetic field vectors obtained directly from the corresponding Stokes parameters; points below 3 times the r.m.s. noise level are neglected in the observed maps. Agreement between model and observations is reasonable in the top left and bottom right quadrants near the bar (and partly further out), whereas the differences are quite large in the other regions. The difference is especially large near the beginning of the spiral arms. The

mean value of the difference between the observed and modelled polarization angles is 33° , and its standard deviation is 25° . For comparison, the errors in the observed polarization angle range from 2 to 10 degrees.

The overall difference is that the model polarization vectors are arranged into a more elliptical pattern around the bar than the observed ones, which exhibit a more circular configuration (and have almost constant pitch angles). It seems that the non-axisymmetric distortion due to the bar is weaker in the observed magnetic field than in the model. This could be because the magnetic field is coupled to a warm gas component which has less response to the bar's potential than cold gas and stars (Beck et al. 2005). We made a comparison similar to that in Fig. 5.15 but for Model 6, where the speed of sound is 30 km s^{-1} (see Table 5.1). The resulting gas dynamical model illustrated in Fig. 5.5 (right hand panel) has a more uniform density distribution and weaker deviations from axial symmetry. The improvement in the magnetic pattern was only marginal, and so the reason for this discrepancy remains unclear.

5.3.9 Sensitivity to parameters, and implications of the dynamo models

In this section, we discuss how synthetic radio maps are affected by various changes in our model. This allows us to infer useful information about the interstellar medium in the galaxy.

Distribution of cosmic rays

In order to calculate the synchrotron intensity, we need to specify the number density of cosmic ray electrons. In Sect. 4 we list models for this quantity for which we now discuss the consequences in our current galaxy model. As illustrated in Fig. 5.16, the major and universal effect of any plausible non-uniform distribution of n_{cr} is to enhance the central maximum in P , so that the peaks in the outer parts become relatively insignificant. Most importantly, any signature of the spiral arms almost disappears. If the synthetic polarized intensity is rescaled to fit that observed in the spiral arms, the central peak becomes unacceptably broad and high. Using $n_{\text{cr}} \propto B^2/p$ instead of p^{-1} as in model (iii) does not improve the situation. Similarly, it does not help if we use $n_{\text{cr}} \propto B_{\text{tot}}^2 = B^2 + 4\pi\rho v_t^2$, assuming that the random magnetic field is in equipartition with turbulent energy. Since models (ii) and (iii) involve the assumption of energy equipartition (or pressure balance) between cosmic rays and magnetic fields, we conclude that our results do not suggest this type of relation between cosmic rays

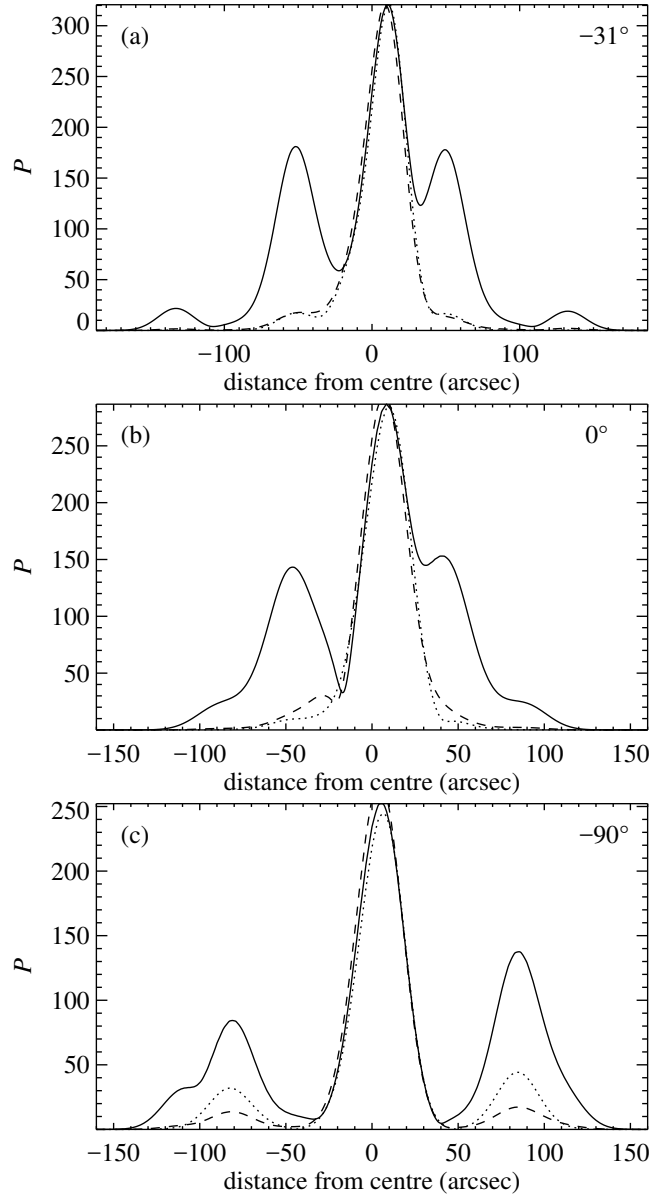


Figure 5.16: Cuts through radio maps for various models of cosmic ray distribution as defined in Eq. (4.5); the position angle of the cut is indicated in the upper right corner of each panel: **(a)** -31° , **(b)** 0° , and **(c)** -90° . The solid lines are for Model 2, i.e., with $n_{\text{cr}} = \text{const}$, and are identical to those in Figs. 5.11(b)–5.13(b); the other two cuts in each panel are for model (ii) $n_{\text{cr}} \propto \sqrt{I}$, dashed; and model (iii) $n_{\text{cr}} = p^{-1}$, dotted.

and magnetic fields at large scales.

We can think of several plausible explanations for this perhaps surprising result. It may be that some fraction of the polarized emission in the outer galaxy is produced by anisotropic magnetic fields which are not modelled. We do not consider this to be a very plausible option as this would require that the anisotropy is larger in the outer galaxy and in the spiral arms, rather than in the region of the central peak. Meanwhile, velocity shear, which might produce the anisotropy, is stronger in the inner bar region. More plausibly, cosmic ray diffusion makes their distribution smoother than that of the magnetic field. With the cosmic ray diffusivity of $K \simeq 10^{29} \text{ cm}^2 \text{ s}^{-1}$ and the confinement time $\tau \simeq 10^6 \text{ yr}$, their distribution would be rather homogeneous at scales $(K\tau)^{1/2} \simeq 1 \text{ kpc}$. We note, however, that our model suggests that cosmic ray distribution is almost uniform at scales of order 10 kpc.

It cannot be excluded that the synthetic polarization maps exaggerate the relative height of the central peak because they neglect Faraday depolarization due to random magnetic fields, namely the internal Faraday dispersion discussed in Sect. 5.3.5. As follows from Eq. (5.9), and discussion following it, it is not implausible that this effect can reduce the relative height of the central peak by a factor of five or somewhat less. As can be seen from Fig. 5.16, the ratio of the central to the secondary peaks at a distance of about $50''$ from the centre is about 20 or more for the non-uniform distributions of cosmic rays, whereas the observed ratio is about 2–3. Given the uncertainty of any estimates of the amount of depolarization, we cannot exclude that models with a non-uniform distribution of cosmic rays could be reconciled with observations.

We show in Fig. 5.17 the ratio of polarized intensity observed at $\lambda 6.2 \text{ cm}$ to the integral along the line of sight $\int B_{\perp}^2 ds$, with B_{\perp} the component of the modelled magnetic field in the sky plane. The latter is (roughly) proportional to the synthetic polarized intensity obtained for a uniform cosmic ray distribution. If our magnetic field model were perfect, the above ratio would show the variation of cosmic rays across the galactic image. We note that the value of the ratio varies remarkably little in the bar region; the most prominent variations arise from the local peaks of the observed polarized intensity that are also prominent in Fig. 5.14. Figure 5.17 confirms that the variation of cosmic ray energy density within the galaxy is rather weak and consists of a large-scale, smooth variation with contours of a shape similar to that of gas density and other tracers in the bar, and perhaps with a few local maxima.

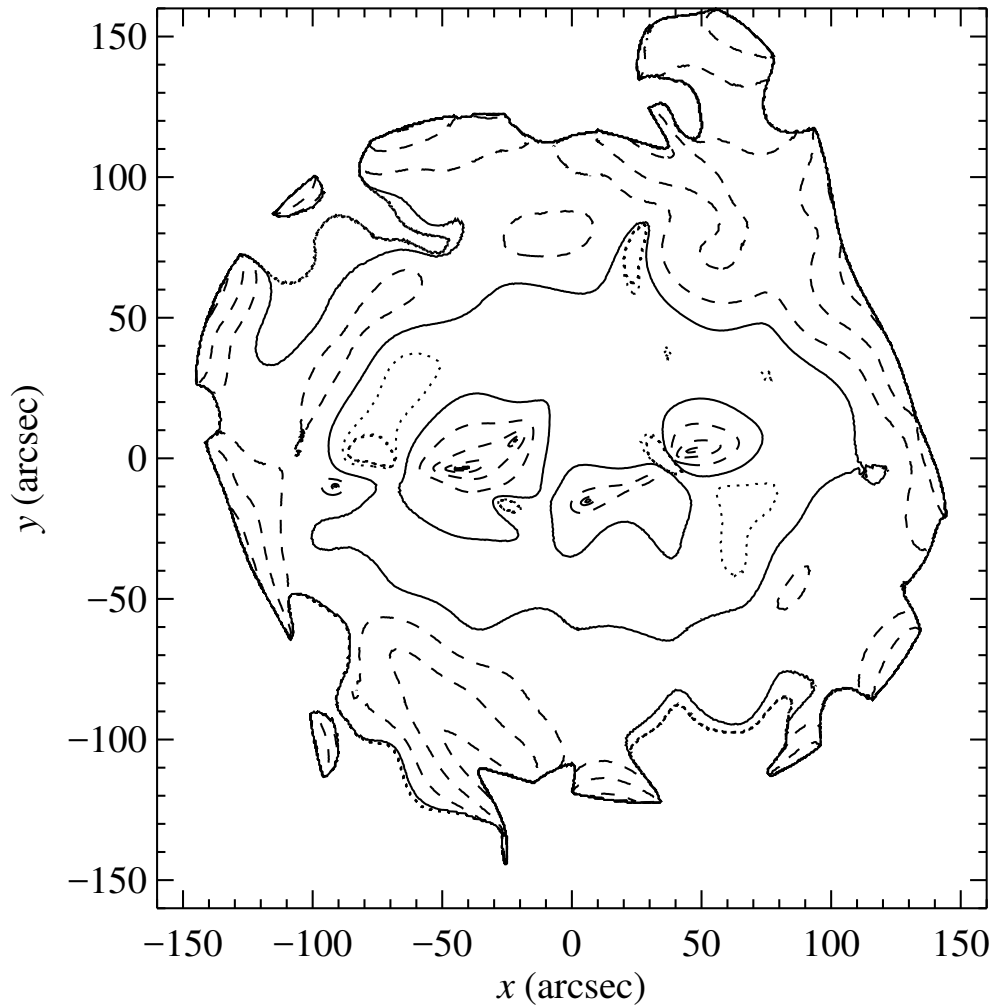


Figure 5.17: A map of the ratio of polarized intensity observed at $\lambda 6.2$ cm to the synthetic P obtained from Model 2 with $n_{\text{cr}} = \text{const}$. This ratio can be used to assess the variation of n_{cr} required to achieve a perfect fit to observations (neglecting any anisotropy of the turbulent magnetic fields and any contribution of a hypothetical galactic halo to the polarized emission). The contour at level unity is shown solid, the other contours are at levels 3^n , with negative and positive integer values of n ; contours above (below) unity are shown dashed (dotted).

The effects of the turbulent magnetic diffusivity

Models 2 and 4 yield very similar magnetic field distributions (see Fig. 5.11), even though the background turbulent magnetic diffusivity η_0 in Model 4 is more than twice as large as in Model 2 (see Table 5.1). The main effect of enhanced magnetic diffusivity is to make the secondary peaks of P in Model 4 less prominent, even with $n_{\text{cr}} = \text{const.}$ Model 4 could be reconciled with observations if n_{cr} were enhanced in the outer bar regions and in the spiral arms and/or reduced in the central part. Unless this is the case, and given that Model 2 agrees with observations better than Model 4, we conclude that our models support a value $\eta_0 \lesssim 10^{26} \text{ cm}^2 \text{ s}^{-1}$ in NGC 1365.

One of the effects of turbulent magnetic diffusion (and dynamo action) is to produce a misalignment between magnetic field and velocity in a shearing flow. Since the velocity shear is strong everywhere in the bar region and near the spiral arms, we expect that magnetic and velocity fields would be tightly aligned (in the corotating frame) if magnetic field were frozen into the flow (Moss et al. 2001).

The degree of alignment between the model magnetic and velocity fields in NGC 1365 is illustrated in Fig. 5.18, where we note that the angle between the two vectors exceeds 20° almost everywhere in the bar. The misalignment is also significant near the spiral arms.

The local enhancements of turbulent magnetic diffusivity, by a factor of 2–3, in the dust lanes and near the galactic centre introduced in Sect. 5.3.2 are important in our model as they allow us to avoid excessively large strength of the large-scale magnetic field produced by extreme velocity shear in those regions. As argued by Moss et al. (2001), such a local enhancement of interstellar turbulence may be associated with instabilities of the shear flow.

The rôle of dynamo action

Model 3 has the same parameters as Model 2, except that $R_\alpha = 0$. Thus, this model includes the same effects of rotation and velocity shear as Model 2, but without any dynamo action. In this model, the magnetic field decays on a timescale of about 0.6 Gyr, after an initial accelerated decay near the galactic centre. However, the magnetic structure in the outer parts of the galaxy is remarkably similar to that with $R_\alpha \neq 0$. We deduce that the magnetic structure we have obtained does not depend strongly on details of the poorly known α -effect, but rather is controlled by the large-scale velocity field, which is known much more reliably. The rôle of the α -effect is just to maintain the magnetic field against decay, which is enhanced by the strong shear typical of barred

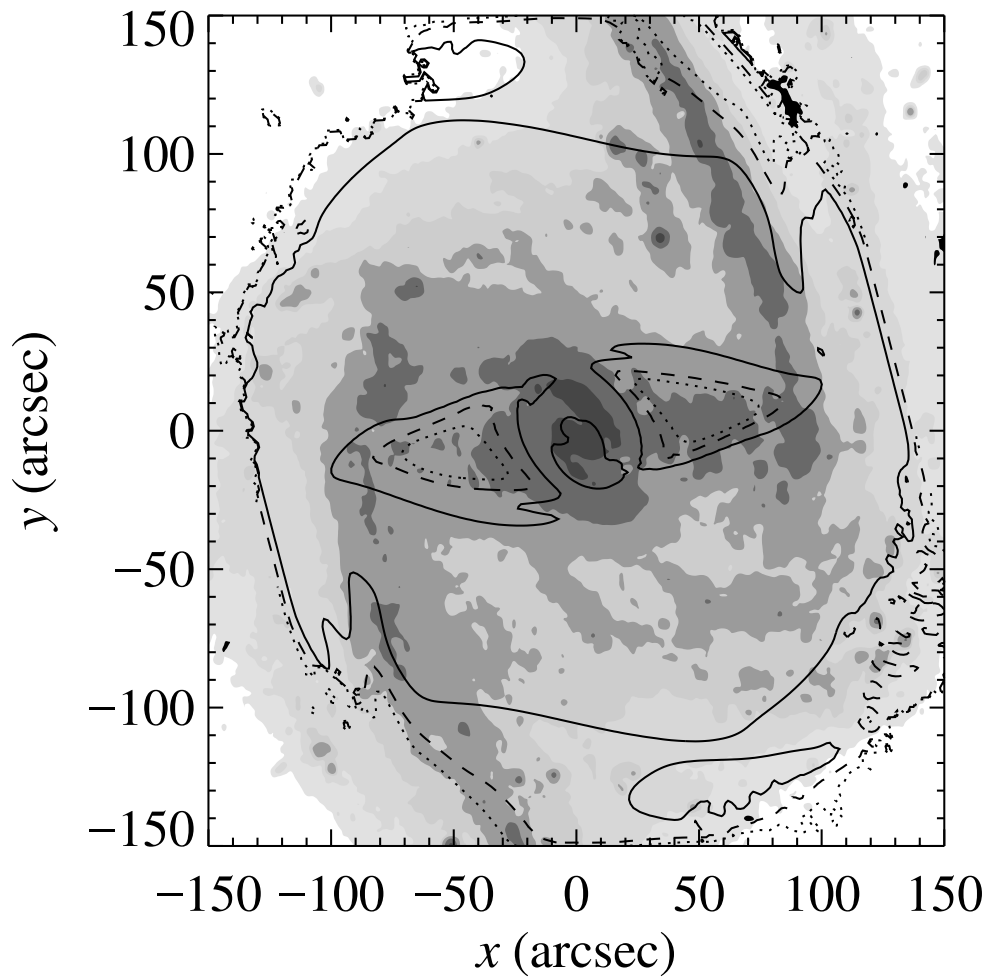


Figure 5.18: The alignment of the regular magnetic and velocity fields (in the co-rotating frame) illustrated with the contours of $\cos \chi = |\mathbf{u} \cdot \mathbf{B}|/uB$ at the midplane for Model 2, projected on to the optical image in the plane of the sky. The levels shown are 0.4 (dotted), 0.7 (dashed) and 0.95 (solid).

galaxies. This situation is similar to that found when modelling another barred galaxy, NGC 1097 (Moss et al. 2001).

The effect of the speed of sound

Models 2 and 6 have different values for the speed of sound (10 and 30 km s⁻¹, respectively). The higher speed of sound results in less structure in the velocity and density fields (even though we neglected to include an equivalent increase of the turbulent magnetic diffusivity by a factor of 3, which would be necessary for strict consistency). The cuts for Model 6 have relatively weaker features in the outer parts of the galaxy. This result appears less acceptable, and we deduce that 10 km s⁻¹ is a more favourable value for the speed of sound of the gas phase, to which the regular magnetic field is coupled.

5.3.10 Dependence on the gas ionization fraction

For $X \gtrsim 0.2$, the synthetic cuts of P show a much greater disagreement with the observed cuts than when $X = 0.1$. For example, for the cuts in Fig. 5.13, the effect of increasing X (and therefore increasing depolarization) is to broaden the minima in P at about $\pm 50''$, and increase the ratios of the central maximum to outer maxima (at about $\pm 100''$).

When we calculate synthetic RM for values of $X \lesssim 0.01$, the range of values obtained does not match the observed range $\pm 600 \text{ rad m}^{-2}$. For example, at $X = 0.01$, the maximum synthetic RM is about 350 rad m^{-2} .

Provided a constant ionization fraction is appropriate, our models suggest that $0.01 \lesssim X \lesssim 0.2$ to be a plausible range of values.

5.4 Discussion and conclusions

We have constructed a three dimensional dynamo model for NGC 1365, with the rotation curve, non-circular velocities and gas density taken from a dynamical model for this particular galaxy. Thus, although we have taken a similar approach as in earlier studies of other specific barred galaxies (IC 4214, Moss et al. 1999a; NGC 1097, Moss et al. 2001), for NGC 1097 we adopted a generic dynamical model as input, whereas here we have been able to use a bespoke model. We have tried to make a much more detailed comparison between observations and model predictions than previously

Of course, we have been restricted to using a mean field dynamo model – for this sort of study there is really no plausible alternative currently available. Our modelling (and

that of the earlier papers, cited above) has demonstrated that when modelling galaxies with strong non-circular velocities the rôle of the mean field α -coefficient is primarily to offset the inevitable diffusive decay of the field, and thus allow a steady state with fields of order equipartition strength to be maintained. The major determinant of the field structure is the non-circular velocity field (Sect. 5.3.9 and Moss et al. 1998a, 2001), and the main features can be expected to persist for plausible field maintenance mechanisms. We must further bear in mind the other limitations of the modelling, including the restriction to the inner part of the galaxy, $r \leq 15$ kpc, which means that boundary effects may influence results near this radius.

Our main conclusions are as follows. We see no evidence for the variation in n_{cr} as strong as in B^2 . This may imply that equipartition between cosmic rays and the regular magnetic field is *not* maintained even at global scales. The discrepancy between our crude models involving the equipartition assumption and observations could be reduced if Faraday depolarization due to turbulent magnetic fields was taken into account. We have discussed this result further in Sect. 5.3.9.

The strongest deviations of the synthetic polarized intensity from that observed occur in the bar region, just upstream of the dust lanes. The reason for the low synthetic polarized intensity is the small value of magnetic field strength there in the model. More precisely, the depth of the minima in synthetic and observed P are similar but they occur at somewhat different positions, and those in the synthetic map are broader (see Fig. 5.13). However, the relative heights of the maxima in P are reproduced quite successfully. In this sense, the agreement is better than might be inferred from Fig. 5.14. The reason for the difference is the deep and broad minimum in the gas density in those regions. We believe this to be a shortcoming of the gas dynamical model, which was fitted to incomplete CO data. In particular, CO observations of NGC 1097 (Crosthwaite 2001) do not show the minima of the density in the bar region to be as deep as in the model of NGC 1365 used here.

Our preferred model relies on the galactic rotation curve and gas density distribution different from those suggested by Lindblad et al. (1996); the rotation curve used is that resulting from CO observations (Sofue et al. 1999). Our results are compatible with the observed distributions of polarized synchrotron intensity and the magnitude of the Faraday rotation measure for the number densities of ionized diffuse gas of order 0.16 cm^{-3} at a distance of order 5 kpc from the centre along the bar's minor axis and 0.21 cm^{-3} in the spiral arms. With the gas dynamical model used here, this corresponds to the mean ionization fraction of 0.01–0.2.

Our models confirm that magnetic field strengths in the inner bar region can be

strong enough to drive mass inflow at a rate of several solar masses a year (see also Moss et al. 2000, 2001; Beck et al. 2005). Thus, in these strongly barred, strongly magnetic galaxies, it becomes necessary to include the dynamical effects of magnetic fields in order to reproduce all features of the gas flow. It follows that self-consistent magnetohydrodynamic modelling of barred galaxies is required.

Keeping in mind that our dynamical model is incomplete, at least in that azimuthal structure corresponding to odd modes is omitted, our general conclusion is that mean field dynamo models are reasonably successful in modelling magnetic fields in this barred galaxy. Moreover, such models can also provide information about both the gas dynamical modelling process and conditions in the interstellar medium (see also the models for the ‘normal’ spiral galaxy M31 in Moss et al. 1998b). A robust conclusion is that, contrary to widely held opinions, dynamical effects of magnetic fields cannot be everywhere ignored in galaxy modelling.

Chapter 6

Basic conclusions

In this section we briefly state the main results of this work. The following is based on a range of arguments and results discussed in detail elsewhere in the text where indicated.

- The model of cosmic ray evolution in a random magnetic field produced by the fluctuation dynamo has been developed. We have found both strongly positive and negative correlations between the energy density of cosmic rays and gas density, which appears to be mainly determined by the ratio of energy densities in the statistically steady state. However, no similar correlation between the cosmic ray and magnetic energy densities (consistent with local equipartition) was found in the models considered. We have found that the distribution of cosmic ray energy can be much more uniform than the energy in magnetic fields and gas, due to the relatively large cosmic ray diffusivity. Consequently, we argue that equipartition between cosmic rays and other constituents of the ISM does not necessarily imply that cosmic rays play a significant rôle in the dynamics of the ISM.
- We suggest that deviations from the standard (Fickian) diffusion of cosmic rays can be significant due to their large diffusivity in the turbulent interstellar magnetic field. Non-Fickian terms render wave-like features to the cosmic ray propagation; these can significantly affect the cosmic ray dynamics under certain circumstances as discussed in Sect. 3. The non-Fickian diffusion formulation removes a numerical problem with the implementation of field-aligned diffusion and allows realistic (large) values of cosmic ray diffusivity to be employed in modelling.
- We have presented a more detailed comparison of galactic dynamo models with radio polarization maps than ever before by comparing directly synthetic maps for the models with real observations. We have demonstrated that simple quasi-kinematic models (with algebraic α -quenching) provide satisfactory general agreement with observations. We have identified the need to include the spatial variation of the turbulent magnetic diffusivity in order to reproduce the effects of large-scale shocks on magnetic fields. Our results suggest that the dynamical effects of magnetic fields can not be completely ignored in galaxy modelling, particularly for the strongly-barred galaxies we have considered here.
- The distribution of polarized synchrotron emission across the barred galaxy NGC 1365 can be best reproduced if the cosmic ray energy density does not vary much within

about 10 kpc of its centre. As with the model for cosmic ray evolution in a random magnetic field of Sect. 3, our modelling of NGC 1365 seems to rule out a cosmic ray distribution consistent with the local equipartition with magnetic fields, which would vary strongly across the galaxy (of course, localized variations, e.g. in the nuclear region, remain possible or even necessary).

Appendix A

Boundedness of cosmic ray energy density

Here we show that, in a closed or periodic domain, $\max(e_c)$ can only decrease as a result of (tensorial) diffusion. This is useful for showing that the diverging behaviour of U_c does not produce a singularity in e_c ; cf. Sect. 3.2.2. In order to avoid interference from other effects, we assume that the evolution of e_c is only governed by diffusion, i.e.

$$\frac{\partial e_c}{\partial t} = \nabla_i (K_{ij} \nabla_j e_c).$$

Note also that $\max(e_c) = \langle e_c^n \rangle^{1/n}$ for $n \rightarrow \infty$. Here, angular brackets denote volume averages. Thus, using integration by parts, we have

$$\begin{aligned} \frac{d}{dt} \langle e_c^n \rangle &= n \left\langle e_c^{n-1} \frac{\partial e_c}{\partial t} \right\rangle = n \langle e_c^{n-1} \nabla_i (K_{ij} \nabla_j e_c) \rangle \\ &= -n(n-1) \langle e_c^{n-2} K_{ij} (\nabla_i e_c) (\nabla_j e_c) \rangle \\ &\leq 0 \quad (\text{for any value of } n > 1). \end{aligned}$$

The last inequality assumes that the diffusion tensor is positive definite, which is true in our case, because

$$K_{ij} (\nabla_i e_c) (\nabla_j e_c) = (K_{\parallel} - K_{\perp}) (\hat{\mathbf{B}} \cdot \nabla e_c)^2 + K_{\perp} (\nabla e_c)^2$$

is positive. Therefore, $\max(e_c)$ must decrease with time.

Appendix B

The forcing function

We specify here the forcing function used in Sect. 3¹. It is defined as

$$\mathbf{f}(\mathbf{x}, t) = \text{Re}\{N \mathbf{f}_{\mathbf{k}(t)} \exp[i\mathbf{k}(t) \cdot \mathbf{x} + i\phi(t)]\},$$

where \mathbf{x} is the position vector. The wavevector $\mathbf{k}(t)$ and the random phase $-\pi < \phi(t) \leq \pi$ change at every time step, so $\mathbf{f}(\mathbf{x}, t)$ is δ -correlated in time. For the time-integrated forcing function to be independent of the length of the time step δt , the normalization factor N has to be proportional to $\delta t^{-1/2}$. On dimensional grounds it is chosen to be $N = f_0 \rho_0 c_s (|\mathbf{k}| c_s / \delta t)^{1/2}$, where f_0 is a dimensionless forcing amplitude. At each time step we select randomly one of many possible wavevectors in a certain range around a given forcing wavenumber. The average wavenumber is referred to as k_f . In Sect. 3, two different wavenumber intervals are considered: 1–2 for $k_f = 1.5$ and 4.5–5.5 for $k_f = 5$. The system is forced with transverse helical waves,

$$\mathbf{f}_{\mathbf{k}} = \mathbf{R} \cdot \mathbf{f}_{\mathbf{k}}^{(\text{nohel})} \quad \text{with} \quad R_{ij} = \frac{\delta_{ij} - i\sigma \epsilon_{ijk} \hat{k}_k}{\sqrt{1 + \sigma^2}},$$

where $\sigma = 1$ for positive helicity of the forcing function,

$$\mathbf{f}_{\mathbf{k}}^{(\text{nohel})} = (\mathbf{k} \times \hat{\mathbf{e}}) / \sqrt{k^2 - (\mathbf{k} \cdot \hat{\mathbf{e}})^2}, \quad (\text{B.1})$$

is a non-helical forcing function, and $\hat{\mathbf{e}}$ is an arbitrary unit vector not aligned with \mathbf{k} ; note that $|\mathbf{f}_{\mathbf{k}}|^2 = 1$.

¹This forcing function was also used by Brandenburg (2001), but in his Eq. (5) the factor 2 in the denominator should have been replaced by $\sqrt{2}$ for a proper normalization.

Bibliography

- Achterberg, A. 1981, *A&A*, 98, 195
- Bakunin, O. G. 2003a, *Uspekhi Fizicheskikh Nauk*, 46, 733
- Bakunin, O. G. 2003b, *Uspekhi Fizicheskikh Nauk*, 46, 309
- Barge, P. & Sommeria, J. 1995, *A&A*, 295, L1
- Beck, R., Brandenburg, A., Moss, D., Shukurov, A., & Sokoloff, D. 1996, *ARA&A*, 34, 155
- Beck, R., Ehle, M., Shoutenkov, V., Shukurov, A., & Sokoloff, D. 1999, *Nature*, 397, 324
- Beck, R., Fletcher, A., Shukurov, A., et al. 2005, *A&A*, 444, 739
- Beck, R. & Krause, M. 2005, *Astronomische Nachrichten*, 326, 414
- Beck, R., Shoutenkov, V., Ehle, M., et al. 2002, *A&A*, 391, 83
- Benjamin, R. A., Churchwell, E., Babler, B. L., et al. 2005, *ApJ*, 630, L149
- Berezinskii, V. S., Bulanov, S. V., Dogiel, V. A., Ginzburg, V. L., & Ptuskin, V. S. 1990, *Astrophysics of cosmic rays* (North-Holland, Amsterdam)
- Blackman, E. G. & Field, G. B. 2000, *ApJ*, 534, 984
- Blackman, E. G. & Field, G. B. 2003, *Physics of Fluids*, 15, L73
- Brandenburg, A. 2001, *ApJ*, 550, 824
- Brandenburg, A. & Dobler, W. 2001, *A&A*, 369, 329
- Brandenburg, A., Käpylä, P. J., & Mohammed, A. 2004, *Physics of Fluids*, 16, 1020
- Brandenburg, A., Procaccia, I., & Segel, D. 1995, *Physics of Plasmas*, 2, 1148

- Brandenburg, A. & Subramanian, K. 2005, *Phys. Rep.*, 417, 1
- Braun, R. 1991, *ApJ*, 54
- Breitschwerdt, D., McKenzie, J. F., & Voelk, H. J. 1991, *A&A*, 245, 79
- Burn, B. J. 1966, *MNRAS*, 133, 67
- Casse, F., Lemoine, M., & Pelletier, G. 2002, *Phys. Rev. D*, 65, 023002
- Cesarsky, C. J. 1980, *ARA&A*, 18, 289
- Chuvilgin, L. G. & Ptuskin, V. S. 1993, *A&A*, 279, 278
- Crosthwaite, L. P. 2001, PhD thesis, University of California, Los Angeles
- Curran, S. J., Polatidis, A. G., Aalto, S., & Booth, R. S. 2001, *A&A*, 373, 459
- Davis, L. J. & Greenstein, J. L. 1951, *ApJ*, 114, 206
- Drury, L. O. & Völk, J. H. 1981, *ApJ*, 248, 344
- Elperin, T., Kleeorin, N., & Rogachevskii, I. 1996, *Physical Review Letters*, 77, 5373
- Elperin, T., Kleeorin, N., & Rogachevskii, I. 1997, *Phys. Rev. E*, 55, 2713
- Englmaier, P. & Gerhard, O. 1997, *MNRAS*, 287, 57
- Farmer, A. J. & Goldreich, P. 2004, *ApJ*, 604, 671
- Felice, G. M. & Kulsrud, R. M. 2001, *ApJ*, 553, 198
- Gerhard, O. 2002, in *Astronomical Society of the Pacific Conference Series*, Vol. 273, *The Dynamics, Structure & History of Galaxies: A Workshop in Honour of Professor Ken Freeman*, ed. G. S. Da Costa & H. Jerjen
- Giacalone, J. & Jokipii, J. R. 1999, *ApJ*, 520, 204
- Ginzburg, V. L. & Syrovatskii, S. I. 1964, *The Origin of Cosmic Rays (The Origin of Cosmic Rays, New York: Macmillan, 1964)*
- Ginzburg, V. L. & Syrovatskii, S. I. 1965, *ARA&A*, 3, 297
- Gombosi, T. I., Jokipii, J. R., Kota, J., Lorencz, K., & Williams, L. L. 1993, *ApJ*, 403, 377
- Hall, J. S. 1949, *Science*, 109, 166

- Hanasz, M., Kowal, G., Otmianowska-Mazur, K., & Lesch, H. 2004, *ApJ*, 605, L33
- Hanasz, M. & Lesch, H. 2003, *A&A*, 412, 331
- Haugen, N. E. L., Brandenburg, A., & Mee, A. J. 2004, *MNRAS*, 353, 947
- Hillas, A. M. 2005, *Journal of Physics G Nuclear Physics*, 31, 95
- Hiltner, W. A. 1949, *Science*, 109, 165
- Hodgson, L. S. & Brandenburg, A. 1998, *A&A*, 330, 1169
- Jackson, J. D. 1975, *Classical electrodynamics* (92/12/31, New York: Wiley, 1975, 2nd ed.)
- Johansen, A., Andersen, A. C., & Brandenburg, A. 2004, *A&A*, 417, 361
- Jones, T. W. 1993, *ApJ*, 413, 619
- Jun, B.-I., Clarke, D. A., & Norman, M. L. 1994, *ApJ*, 429, 748
- Jun, B.-I. & Jones, T. W. 1999, *ApJ*, 511, 774
- Kang, H. & Jones, T. W. 1990, *ApJ*, 353, 149
- Kleeorin, N., Moss, D., Rogachevskii, I., & Sokoloff, D. 2002, *A&A*, 387, 453
- Kleeorin, N., Moss, D., Rogachevskii, I., & Sokoloff, D. 2003, *A&A*, 400, 9
- Kóta, J. & Jokipii, J. R. 2000, *ApJ*, 531, 1067
- Krause, F. 1972, *Astronomische Nachrichten*, 294, 83
- Krause, F. & Rädler, K. H. 1980, *Mean-field magnetohydrodynamics and dynamo theory* (Pergamon Press, Oxford)
- Kulsrud, R. & Pearce, W. P. 1969, *ApJ*, 156, 445
- Kulsrud, R. M. & Anderson, S. W. 1992, *ApJ*, 396, 606
- Landau, L. D. & Lifshitz, E. M. 1987, *Fluid Mechanics*, 2nd edn. (Course of theoretical physics, Pergamon Press, Oxford)
- Lequeux, J. 2005, *The interstellar medium* (The interstellar medium, Translation from the French language edition of: *Le Milieu Interstellaire* by James Lequeux, EDP Sciences, 2003 Edited by J. Lequeux. Astronomy and astrophysics library, Berlin: Springer, 2005)

- Lindblad, P. A. B., Lindblad, P. O., & Athanassoula, E. 1996, *A&A*, 313, 65
- Lindblad, P. O. 1999, *A&A Rev.*, 9, 221
- Longair, M. S. 1994, *High energy astrophysics. Vol.2: Stars, the galaxy and the interstellar medium* (Cambridge: Cambridge University Press, —c1994, 2nd ed.)
- Mac Low, M.-M. & Klessen, R. S. 2004, *Reviews of Modern Physics*, 76, 125
- Madore, B. F., Freedman, W. L., Silbermann, N., et al. 1998, *Nature*, 395, 47
- Mathewson, D. S. & Ford, V. L. 1970, *MmRAS*, 74, 139
- Miller, K. A. & Stone, J. M. 2000, *ApJ*, 534, 398
- Moffatt, H. K. 1978, *Magnetic field generation in electrically conducting fluids* (Cambridge, England, Cambridge University Press, 1978. 353 p.)
- Moss, D. 1997, *MNRAS*, 289, 554
- Moss, D., Korpi, M., Rautiainen, P., & Salo, H. 1998a, *A&A*, 329, 895
- Moss, D., Rautiainen, P., & Salo, H. 1999a, *MNRAS*, 303, 125
- Moss, D., Shukurov, A., & Sokoloff, D. 1999b, *A&A*, 343, 120
- Moss, D., Shukurov, A., & Sokoloff, D. 2000, *A&A*, 358, 1142
- Moss, D., Shukurov, A., Sokoloff, D., Beck, R., & Fletcher, A. 2001, *A&A*, 380, 55
- Moss, D., Shukurov, A., Sokoloff, D. D., Berkhuijsen, E. M., & Beck, R. 1998b, *A&A*, 335, 500
- Niklas, S. 1995, PhD thesis, PhD Thesis, Univ. Bonn, (1995)
- Ondrechen, M. P. & van der Hulst, J. M. 1989, *ApJ*, 342, 29
- Otmianowska-Mazur, K., Chyży, K. T., Soida, M., & von Linden, S. 2000, *A&A*, 359, 29
- Otmianowska-Mazur, K., Elstner, D., Soida, M., & Urbanik, M. 2002, *A&A*, 384, 48
- Pacholczyk, A. G. 1970, *Radio astrophysics. Nonthermal processes in galactic and extragalactic sources* (Series of Books in Astronomy and Astrophysics, Freeman, San Francisco)

- Padoan, P. & Scalo, J. 2005, *ApJ*, 624, L97
- Pariev, V. I., Istomin, Y. N., & Beresnyak, A. R. 2003, *A&A*, 403, 805
- Parker, E. N. 1965, *Planet. Space Sci.*, 13, 9
- Parker, E. N. 1966, *ApJ*, 145, 811
- Parker, E. N. 1979, *Cosmical magnetic fields: Their origin and their activity* (Oxford, Clarendon Press; New York, Oxford University Press, 1979, 858 p.)
- Parker, E. N. 1992, *ApJ*, 401, 137
- Ptuskin, V. S. 1979, *Ap&SS*, 61, 259
- Roberts, P. H. & Soward, A. M. 1975, *Astronomische Nachrichten*, 296, 49
- Ruzmaikin, A. A., Sokolov, D. D., & Shukurov, A. M. 1988, *Magnetic fields of galaxies* (Kluwer, Dordrecht)
- Rybicki, G. B. & Lightman, A. P. 1979, *Radiative processes in astrophysics* (New York, Wiley-Interscience, 1979. 393 p.)
- Ryu, D., Kim, J., Hong, S. S., & Jones, T. W. 2003, *ApJ*, 589, 338
- Sandqvist, A., Joersaeter, S., & Lindblad, P. O. 1995, *A&A*, 295, 585
- Scarrott, S. M., Ward-Thompson, D., & Warren-Smith, R. F. 1987, *MNRAS*, 224, 299
- Shukurov, A., Sokoloff, D., Subramanian, K., & Brandenburg, A. 2006, *A&A*, 448, L33
- Simpson, J. A. 1983, *Annual Review of Nuclear and Particle Science*, 33, 323
- Skilling, J. 1971, *ApJ*, 170, 265
- Skilling, J. 1975a, *MNRAS*, 172, 557
- Skilling, J. 1975b, *MNRAS*, 173, 255
- Sofue, Y., Tutui, Y., Honma, M., et al. 1999, *ApJ*, 523, 136
- Soida, M., Otmianowska-Mazur, K., Chyży, K., & Vollmer, B. 2006, *A&A*, 458, 727
- Sokoloff, D. & Shukurov, A. 1990, *Nature*, 347, 51
- Sokoloff, D. D., Bykov, A. A., Shukurov, A., et al. 1998, *MNRAS*, 299, 189, erratum: Sokoloff et al. (1999).

-
- Sokoloff, D. D., Bykov, A. A., Shukurov, A., et al. 1999, *MNRAS*, 303, 207
- Stone, J. M. & Norman, M. L. 1992, *ApJS*, 80, 791
- Strong, A. W. & Moskalenko, I. V. 1998, *ApJ*, 509, 212
- Subramanian, K. 1999, *Physical Review Letters*, 83, 2957
- Subramanian, K. & Mestel, L. 1993, *MNRAS*, 265, 649
- Vainshtein, S. I. & Cattaneo, F. 1992, *ApJ*, 393, 165
- van der Kruit, P. C. & Allen, R. J. 1978, *ARA&A*, 16, 103
- Wentzel, D. G. 1974, *ARA&A*, 12, 71
- Widrow, L. M. 2002, *Reviews of Modern Physics*, 74, 775
- Zeldovich, Y. B., Ruzmaikin, A. A., & Sokoloff, D. D. 1990, *The almighty chance*
(World Scientific Lecture Notes in Physics, World Scientific Publication, Singapore)